ISSN 1810-648X
E-ISSN 2537-6365

GHITU INSTITUTE OF ELECTRONIC
ENGINEERING AND NANOTECHNOLOGIES

INSTITUTE OF APPLIED PHYSICS

STATE UNIVERSITY OF MOLDOVA

PHYSICAL SOCIETY OF MOLDOVA

Moldavian Journal of the Physical Sciences

Chisinau
2019

Volume 18
No. 1-4

Scientific journal **Moldavian Journal of the Physical Sciences** includes original scientific articles, communications and reviews concerning various problems of modern physics. The journal is published in English, its periodicity is 4 numbers a year, with circulation of 200 copies.

web: http://www.nano.asm.md

GUIDELINES FOR AUTHORS

The "Moldavian Journal of Physical Sciences" appears quarterly and publishes in English papers referring to original scientific research in physics and related fields, including applications in electronics and technology, material engineering and device physics. A review paper for every issue is planned and short communications with hot news are encouraged.

Papers must be prefaced by a brief abstract in English up to 100 words. Single space of the rows in the manuscript is required.

Authors are invited to send two printed copies of their papers, as well as an electronic record on a $3^{1/4}$ inches diskette, or by e-mail, in English. The articles will be edited by using WORD for Windows. Chapters must be numbered by using Arabic figures, as follows:

3. Experimental results.
3.1. Results analysis.
3.2. Methods of calculus.

Formulae must be written very clearly and easy-to-read. Do not use non-explained abbreviations. Illustrations and diagrams must be realized on computer drafts (on images). All graphic and text objects must be of very good quality and easy to read. Figures included in the text are preferable.

Reference citations will be presented as follows: author's forename initial and last name, journal name, volume, page number, year (in parentheses), for example: F.A. Moldovan, S.P. Russu, Phys. Rev. Let. 85, 357, (2000). Complete title, publisher, city and year will be written for book's author's name and forename initial, for example: M. Teodorescu, Cooperation in science and technology with Eastern and European countries, Editura Tehnica, Bucuresti, vol. 1, 1992. References into the text will be made within square brackets, for example [7]; reference citation numbers must be made successively, as they appear into the text.

Manuscripts of regular papers should be limited up to 10 pages and will be signed by authors; they also must be marked "Ready to print". Reviews are limited up to 20 pages. Maximum 4 pages are admitted for short communications. One full page of the journal (size A4) contains 54 rows with 95 characters/row; font size - 12. Page set up: top, left, right – 2,5; bottom – 3,5 cm. The very manuscript which is marked "Ready to print" will be published within 6 months from sending.

The submitted papers must be reviewed by two independent reviewers. The papers must contain original work and have not submitted for publication to any other journal. The papers which have been published previously, as well those accepted to be published in other reviews, will be not be admitted by Editorial Board; the authors have to mention this situation.

Proofs will be sent to authors for checking. Corrections must be restricted to errors since modifications to the text may be charged to the author. The publishers reserve the right to adapt the presentation of an article to conform to our style. After their publishing in our journal, the manuscripts and corresponding illustrations become the property of Editorial Board and will not be returned to the authors. The same for the papers, which have not been admitted for publication. The publishing in our journal is made free of charge.

The papers sent for publishing are considered not secret. The authors only are responsible for this in front of their own institutes or employers. Authors have to mention their complete address and telephone, fax number and e-mail.

Papers from around the world can be sent to be published to the following address:

Ghitu Institute of Electronic Engineering and Nanotechnologies, 3/3 Academy St., MD 2028 Chisinau, the Republic of Moldova, tel. (00 37322) 73-70-92; E-mail: vvursaki@gmail.com, E-mail of responsible secretary: sofiadonu@yahoo.com

TWO-DIMENSIONAL EXCITON SUPERPOSITION STATES WITH DIRAC CONE DISPERSION LAWS

S. A. Moskalenko, I. V. Podlesny, and I. A. Zubac

Institute of Applied Physics, Academiei str. 5, Chisinau, MD-2028, Republic of Moldova
E-mail: exciton@phys.asm.md

(Received July 17, 2019)

Abstract

Our review paper is dedicated to studies of two-dimensional (2D) Wannier–Mott excitons in transition metal dichalcogenides and 2D magnetoexcitons in GaAs-type quantum wells subjected to the action of a strong perpendicular magnetic field, which both revealed the Dirac cone dispersion laws. It is shown that necessary conditions for the implementation of this property to be carried out are the taking into account of the electron–hole (e–h) exchange Coulomb interaction and the interdependence between the center-of-mass and relative e–h motions in the frame of the excitons. A short review describing the effect of these two factors on the Dirac cone dispersion law formation is presented.

1. Introduction

To date, two types of the 2D excitons with Dirac cone dispersion laws have been elucidated. One of them concerns the Wannier–Mott excitons in transition metal dichalcogenides (TMDCs), such as molybdenum and wolfram monolayers MoX_2 and WX_2 with X=S, Se [1]. The other type of excitons can be formed in GaAs quantum wells (QWs) subjected to the action of a strong perpendicular magnetic field [2]. Below, a short review of these two variants is presented. In both cases, the arising of the Dirac cone dispersion laws takes place under the influence of the electron–hole (e–h) exchange Coulomb interaction under conditions, where the interdependence between the center-of-mass and the relative e–h motions does appear. The linear dispersion law of the 2D Bose gas is a rare case. It can change the thermodynamic properties of the system opening a possibility of achieving its Bose–Einstein condensation (BEC) at finite temperatures even at its infinite extent [3].

According to Hohenberg [4], in a homogeneous 2D Bose gas with parabolic dispersion laws, the quantum fluctuations arising on the surface with an infinite extent are able to destroy the establishing of the coherent macroscopic states. The BEC of 2D excitons at nonzero temperatures becomes impossible. To avoid this restriction, it was necessary to confine the surface of the gas. For example, in the case of 2D cavity exciton polaritons with parabolic dispersion law, their BEC at low yet finite temperatures was achieved via confining the excitons on the surface of the light spot created by a laser beam on the QW embedded into the microcavity [5, 6].

2. Band Structures of Two Exciton Systems

The band structure of dichalcogenide monolayers was described in [1]. This type of monolayers happens to be direct band gap semiconductors with minimal direct band gaps at the

corner points $\vec{K}$ and $-\vec{K}$ of the hexagonal Brillouin zone, as shown in Fig. 1. There are two valleys $\vec{K}$ and $-\vec{K}$, where the valence electrons effectuate direct optical quantum transitions in the conduction bands, while maintaining their spin projections. Due to the symmetry of the Hamiltonian as regards the time inversion in the structures without a center of inversion, the Kramers theorem establishes that the energy of electron with spin up in valley $\vec{K}$ equals to the energy of the electron with spin down in valley $-\vec{K}$. This property is shown in Fig. 1. Direct optical quantum transitions take place with the participation of photons with different circular polarizations. The bare Wannier–Mott excitons appearing in $\vec{K}$ and $-\vec{K}$ valleys due to the direct Coulomb e–h interactions have the same energies of their binding and creation. Two degenerate valley exciton states can be characterized by valley pseudospin projections.

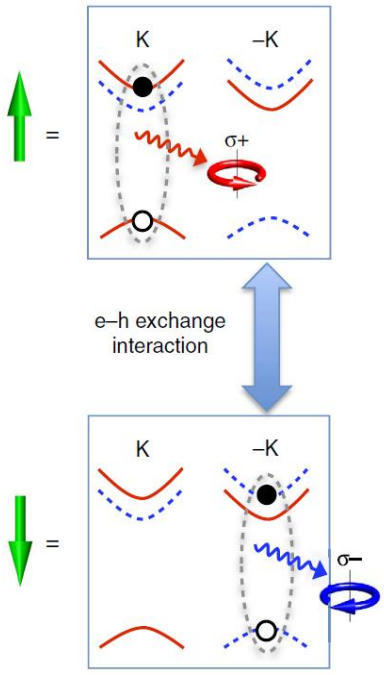

Fig. 1. Valley-orbit coupled exciton X_0. Valley pseudospin up and down configurations of X_0. The figure is reproduced from the paper of Yu. H. et al., Nat. Commun. 5, 3876 (2014).

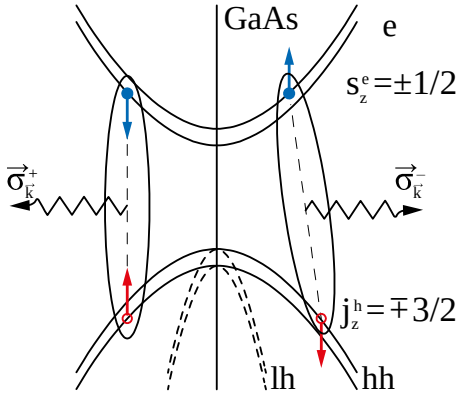

Fig. 2. Band structure of the GaAs crystal.

The band structure of GaAs QWs in the absence of an external perpendicular magnetic field is shown in Fig. 2. The conduction electrons have spin projections $s_z^e = \pm 1/2$, and the heavy holes have the full angular momentum projections $j_z^h = \pm 3/2$. Its origin is associated with the locking of the valence electron spin projection up (down) with the *p*-type orbit magnetic moment projection $M = 1(-1)$ giving rise to the resultant projections $3/2\,(-3/2)$, as shown in Fig. 3. The total angular momentum projection of the e–h pair $F = s_z^e + j_z^h$ is a quantum number characterizing the states of the e–h pairs and of the excitons. It has four possible values $F = \pm 1, \pm 2$. Two exciton states with $F = \pm 1$ are shown in Fig. 2. They can emit photons with different circular polarizations. As in the case of the TMDCs, in the case of GaAs QWs, there are two bare exciton degenerate states interacting with photons of different circular polarizations. A strong perpendicular magnetic field leads to the Landau quantization of the orbital motions and the formation of discrete energy levels of electrons and holes separately, as is shown in Fig. 4. Under the action of the Lorentz force, the magnetoexciton with in-plane wave vector $\mathbf{k}_{\|}$ looks as an electric dipole, as is shown in Fig. 5.

$$\psi_{c,s,\pm 1/2,\mathbf{q}} = \frac{e^{i\mathbf{q}\mathbf{r}}}{\sqrt{V}} U_{c,s,\mathbf{q}}(\mathbf{r}) \begin{vmatrix} \uparrow \\ \downarrow \end{vmatrix}; \qquad \varphi_{n,p}(x,y) = \frac{e^{ipx}}{\sqrt{L_x}} \varphi_n\left(y - pl_0^2\right); \quad l_0^2 = \frac{\mathrm{hc}}{eB}$$

$$\psi_{v,p,3/2,3/2,\mathbf{q}} = \frac{e^{i\mathbf{q}\mathbf{r}}}{\sqrt{2V}} [U_{v,p,x,\mathbf{q}}(\mathbf{r}) + iU_{v,p,y,\mathbf{q}}(\mathbf{r})] \left|\uparrow\right\rangle;$$

$$\psi_{v,p,3/2,-3/2,\mathbf{q}} = \frac{e^{i\mathbf{q}\mathbf{r}}}{\sqrt{2V}} [U_{v,p,x,\mathbf{q}}(\mathbf{r}) - iU_{v,p,y,\mathbf{q}}(\mathbf{r})] \left|\downarrow\right\rangle;$$

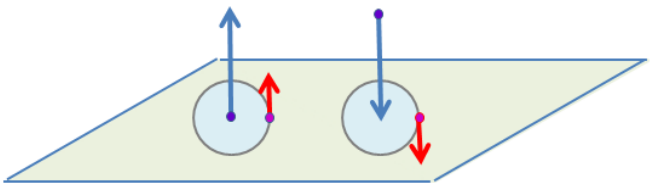

$$\boldsymbol{\sigma}_M = \frac{1}{\sqrt{2}}\left(\mathbf{a}_1 \pm i\mathbf{a}_2\right).$$

$$M = \pm 1$$

Fig. 3. Conduction and valence electron wave functions.

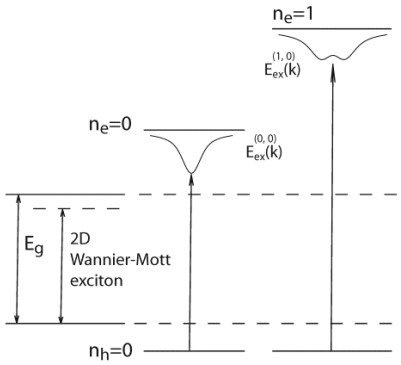

Fig. 4. Scheme of two magnetoexciton energy bands (reproduced from [7]).

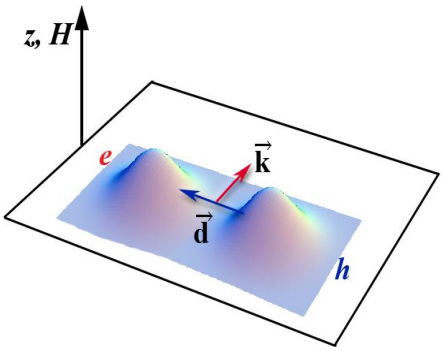

Fig. 5. Electric-dipole model of a 2D magnetoexciton with wave vector $\vec{k}$ and with the arm of the electric dipole moment $\vec{d}$ [8].

The binding energy and the ionization potential are determined by the direct Coulomb e–h interaction. The arm of the dipole is proportional to the center-of-mass wave vector yet perpendicular to it. Despite the change of the orbital structure of the magnetoexciton compared with the Wannier–Mott exciton with hydrogen atom-type structure, the spin structure of the magnetoexciton remains the same as in the absence of a magnetic field until the Rashba spin–orbit coupling (RSOC) is not taken into account. A new property of the 2D magnetoexciton is the interdependence between the center-of-mass and the relative e–h motions induced by the action of the Lorentz force. This interdependence happens to play an important role promoting to the formation of the Dirac cone dispersion law under the influence of the exchange e–h Coulomb interaction.

3. Electron–Hole Exchange Coulomb Interaction

The diagrams representing the direct, exchange, and mixed e–h Coulomb interactions are shown in Fig. 6. During the direct Coulomb scattering, the particles are moving separately without changing their origins. In the exchange scattering process, the e–h pairs are created and annihilated. In the case of the valley excitons in the TMDCs, these processes can take place with the electron from one valley and with the hole from another valley, which can lead to the interdependence between the center-of-mass and the relative e–h motions even in the absence of an external perpendicular magnetic field. In both cases, the exchange e–h Coulomb interaction removes the degeneracy of the bare exciton states and leads to the formation of their coherent superposition states with well-defined coefficients of linear combinations. These superposition states in the case of two valley exciton states were shown in [1]. One of them has a Dirac cone dispersion law, whereas the other state has a Kirgiz hat-type dispersion law with minimum energy on the circle formed by the in-plane wave vectors, as shown in Fig. 7.

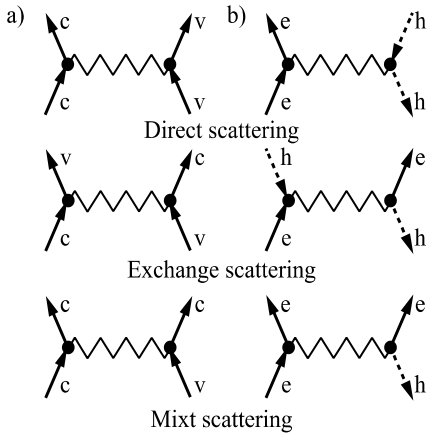

Fig. 6. Electron–hole Coulomb scattering processes: (a) in two-band representation and (b) in electron-hole description.

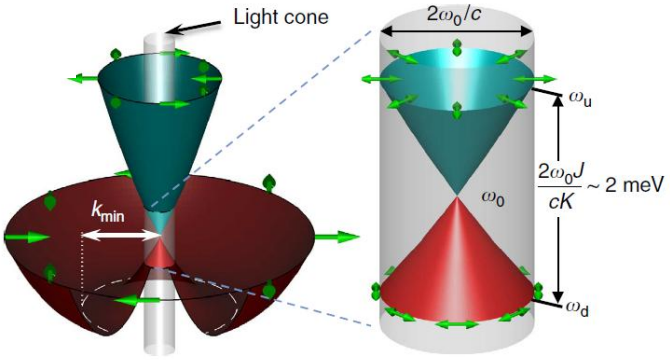

Fig. 7. Dispersion of valley-orbit coupled X_0, which in the light cone implements a massless Dirac cone with chirality index l=2. Figure is reproduced from the paper of Yu. H. et al., Nat. Commun. 5, 3876 (2014).

In the case of the 2D magnetoexcitons, the superposition states are described by formulas (1):

$$\left|\psi_0^{\pm}\right\rangle = c_1^{\pm}\left[\left|\psi_{ex}\left(-1;\vec{k}_{\mathrm{P}}\right)\right\rangle \pm e^{-2i\varphi}\left|\psi_{ex}\left(1;\vec{k}_{\mathrm{P}}\right)\right\rangle\right],$$

$$E_{ex}^{+}(\vec{k}_{\|}) = E_{ex}^{0}(\vec{k}_{\|}) + \varepsilon_0 + I_l\sqrt{\frac{2}{\pi}}\left|\frac{\rho_{c-v}}{l_0}\right|^2 e^{-\frac{|\vec{k}_{\|}|^2 l_0^2}{2}}\left|\vec{k}_{\|}\right| l_0.$$

$$E_{ex}^{-}(\vec{k}_{\|}) = E_{ex}^{0}(\vec{k}_{\|}) + \varepsilon_0; \quad \varepsilon_0 = -\frac{1}{2}I_l\left|\frac{\rho_{c-v}}{l_0}\right|^2; \quad l_0^2 = \frac{\mathrm{h}c}{eB}.$$

$$E_{ex}^{0}\left(\vec{k}_{\mathrm{P}}\right) = -I_l e^{-\frac{|\vec{k}_{\mathrm{P}}|^2 l_0^2}{4}} I_0\left(\frac{|\vec{k}_{\mathrm{P}}|^2 l_0^2}{4}\right); \quad I_l = \frac{e^2}{\varepsilon_0 l_0}\sqrt{\frac{\pi}{2}}, \tag{1}$$

$$\left|\Psi_1\right\rangle = \left|\Psi_{ex}(-1;\vec{k}_{\|})\right\rangle; \qquad \left|\Psi_2\right\rangle = \left|\Psi_{ex}(1;\vec{k}_{\|})\right\rangle.$$

The bare magnetoexciton states are determined by the quantum numbers $F = \pm 1$ in the way $\left|\Psi_1\right\rangle = \left|\Psi_{ex}(-1; \vec{k}_{\|})\right\rangle$; $\left|\Psi_2\right\rangle = \left|\Psi_{ex}(1; \vec{k}_{\|})\right\rangle$ and the superposition states are denoted as $\left|\Psi_0^{\pm}\right\rangle$. It is evident from Fig. 8 that the symmetric superposition state $\left|\Psi_0^{+}\right\rangle$ acquires a linear dispersion law in the range of in-plane wave vectors $\vec{k}_{\|} l_0 < 1$, where l_0 is the magnetic length. The asymmetric superposition state $\left|\Psi_0^{-}\right\rangle$ remains with the same dispersion law as the bare magnetoexciton states.

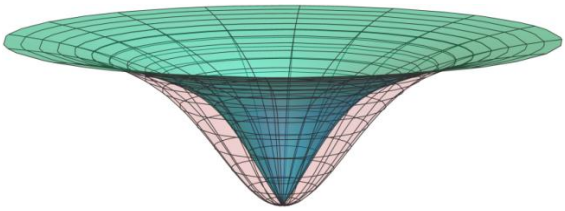

Fig. 8. Branches of 2D bright magnetoexciton in two superposition states with and without Dirac cone dispersion law.

The selection rules of the quantum transitions from the ground state of the crystal to the superposition states are discussed in the following section.

4. Selection Rules of the Optical Quantum Transitions

It is evident from Fig. 9 that the photons are propagating in any arbitrary direction of the 3D space, being characterized by circular polarizations $\vec{\sigma}_{\vec{k}}^{\pm}$. The 2D magnetoexcitons are located on the 2D plane of the layer. They are characterized by the quantum numbers $F = \pm 1$, what is equivalent to the circular polarization $\vec{\sigma}_M = (1/\sqrt{2})(\vec{a}_1 \pm i\vec{a}_2)$ with $F = M = \pm 1$. Here, $\vec{a}_1$ and $\vec{a}_2$ are the in-plane unit vectors. The selection rules of the quantum transitions from the ground state of the crystal to the superposition states depend essentially on quantum numbers n_e and n_h of the electron and hole Landau quantization levels. In the lowest Landau levels (LLLs) approximation, where only the lowest numbers $n_e = n_h = 0$ are taken into account, the geometric selection rules depend on the scalar products $(\vec{\sigma}_{\vec{k}}^{\pm} \cdot \vec{\sigma}_M^{*})$ in their different combinations. It was shown [2] that both superposition states are dipole active in the both circular polarizations. However, in the case of a symmetric state, the probability of the quantum transition depends on the direction of light propagation as regards the semiconductor layer. It has the dependence proportional to $k_z^2 / |\vec{k}|^2$, where $\vec{k} = a_3 k_z + \vec{k}_{\|}$, and a_3 is the unit vector oriented perpendicular to the layer surface. It is maximal in the Faraday geometry with light wave vector $\vec{k}$ perpendicular to the surface of the layer and vanishes in the Voigt geometry with the light propagation along the layer surface. This dependence on light wave vector projection k_z does not mean the appearance of a quadrupole quantum transition. It would be characterized by the quadratic dependence on the magnetoexciton in-plane wave vector $\vec{k}_{\|}$ and would be looking as $|\vec{k}_{\|}|^2 l_0^2$. In the case of an asymmetric superposition state, the probability of the quantum transition does not

depend on the direction of light propagation at all. These results are shown in Fig. 10.

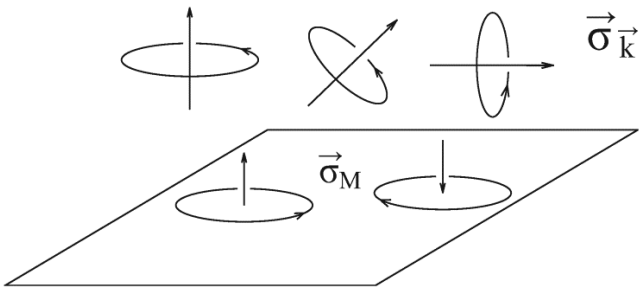

$$\vec{\sigma}_{\vec{k}}^{\pm} = \frac{1}{\sqrt{2}}\left(\vec{e}_{k,1} \pm i\vec{e}_{k,2}\right);$$

$$\vec{\sigma}_M = \frac{1}{\sqrt{2}}\left(\vec{a}_1 \pm i\vec{a}_2\right).$$

$$\left|(\vec{\sigma}_{\vec{k}}^{\pm} \cdot \vec{\sigma}_M^{*})\right|^2$$

Fig. 9. Circular polarizations of the photons and the 2D excitons. The geometric selection rules are determined by factors $\left|(\vec{\sigma}_{\vec{k}}^{\pm} \cdot \vec{\sigma}_M^{*})\right|^2$. The figure is reproduced from [7].

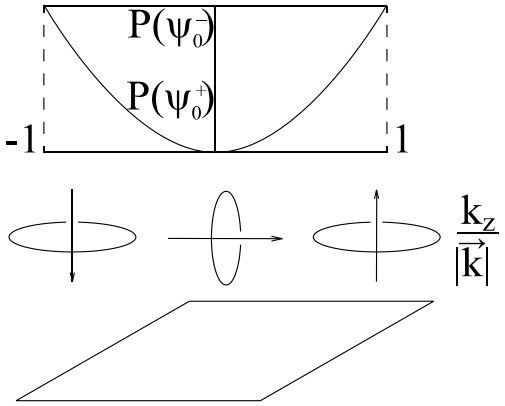

Fig. 10. Selection rules of the quantum transitions in both circular polarizations from the ground state of the crystal to the superposition magnetoexciton states $\left|\psi_0^{\pm}\left(\vec{k}_{\text{P}}\right)\right\rangle$.

We will now discuss the case of light with linear polarizations $\vec{s}_{\vec{k}}$ and $\vec{t}_{\vec{k}}$ shown in Fig. 11.

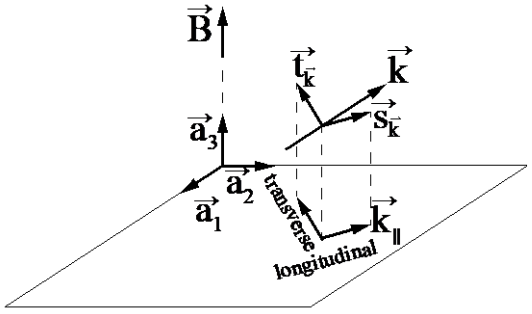

Fig. 11. Selection rules of the quantum transitions in two linear polarizations.

The probability of quantum transitions depends on the projections of the linear polarization vector $\vec{s}_k$ and $\vec{t}_k$ on the plane of the layer, especially on the fact whether they are longitudinal or transverse as regards the exciton in-plane wave vector $\vec{k}_{||}$. The symmetric superposition state is dipole active in the linear polarization $\vec{s}_k$ with a longitudinal projection and forbidden in the linear light polarization $\vec{t}_k$ with a transverse projection. As in the case of circular polarizations, the probability of quantum transitions is proportional to $k_z^2/|\vec{k}|^2$. The asymmetric superposition state is dipole active in the linear polarization $\vec{t}_k$ with a transverse projection and forbidden in the $\vec{s}_k$ polarization, and it does not depend on the light orientation. The probabilities of quantum transitions in the exciton states of the TMDC monolayers under the action of the linearly polarized light also depend on the projections of the polarization vectors on the surface of the monolayers, as in the case of the 2D magnetoexcitons. More so, this marvelous property has been first discussed and underlined by the authors of theoretical and experimental studies published in [1].

5. Conclusions

The influence of the e–h exchange Coulomb interaction on the superposition states formed by two 2D magnetoexciton with quantum numbers $F = \pm 1$, as well as by two valley Wannier–Mott excitons created in the TMDC monolayers, leads to the arising of new superposition exciton states with Dirac cone dispersion laws. A necessary condition for the implementation of this property is the interdependence between the center-of-mass and the relative e–h motions. In the case of magnetoexcitons, this interdependence is induced by the Lorentz force, whereas in the case of TMDCs, it is attributed to the existence and superposition of the exciton states in two equivalent valleys $\vec{K}$ and $-\vec{K}$ of the hexagonal Brillouin zone.

References

[1] Y. Hongyi, L. Gui-Bin, G. Pu, X. Xiaodong and Y. Wang, Nat. Commun. 5, 3876 (2014).doi: 10.1038/ncomms4876
[2] S. Moskalenko, I. Podlesny, I. Zubac and B. Novikov, Solid State Commun. 302, 113714 (2019).
[3] S.A. Moskalenko and D.W. Snoke, Bose-Einstein Condensation of Excitons and Biexcitons and Coherent Nonlinear Optics with Excitons, Cambridge University Press, New York, 2000, p. 189.
[4] P.C. Hohenberg. Phys. Rev. 158, 383(1967). https://doi.org/10.1103/PhysRev.158.383
[5] H. Deng, H. Haug, and Y. Yamamoto, Rev. Mod. Phys. 82, 1489 (2010). https://doi.org/10.1103/RevModPhys.82.1489
[6] S.A. Moskalenko and I.M. Tiginyanu, Low Temperature Physics/Fizika Nizkikh Temperatur, 42, 5, 426-437 (2016). https://doi.org/10.1063/1.4948615
[7] S.A. Moskalenko et al., Phys. Rev. B 79, 125425 (2009).https://doi.org/10.1103/PhysRevB.79.125425
[8] S.A. Moskalenko et al., Solid State Commun. 283, 14(2018).https://doi.org/10.1016/j.ssc.2018.08.005.

ELECTRONIC DENSITY OF STATES IN STRONGLY ANISOTROPIC SYSTEMS IN THE PHASE OF COEXISTENCE OF MAGNETISM AND SUPERCONDUCTIVITY IN AN EXTERNAL MAGNETIC FIELD

M. E. Palistrant, I. D. Cebotari, and S. A. Palistrant

Institute of Applied Physics, Academiei str. 5, Chisinau, MD-2028 Republic of Moldova
E-mail: chebotar.irina@gmail.com

(Received April 17, 2019)

Abstract

A method for calculating the electronic density of states in the "mixed phase"—superconductivity (SC) and the magnetic state of the spin-density wave (SDW)—is proposed. The main mechanism for the appearance of this phase is considered to be the doping of the system and allowance for the lattice structure (umklapp processes). The effect of an external magnetic field and the possibility of increasing the superconducting transition temperature T_c are analyzed.

1. Introduction

Numerous experimental studies of the properties of modern high-temperature materials demonstrate a surprising property: magnetism accompanies superconductivity; superconductivity (SC) arises either against the background of a state of a spin density wave (SDW) or after the suppression of magnetism because of doping. Modern high-temperature materials contain a number of features in the electronic energy spectrum, namely: it is a multiband system (several energy bands are present on the Fermi surface). Herewith, each compound is characterized by a certain number of these bands, which can only be electronic, only of the hole-type, or alternate between the two in different ratios. This situation requires a separate approach, when considering compounds from the class of ferropnictides and ferrochalcogenides; different ideas about the mechanism of the appearance of SC in these systems are emerging (reviews of the works in [1–3]). At present, an agreement has been reached that, in systems with electron bands on the Fermi surface (FeAs plane is responsible for SC), the main mechanism of interaction in the appearance of superconductivity is the spin fluctuations. In other compounds with a basic superconducting plane FeSe, this mechanism cannot be implemented because of the lack of "nesting" in the electronic energy spectrum and the absence of a magnetic exchange interaction. In this case [3], the cause of high-temperature superconductivity is the numerous interband electron–electron interactions in a rarefied BCS type system [4]. It is of interest that, in modern high-temperature superconductors, phase transitions are observed, for example, the commensurate–incommensurate state of a spin density wave. As a result, a displacement of the dielectric gap relative to the Fermi level and the transition to a gapless magnetic system occur in these materials.

Another approach related to the role of the Fermi surface is given in [5, 6], which is based on the accounting of the changes of parameters (when doping) such as the change in the difference in the areas of the cavities of the Fermi surface of the bands under consideration and of the deviations from ellipticity.

As in our above-mentioned works and in [5, 6], the appearance of superconductivity near the temperature of the magnetic transition is essential for the appearance of a "mixed" phase (SC+ SDW). As noted above, the thermodynamic properties of this state are studied in both quasi-1D and -2D cases. Of undoubted interest are the kinetic properties of these systems. In the study of kinetic characteristics, an important step is to determine the electronic density of states in the mixed phase of two long-range orderings: superconductivity and the spin-density wave state. This paper is focused on this problem.

2. Hamiltonian of the System and Main Definitions

In the mean-field approximation, the Hamiltonian of the system under consideration has the form

$$\mathrm{H} = \mathrm{H}_0 + \mathrm{H}_{BCS} + \mathrm{H}_{SDW} + \mathrm{H}_{H_0}, \tag{1}$$

where

$$\begin{aligned}
\mathrm{H}_0 &= \sum_{k\alpha}\left[\left(\varepsilon(\vec{k}) - \mu\right) a^{\dagger}_{\vec{k}\alpha}\, a_{\vec{k}\alpha}\right], \\
\mathrm{H}_{BCS} &= \Delta\sum_{k}\left(a^{\dagger}_{\vec{k}\uparrow}\, a^{\dagger}_{-\vec{k}\downarrow} + h.c.\right), \\
\mathrm{H}_{SDW} &= -M\sum_{\vec{k},\alpha,\beta}\left(\sigma^{i}\right)_{\alpha\beta}\left(a^{\dagger}_{\vec{k}a}\, a_{\vec{k}+\vec{Q},\beta} + h.c.\right), \\
\mathrm{H}_{H_0} &= -\sum_{\vec{k},\alpha,\beta} H_0\left(\sigma^{z}\right)_{\alpha\beta} a^{\dagger}_{\vec{k}\alpha}\, a_{\vec{k}\beta}.
\end{aligned} \tag{2}$$

Expression (1) contains terms responsible for superconductivity, magnetism, and the interaction of electrons with an external magnetic field. We chose representation in which we have a parallel magnetic field ($\vec{H}_0 \parallel \vec{M}$) for $i = z$ and a perpendicular magnetic field ($\vec{H}_0 \perp \vec{M}$) for $i = x$, Q is the wave vector of SDW; σ is the Pauli matrix:

$$\sigma^{x} = \begin{pmatrix} 0 & 1 \\ -1 & 0 \end{pmatrix}; \quad \sigma^{z} = \begin{pmatrix} 1 & 0 \\ 0 & -1 \end{pmatrix}. \tag{3}$$

In expression (2), $a^{\dagger}_{\vec{k}\alpha}$ and $a_{\vec{k}\alpha}$ are the creation and annihilation operators of electrons with momentum $\vec{k}$ and projection of spin $\alpha = \uparrow, \downarrow$, μ is the deviation from the middle filling of the energy band and $\varepsilon(\vec{k})$ is the energy of electron. The Δ and M quantities are the superconducting and magnetic order parameters:

$$\begin{aligned}
\Delta &= VT\sum_{\vec{k},\omega_n} F^{\downarrow\uparrow}_{-\vec{k}\vec{k}}(\omega_n), \\
M &= \frac{1}{2} IT\sum_{\vec{k},\omega_n,\alpha}\left(\sigma^{z}\right)_{\alpha\alpha} G^{\alpha\alpha}_{\vec{k}-\vec{Q},\vec{k}}(\omega_n), \\
\omega_n &= \left(2n+1\right)\pi T, \quad n = \pm 1, \pm 2, \ldots
\end{aligned} \tag{4}$$

Here, V and I are the BCS and exchange interaction constants, respectively; $F^{\downarrow\uparrow}_{-kk}$ and $G^{\alpha\alpha}_{k-Q,k}$ are the Fourier representations of the temperature Green's functions (anomalous and normal, respectively), ω_n – the Matsubara frequency, and T is the temperature.

We consider a quasi-1D system with the dispersion law:

$$\varepsilon(\mathrm{k}) = -W\cos kd, \tag{5}$$

where W is the half-width of the energy band and d is the lattice constant. With the middle filling of the energy band $\mu = 0$ and the external magnetic field $H_0 = 0$, the nesting condition is satisfied:

$$\varepsilon(k) = -\varepsilon(k + Q_0) \tag{6}$$

Herewith, the quasi-1D system is in the magnetic state of the SDW with the wave vector $Q_0 = \pi/d$. The deviation from the middle filling of the energy band $\mu \neq 0$, as well as the inclusion of an external magnetic field $\vec{H}_0$, violate the nesting condition; as a result, there are phase transitions of the commensurable–incommensurable state of the SDW; an order parameter that determines this incommensurability arises. Herewith, the dielectric gap shifts with respect to the Fermi surface, and the magnetic system transits into a gapless state: free carriers appear on the Fermi surface; as a result, the coexistence of superconductivity and magnetism is possible.

This mechanism for the appearance of superconductivity against the background of magnetism has been studied, for example, in our works [3, 7, 8]. In these papers, the thermodynamic properties of doped systems of reduced dimensionality are mostly analyzed. A further stage of the research consists in a more detailed study of the effect of an external magnetic field on the thermodynamic properties of the systems under consideration and the study of the effect of the lattice structure (umklapp process) on the kinetic characteristics of the mixed state (SC + SDW). The first step to solve this problem is to calculate the density of electronic states. We start from the mean-field approximation. This approach is possible, if we consider a three-dimensional system in which the motion of electrons is one-dimensional. The three-dimensionality of the system cancels the existing fluctuations, which makes it possible to apply the mean-field theory (justification see in our above works). In Hamiltonian (1), the parameters of the magnetic M and superconducting Δ long-range orders are determined by equations (4). Applying the method of temperature Green's functions [9] based on Hamiltonian (1), we obtain for the introduced Green's functions in the case of a parallel magnetic field $\vec{H}_0 \| \vec{M}$ the following expressions:

$$G^{\uparrow\uparrow}_{kk}(\omega_n) = -\frac{\left\{(i\omega_n + H_0 + \varepsilon_1)\left[-(i\omega_n + H_0)^2 + \varepsilon_2^2 + \Delta^2\right] + M^2(i\omega_n + H_0 - \varepsilon_2)\right\}}{D_{H_0}\omega_n},$$

$$F^{\downarrow\uparrow}_{-kk} = \frac{\Delta\left\{-(i\omega_n + H_0)^2 + \varepsilon_2^2 + \Delta^2 - M^2\right\}}{D_{H_0}(\omega_n)}, \tag{7}$$

$$G^{\sigma\sigma}_{k-Q,k}(\omega_n) = \sigma\frac{M[M^2 - \Delta^2 - (i\omega_n + H_0 + \varepsilon_1)(i\omega_n + H_0 + \varepsilon_2)}{D_{H_0}(\omega_n)}.$$

Here

$$D_{(H_0)}(\omega_n) = (i\omega_n + H_0)^4 - (i\omega_n + H_0)^2(\varepsilon_1^2 + \varepsilon_2^2 + 2M^2 + 2\Delta^2) + \\ + \varepsilon_1^2\varepsilon_2^2 - 2M^2\varepsilon_1\varepsilon_2 + \Delta^2\left(\varepsilon_1^2 + \varepsilon_2^2\right) + \left(M^2 - \Delta^2\right)^2. \quad (8)$$

Substituting necessary Green's functions (7) into expressions (4), we obtain a system of equations for order parameters Δ and M. One can solve this system numerically for given values of parameters μ and H_0. First, we should choose 1D or 2D cosine law of dispersion and convert from summation over $\vec{k}$ to integration with respect to energy, taking into account the transition of the system to the incommensurate state of the SDW (see, e.g., [3, 7, 8]). Below, we present a method for taking into account the umklapp processes associated with a change in the wave vector of a spin density wave $Q \neq 2k_F$ of a quasi-1D system.

3. Calculation of the Density of Electronic States

The relation determines the density of electronic states with allowance for umklapp processes and in the presence of an external magnetic field ($\vec{H}_0 \| \vec{M}$):

$$N^{\uparrow}(\omega) = N_N^{\uparrow}(\omega) + N_u^{\uparrow}(\omega), \quad (9)$$

where $N_N^{\uparrow}(\omega)$ is determined by the normal processes and $N_u^{\uparrow}(\omega)$ by the umklapp processes in the magnetic field H_0 chosen in the direction $\vec{M}$.

We first consider normal processes:

$$N_N^{\uparrow}(\omega) = \frac{1}{\pi} \sum_{q<k<Q_0} \mathrm{Im} G_{kk}^{\uparrow\uparrow}(z)\Big|_{z=\omega-i\delta}. \quad (10)$$

The domain of sum in formula (10) is determined by the conditions $|k| < Q_0$ and $|k - Q| < Q_0$, where $Q = Q_0 + q$ ($q = k_F$).

In accordance with (7), we have

$$G_{kk}^{\uparrow\uparrow}(z) = -\frac{D_1(H_0, z)}{D(H_0, z)}, \quad (11)$$

where

$$D_1(H_0, z) = \left[z + H_0 + \varepsilon_1\right]\left[-\left(z + H_0\right)^2 + \varepsilon_2^2 + \Delta^2\right] + M^2\left(z + H_0 - \varepsilon_2\right),$$

$$D(H_0, z) = \left(z + H_0\right)^4 - \left(z + H_0\right)^2[\left(\varepsilon_1^2 + \varepsilon_2^2 + 2M^2 + 2\Delta^2\right) + \\ + \varepsilon_1^2\varepsilon_2^2 - 2M^2\varepsilon_1\varepsilon_2 + \Delta^2\left(\varepsilon_1^2 + \varepsilon_2^2\right) + \left(M^2 - \Delta^2\right)^2,$$

$$\varepsilon_1 = \varepsilon_k^r - \mu, \quad \varepsilon_2 = \varepsilon_{k-Q}^r - \mu,$$

To perform the integration in (10), we use the cosine law (5), representing ε_1 and ε_2 as follows:

$$\varepsilon_1 = \varepsilon_{k-q/2}\cos\frac{qd}{2} - \mu_{\pm} = \varepsilon - \mu_{\pm},$$
$$\varepsilon_2 = -\left[\varepsilon_{k-q/2}\cos\frac{qd}{2} + \mu_{\pm}\right] = -\left(\varepsilon + \mu_{\pm}\right), \tag{12}$$
$$\mu_{\pm} = \mu \pm \eta, \quad \eta = W\sin\frac{qd}{2}.$$

We will consider small deviations of the wave vector of the spin density wave from $2k_f$ ($q/2k_F << 1$); therefore, we will assume $\sin(\frac{qd}{2}) \approx \frac{qd}{2}$; $\cos(\frac{qd}{2}) \approx 1$.

We substitute (11) into (10) and reduce $N_N^{\uparrow}(\omega)$ to the form:

$$N_N^{\uparrow}(\omega) = \frac{1}{2\pi^2}\,\mathrm{Im}\int_{-W_1}^{W_1} N(\varepsilon_{k-q/2})\,d\,\varepsilon_{k-q/2}\,\left.\frac{D_1\left(\varepsilon_{k-q/2},\ H_0,\ \mu_-\right)}{D_{H_0}\left(\varepsilon_{k-q/2},\ H_0,\ \mu_-\right)}\right|_{z=\omega-i\delta} \tag{13}$$

where

$$W_1 = W\cos\frac{qd}{2}, \quad N(\varepsilon_{k-q/2}) = \frac{1}{d\sqrt{W^2 - \varepsilon_{k-q/2}^2}} \tag{14}$$

The account of umklapp processes reduces to additional summation over the domain $-Q_0 < k < q$, that is

$$N_u^{\uparrow}(\omega) = \frac{1}{2\pi^2}\int_{-Q_0}^{q} dk\ \mathrm{Im}G_{kk}^{\uparrow\uparrow}(z)\big|_{z=\omega-i\delta} \tag{15}$$

The domain of integration in this expression is conveniently divided into three sections: $-Q_0 < k < -Q_0 + \frac{q}{2}$, $-Q_0 + \frac{q}{2} < k < \frac{q}{2}$ and $\frac{q}{2} < k < q$.

In the first and last terms, we proceed to integration with respect to $\varepsilon_{k-q/2}$; in the second term of this expression, we replace k by $-k$ and then proceed to integration over $\varepsilon_{k+q/2}$. As a result, expression (15) has the form:

$$\begin{aligned} N_u^{\uparrow}(\omega) = {} & \frac{1}{2\pi^2}\,\mathrm{Im}\int_{-W_1}^{W} d\varepsilon_{k-q/2}\,N\left(\varepsilon_{k-q/2}\right)\left.\frac{D_1\left(\varepsilon_{k-q/2},\ H_0,\mu_-\right)}{D_{H_0}\left(\varepsilon_{k-q/2},\ H_0,\mu_-\right)}\right|_{z=\omega-i\delta} + \\ & + \frac{1}{2\pi^2}\,\mathrm{Im}\int_{-W}^{W} N\left(\varepsilon_{k+q/2}\right)d\,\varepsilon_{k+q/2}\left.\frac{D_1\left(\varepsilon_{k+q/2},\ H_0,\ \mu_+\right)}{D_{H_0}\left(\varepsilon_{k+q/2},\ H_0,\mu_+\right)}\right|_{z=\omega-i\delta} + \\ & + \frac{1}{2\pi^2}\,\mathrm{Im}\int_{-W}^{-W_1} N\left(\varepsilon_{k-q/2}\right)d\varepsilon_{k-1/2}\left.\frac{D_1\left(\varepsilon_{k-q/2},\ H_0,\ \mu_-\right)}{D_{H_0}\left(\varepsilon_{k-q/2},\ H_0,\ \mu_-\right)}\right|_{z=\omega-i\delta} \end{aligned} \tag{16}$$

Based on (13) and (16) for total electronic density of states taking into accounts both normal and umklapp processes, we obtain the following expression:

$$N^{\uparrow}(\omega)=\frac{1}{2\pi^2 dW\cos\frac{dq}{2}}\,\mathrm{Im}\left(\int_{-W}^{W}d\varepsilon\,\frac{D_1(\varepsilon,H_0,\mu_-)}{D_{H_0}(\varepsilon,H_0,\mu_-)}+\right.$$
$$\left.+\int_{-W}^{W}d\varepsilon\,\frac{D_1(\varepsilon,\ H_0,\ \mu_+)}{D_{H_0}(\varepsilon,\ H_0,\ \mu_+)}\right)\Bigg|_{z=\omega-i\delta} \tag{17}$$

In expression (17), we perform integration in the complex domain closing the integration contour in the upper half-flatness. As a result, we obtain:

$$N^{\uparrow}(\omega)=\frac{1}{4\pi dW\cos\frac{qd}{2}}\ \mathrm{Re}\ \left\{I(z,H_0,\mu_-)+I(z,H_0,\mu_+)\right\}\Big|_{z=\omega-i\delta} \tag{18}$$

where

$$I(z,H_0,\mu_\pm)=\frac{C(z,H_0,\mu_\pm)}{B(z,H_0,\mu_\pm)}\cdot$$
$$\cdot\left[\frac{1}{\sqrt{A(z,H_0,\mu_\pm)+B(z,H,\mu_\pm)}}-\frac{1}{\sqrt{A(z,H_0,\mu_\pm)-B(z,H_0,\mu_\pm)}}\right]-$$
$$-(z+H_0+\mu_\pm)\left[\frac{1}{A(z,H_0,\mu_\pm)+B(z,H_0,\mu_\pm)}+\frac{1}{\sqrt{A(z,H_0,\mu_\pm)-B(z,H_0,\mu_\pm)}}\right], \tag{19}$$
$$A(z,H_0,\mu_\pm)=(z+H_0)^2+\mu_\pm{}^2-M^2-\Delta^2,$$

Let us write the square roots in the above expressions in accordance with their definition:

$$\sqrt{a+ib}=\frac{sign\,b}{\sqrt{2}}\left[a+\sqrt{a^2+b^2}\right]^{1/2}+\frac{i}{\sqrt{2}}\left[\sqrt{a^2+b^2}-a\right]^{1/2} \tag{20}$$

We proceed to the representation $z=\omega-i\delta$, using the definition of the square roots (20). As a result, we reduce the total electronic density of states to the form:

$$\frac{N(\omega)}{N_0}=Re\left\{I(\omega,H_0,\mu_-)+I(\omega,H_0,\mu_+)\right\} \tag{21}$$

where

$$I(\omega,H_0,\mu_\pm)=\frac{C}{B}\left[F_1-F_2\right]-\left[\omega+H_0+\mu_\pm\right]\cdot\left[F_1+F_2\right],$$

$$C=C\left(\omega,H_0,\mu_\pm\right)=-2\,\mu_\pm\left(\omega+H_0\right)\left(\omega+H_0+\mu_\pm\right)+2\mu_\pm{}^2, \tag{22}$$

$$B=B\left(\omega,H_0,\mu_\pm\right)=-2\,sign\left(\omega+H_0\right)^2\left[\mu_\pm{}^2\left(\omega+H_0\right)+M^2\Delta^2-\mu_\pm{}^2\Delta^2\right]^{1/2},$$

$$F_1=F_1\left(\omega,H_0,\mu_\pm\right)=-sign\left[\omega+H_0-\frac{\mu_\pm\left(\omega+H_0\right)}{\sqrt{\mu_\pm{}^2\left(\omega+H_0\right)^2+M^2\Delta^2-\mu_\pm{}^2\Delta^2}}\right]\cdot$$

$$\cdot\left[\left(\omega+H_0\right)^2+\mu_\pm{}^2-M^2-\Delta^2+B\right]^{-1/2},$$

$$F_2=F_2\left(\omega,H_0,\mu_\pm\right)=-sign\left[\omega+H_0+\frac{\mu_\pm\left(\omega+H_0\right)}{\sqrt{\mu_\pm{}^2\left(\omega+H_0\right)^2+M^2\Delta^2-\mu_\pm{}^2\Delta^2}}\right]\cdot$$

$$\cdot\left[\left(\omega+H_0\right)+\mu_\pm{}^2-M^2-\Delta^2\right]-B\Big]^{-1/2},$$

$$N_0=4\pi dW\cos\frac{\pi d}{2}$$

Expressions (18)–(22) determine the electronic density of states in the mixed phase (SC + SDW) for a given value of the external magnetic field H_0 and the deviation from the middle filling of the energy band μ in the phase of coexistence of superconductivity and the incommensurate state of SDW due to an external magnetic field H_0 and the deviation of vector of a spin density wave from $2k_F$. In detail, one can obtain further calculations in general only by numerical methods. The problem becomes simpler, if we consider the nucleation of weak superconductivity against the background of the SDW. In this case, we pass to the limiting transition $\Delta << M$.

As a result, we obtain

$$\frac{N\left(\omega\right)}{N_0}=\mathrm{Re}\left\{\frac{\left|\omega+H_0+\mu_-\right|}{\sqrt{\left(\omega+H_0+\mu_-\right)^2-M^2}}+\frac{\left|\omega+H_0+\mu_+\right|}{\sqrt{\left(\omega+H_0+\mu_+\right)^2-M^2}}\right\} \tag{23}$$

It follows that N (ω) ≠ 0, if $\left|\omega+H_0+\mu_-\right|<|\mathrm{M}|$ and $\left|\omega+H_0+\mu_+\right|<|M|$. For temperature higher then critical temperature of SC transition T_c, we have the state of the SDW.

Let us consider some limiting cases:

1. H_0=0, $\mu_\pm=\mu\pm\eta$, $\eta=0$. The system is in a dielectric state (in the commensurate state of the SDW), the nesting condition (6) is satisfied.
2. H_0 =0, $\mu_\pm=\mu\pm\eta$, $\eta\neq0$

For $\mu=\mu_c$ the system goes to the phase of the incommensurate state of the spin density wave with incommensurability parameter η. In the domain $\mu>\mu_c$, an ambiguous correspondence arises between the temperature of the magnetic transition T_M and μ; that is, the state of the SDW becomes unstable. The phase transition to the incommensurate state of the SDW, taking into account the umklapp processes, contributes to the stabilization of the state by transition to a semi

metallic state ($Q \neq 2k_F$, $\eta \neq 0$). There is a possibility of the appearance of superconductivity.

The inclusion of an external magnetic field makes a definite contribution to the η value; consequently, in a definite range of magnetic field values, it accelerates the transition to the above-mentioned metallic state and, accordingly, leads to an increase in the superconducting transition temperature. The same situation occurs when the charge density wave and superconductivity arise in the system (see, e.g., [10]). Consequently, in strongly anisotropic systems in the phase of coexistence of superconductivity and spin density wave, as well as superconductivity and charge density wave, the temperature of the superconducting transition can increase with increasing external magnetic field.

4. Conclusions

Using the Green's function method, we have determined the electronic density of states of a quasi-1D system in the mixed phase of the coexistence of superconductivity and the incommensurable state of the spin density wave in the presence of an external magnetic field. Herewith, we have taken into account the effect of the umklapp processes (lattice structure). Under the assumption of the generation of weak superconductivity against the background of the SDW, we have analyzed various limiting cases. As a result, we have discussed the possibility of implementing the mixed phase of the incommensurate state of SDW with superconductivity. We have shown that the inclusion of an external magnetic field of a certain range contributes to an increase in the temperature of the superconducting transition. This is an unusual and surprising picture illustrating the favorable effect of an external magnetic field on superconductivity.

References

[1] A.V. Chubukov and P.J. Hirchjeld, Physics Today 68, 46 (2016); arXiv: 14127104 v1.
[2] M.V. Sadovskii, Usp. Fiz. Nauk 186, 1035 (2016); Phys. Usp. 59 (10), 947 (2016).
[3] M.E. Palistrant, Zh. Exp. Teor. Fiz. 150, 97 (2016); JETP, 123, 86 (2016).
[4] F.G. Kochorbe and M.E. Palistrant, Teor. Mat. Fiz., 96, 459 (1993); Theor. and Math. Phys., 96, 1083, (1996); Zh. Exp. Teor. Fiz. 104, 3084, (1993); JETP, 77, 442 (1993).
[5] A. B. Vorontsov, M.G. Vavilov, and A.B. Chubrikov, Phys. Rev. B 81, 174538 (2010); arXiv: 1003.2389.
[6] D. Kuzmanovski, A. Jevchenko, M. Khotes, and M.G. Vavilov, Phys. Rev. B 89, 144503 (2014); arXiv: 1401.1118.
[7] V.A. Moskalenko, L.Z. Kon, and M.E. Palistrant, Nizkotemperaturnyye svoystva metallov s osobennostyami zonnogo spektra, Stiinta, Kishinev, 1989.
[8] V.A. Moskalenko, L.Z. Kon, M.E. Palistrant, Teoria supraconductibilitatii multi-banda, Editura tehnica, Bucuresti, 2008.
[9] A.A. Abrikosov, L. P. Gorkov, and I.E. Dzyaloshinski, Metody kvantovoy teorii polya v statisticheskoy fizike, Gos. Izd. Fiz. Mat. Lit., Moscow, 1962.
[10] V.M. Vackalyuk, M.E. Palistrant, and I.V. Padure, J. Phys. Condens. Matter 2, 2699 (1990).

PEIERLS STRUCTURAL TRANSITION IN ORGANIC CRYSTALS OF THE TTT_2I_3 TYPE IN A 2D APPROXIMATION

S. Andronic and A. Casian

Technical University of Moldova, Stefan cel Mare Avenue 168, Chisinau, MD-2004 Republic of Moldova
E-mail: andronic_silvia@yahoo.com

(Received May 29, 2019)

Abstract

The metal–insulator transition of the Peierls type is studied in organic crystals of tetrathiotetracene iodide with the lowest carrier concentration value in a 2D approximation. The two most important electron–phonon interaction mechanisms—of the deformation potential type and the polaron type—are considered. The dynamical interaction of carriers with defects is also taken into account. The renormalized phonon spectrum is calculated; it is shown that the transition is of the Peierls type.

1. Introduction

In the last years, quasi-one-dimensional (Q1D) organic crystals have attracted increasing attention in the scientific world due to more diverse and, in many cases, unusual properties exhibited by them. Organic nanomaterials have large potential applications in electronic, sensing, energy-harnessing, and quantum-scale systems [1]. It was also shown that highly conducting Q1D organic crystals can have extremely promising thermoelectric applications. Since not all parameters of these materials are well known, it is very important to apply different methods—both theoretical and experimental—to determine some of them. In this paper, we study the Peierls structural transition for this purpose.

This phenomenon was theoretically predicted by Rudolf Peierls. According to Peierls, at some lowered temperatures, a one-dimensional metallic crystal with a half filled conduction band has to pass in a dielectric state with a dimerized crystal lattice. This temperature is referred to as the Peierls critical temperature. The Peierls transition was studied by many authors [2–5]. To the best of our knowledge, the Peierls transition in tetrathiotetraceneiodide (TTT_2I_3) crystals has not been studied either theoretically, or experimentally. This material was synthesized independently and nearly simultaneously by the authors of [6–9] with the aim to find superconductivity in a low-dimensional conductor. At the same time, these crystals with the lowering temperature show a metal-dielectric transition. Earlier [10] we have shown for a crystal with a highest carrier concentration and the $TTT_2I_{3.1}$ composition that the transition is of the Peierls type.

For these crystals, the dimensionless Fermi momentum $k_F = 0.517\pi/2$. In this case, it was found that the Peierls transition begins at $T \sim 35$ K in TTT chains and considerably reduces the electrical conductivity. Due to interchain interaction, the transition is completed at $T \sim 19$ K.

The authors of [12] studied a 3D physical crystal model for the same curve. It was found that the transition begins at $T \sim 35$ K in TTT chains and is completed at $T \sim 9.8$ K, as observed

experimentally.

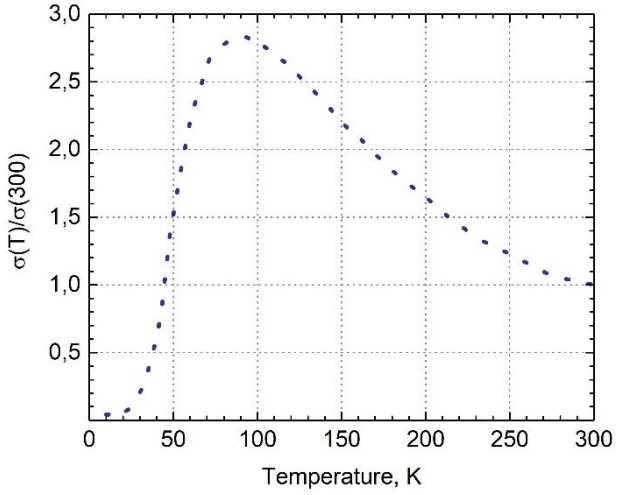

Fig. 1. Temperature dependence of electrical conductivity of the TTT2I3+δ crystal, δ = 0.01. Max – 90 K, σ → 0 at 20 K [10].

In this paper, we will study the behavior of the Peierls transition in TTT_2I_3 crystals with the lowest carrier concentration value. For simplicity, we will apply the 2D approximation. We will analyze the Peierls structural transition for the curve shown in Fig. 1. The dimensionless Fermi momentum in this case is k_F=0.502π/2. In addition, the Peierls critical temperature T_p is determined.

2. Physical Model of Crystals

The physical model of crystals was described in more detail in [11]. The Hamiltonian of the 2D crystal model in the tight binding and nearest neighbor approximations has the form

$$H = \sum_{\boldsymbol{k}} \varepsilon(\boldsymbol{k}) a_{\boldsymbol{k}}^{+} a_{\boldsymbol{k}} + \sum_{\boldsymbol{q}} \eta \omega_{\boldsymbol{q}} b_{\boldsymbol{q}}^{+} b_{\boldsymbol{q}} + \sum_{\boldsymbol{k},\boldsymbol{q}} A(\boldsymbol{k},\boldsymbol{q}) a_{\boldsymbol{k}}^{+} a_{\boldsymbol{k}+\boldsymbol{q}} (b_{\boldsymbol{q}} + b_{-\boldsymbol{q}}^{+}) \tag{1}$$

Here, the first term is the energy operator of free holes in the periodic field of the lattice. The hole energy is measured from the band top; it is presented in the following form:

$$\varepsilon(\boldsymbol{k}) = -2w_1(1-\cos k_x b) - 2w_2(1-\cos k_y a) \tag{2}$$

where w_1 and w_2 are the transfer energies of a hole from one molecule to another along the chain (x direction) and perpendicular to it (y direction).

In Eq. (1) $a_{\boldsymbol{k}}^{+}$, $a_{\boldsymbol{k}}$ are the creation and annihilation operators of the hole with a 2D quasi-wave vector $\boldsymbol{k}$ and projections (k_x, k_y); $b_{\boldsymbol{q}}^{+}$, $b_{\boldsymbol{q}}$ are creation and annihilation operators of an acoustic phonon with 2D wave vector $\boldsymbol{q}$ and frequency $\omega_{\boldsymbol{q}}$.

The second term in the Eq. (1) is the energy operator of longitudinal acoustic phonons

$$\omega_{\boldsymbol{q}}^2 = \omega_1^2 \sin^2(q_x b/2) + \omega_2^2 \sin^2(q_y a/2) \tag{3}$$

where ω_1 and ω_2 are the limit frequencies in the x and y directions.

The third term represents the electron–phonon interactions. The two most important electron–phonon interaction mechanisms—of the deformation potential type and the polaron type—are considered. The coupling constants of the first interaction are proportional to derivatives w_1' and w_2' of w_1 and w_2, with respect to the intermolecular distances. The coupling constant of second interaction is proportional to the average polarizability of the molecule α_0.

This interaction is important for crystals composed of large molecules, such as TTT, so that α_0 is roughly proportional to the molecule volume. The ratio of amplitudes of the polaron-type interaction to the deformation potential one in the *x* and *y* directions is described by parameters γ_1 and γ_2:

$$\gamma_1 = 2e^2\alpha_0 / b^5 w_1', \ \gamma_2 = 2e^2\alpha_0 / a^5 w_2' \tag{4}$$

The square module of matrix element $A(\boldsymbol{k},\boldsymbol{q})$ from Eq. (1) can be written in the form

$$\begin{aligned} |A(\boldsymbol{k},\boldsymbol{q})|^2 = 2\eta w_1'^2 /(NM\omega_{\boldsymbol{q}}) \times \{[\sin(k_x b) - \sin(k_x - q_x, b) - \gamma_1 \sin(q_x b)]^2 + \\ d_1^2[\sin(k_y a) - \sin(k_y - q_y, a) - \gamma_2 \sin(q_y a)]^2\}. \end{aligned} \tag{5}$$

Here, M is the mass of the molecule, N is the number of molecules in the basic region of the crystal, $d_1 = w_2/ w_1 = w_2' / w_1'$.

To explain the behavior of the electrical conductivity from Fig.1, it is necessary to take into account the dynamical interaction of carriers with defects. The static interaction will give contribution to the renormalization of the hole spectrum. Defects in TTT_2I_3 crystals are formed due to different coefficients of dilatation of TTT and iodine chains.

The Hamiltonian of this interaction H_{def} is presented as follows:

$$H_{def} = \sum_{\boldsymbol{k},\boldsymbol{q}} \sum_{n=1}^{N_d} B(q_x) \exp(-iq_x x_n) a_{\boldsymbol{k}}^{+} a_{\boldsymbol{k}-\boldsymbol{q}} (b_{\boldsymbol{q}} + b_{\boldsymbol{q}}^{-}) . \tag{6}$$

Here, $B(q_x)$ is the matrix element of a hole interaction with a defect; it is represented in the form

$$B(q_x) = \sqrt{\eta/(2NM\omega_q)} \cdot I(q_x), \tag{7}$$

where $I(q_X)$ is the Fourier transformation of the derivative with respect to intermolecular distance from the energy of interaction of a carrier with a defect and x_n numbers the defects that are considered linear along the *x*-direction of TTT chains and distributed randomly:

$$I(q_x) = D(\sin(bq_x))^2, \tag{8}$$

Where *D* is a parameter that determines the intensity of hole interaction with a defect. It has the same meaning as w_1' in (5) and is measured in $\text{eV}\cdot\text{Å}^{-1}$.

The renormalized phonon spectrum $\Omega(\boldsymbol{q})$ is determined by the pole of the Green function and obtained from the transcendent dispersion equation

$$\Omega(\boldsymbol{q}) = \omega_{\boldsymbol{q}}[1 - \overline{\Pi}(\boldsymbol{q},\Omega)]^{1/2}, \tag{9}$$

where the principal value of the dimensionless polarization operator takes the form:

$$\text{Re}\,\overline{\Pi}(\boldsymbol{q},\Omega) = -\frac{4}{\eta\omega_q} \sum_{\boldsymbol{k}} \frac{\left[|A(\boldsymbol{k},-\boldsymbol{q})|^2 + |B(q_x)|^2\right](n_k - n_{k+q})}{\varepsilon(\boldsymbol{k}) - \varepsilon(\boldsymbol{k}+\boldsymbol{q}) + \eta\Omega}. \tag{10}$$

Here, n_k is the Fermi distribution function. Equation (9) can be solved only numerically.

3. Results and Discussion

Numerical simulations for the 2D physical model of the crystal are performed for the following parameters [13]: $M = 6.5 \times 10^5 m_e$ (m_e is the mass of the free electron), $w_1 = 0.16$ eV, $w_1' = 0.26$ eV·Å^{-1}, $d_1 = 0.015$, $\gamma_1 = 1.7$, γ_2 is determined from the relationship: $\gamma_2 = \gamma_1 b^5 / a^5 d_1$, $k_F = 0.502\pi/2$. The sound velocity along TTT chains was estimated by comparison of the calculated results for the electrical conductivity of TTT_2I_3 crystals [13] with the reported ones [8], $v_{s1} = 1.5 \times 10^5$ cm/s. For v_{s2} in transversal direction (in a direction) we have taken 1.35×10^5 cm/s.

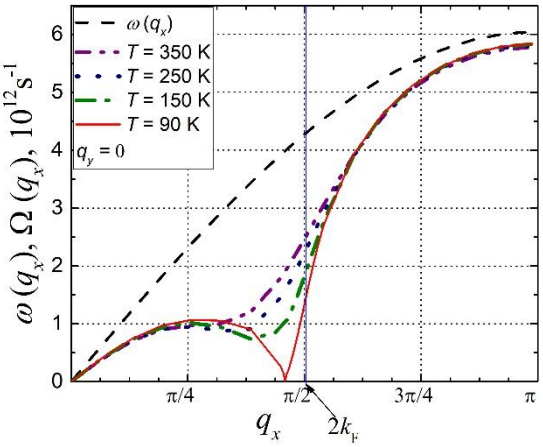

Fig. 2. Renormalized phonon spectrum $\Omega(q_x)$ for $\gamma_1 = 1.7$ and different temperatures. The dashed line is for the spectrum of free phonons. k_F=0.502 π/2, D = 1.074 eV·Å^{-1}.

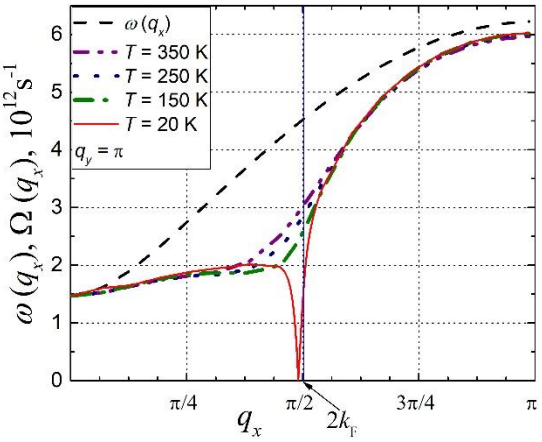

Fig. 3. Renormalized phonon spectrum $\Omega(q_x)$ for $\gamma_1 = 1.7$ and different temperatures. The dashed line is for the spectrum of free phonons. k_F=0.502π/2, D = 1.014 eV·Å^{-1}.

Figures 2 and 3 show the dependences of renormalized phonon frequencies $\Omega(q_x)$ as a function of q_x for different temperatures and different q_y values. In the same graphs, the dependences for initial phonon frequency $\omega(q_x)$ are shown. It is evident that the $\Omega(q_x)$ values are diminished in comparison with those of $\omega(q_x)$ in the absence of an electron–phonon interaction. This means that the electron–phonon interaction and structural defects diminish the values of lattice elastic constants. In addition, one can observe that, with a decrease in temperature T, the curves change their form, and a minimum appears in the $\Omega(q_x)$ dependences. This minimum becomes more pronounced at lower temperatures.

Figure 2 shows the case where $q_y = 0$ and dimensionless Fermi momentum $k_F = 0.502\pi/2$ and $D = 1.074$eV·Å^{-1}. Parameter D is a constant that determines the intensity of hole interaction with a defect. In this case, the interaction between TTT chains is neglected. The Peierls transition begins at T = 90 K. At this temperature, the electrical conductivity achieves a maximum. With the lowering temperature, the electrical conductivity decreases. Figure 3 shows the case where the interaction between TTT chains is taken into account ($q_y = \pi$), D = 1.014 eV·Å^{-1} and $k_F = 0.502\pi/2$. In this case, the transition is completed at T = 20 K. It was observed that parameter D decreases or the hole interaction with a defect is smaller in this case. It is evident from Fig. 1 that the electrical conductivity significantly decreases and achieves zero at $T \sim 20$ K.

4. Conclusions

The Peierls structural transition has been studied in existing organic crystals of TTT_2I_3 with the lowest hole concentration value. The 2D physical model has been considered. The two most important electron–phonon interaction mechanisms—of the deformation potential type and the polaron type—have been considered. The interaction of carriers with defects has been analyzed. The renormalized phonon spectrum has been calculated in the random phase approximation. The method of retarded temperature dependent Green function has been applied. It has been shown that the Peierls transition temperature strongly depends on iodine concentration. It has been found that, if $k_F = 0.502\pi/2$ and the hole concentration achieves the lowest value, the Peierls transition begins at T ~90 K in TTT chains and considerably reduces the electrical conductivity. Due to interchain interaction, the transition is completed at T ~ 20 K.

Acknowledgments

The authors express gratitude to the support of the scientific program of the Academy of Sciences of Moldova under project no. 15.817.02.22F.

References

[1] Organic Nanomaterials: Synthesis, Characterization, and Device Applications (edited by T. Torres and G. Bottari), John Wiley & Sons, Inc., Hoboken, NJ, USA, 2013.
[2] L. N. Bulaevskii, Usp. Fiz. Nauk 115, 263 (1975).
[3] M. Hohenadler, H. Fehske, and F.F. Assaad, Phys. Rev. B, 83, 115105 (2011).
[4] V. Solovyeva et al., J. Phys. D: Appl. Phys. 44, 385301 (2011).
[5] A. Chernenkaya, K. Medjanik, P. Nagel, M. Merz, S. Schuppler, E. Canadell, J. P. Pouget, and G. SchËonhense, Eur. Phys. J. B. 88, 13(2015).
[6] I.I. Buravov, G.I.Zvereva, V.F. Kaminskii, et al., Chem. Commun. 18, 720 (1976).
[7] V.F. Kaminskii, M.l. Kidekel', R.B. Lyubovskii, etal., Phys. Status Solidi A 44, 77 (1977).
[8] B. HiltiandC.W. Mayer, Helv. Chim. Acta 61, 501 (1978).
[9] L.G.Isset and E.A. Perz-Albuerene, Sol. State Comm., 21, 433 (1977).
[10] F. Shchegolev and E. B. Yagubskii, Extended Linear Chain Compounds (edited by I.S.Miller), Plenum Press, New York, 1982, vol. 2, p. 385.
[11] S. Andronic and A. Casian, Adv. Mater. Phys. Chem. 7,212 (2017).
[12] S. Andronic, I. Balmus, and A. Casian, 9th Int. Conf. on Microelectronics and Computer Science, Chisinau, Republic of Moldova, October, 19–21, 2017.
[13] A. Casian and I. Sanduleac, J. Electron. Mater. 43,3740 (2014).

LUMINESCENT PROPERTIES OF Sb-DOPED ZnSe SINGLE CRYSTALS

K. D. Sushkevich, E. P. Goncearenco, N. D. Nedeoglo, and D. D. Nedeoglo

Department of Physics and Engineering, Moldova State University, str. A. Mateevici 60, Chisinau, MD-2009 Republic of Moldova

E-mail: spacemib@gmail.com

(Received April 4, 2019)

Abstract

Photoluminescence (PL) spectra of ZnSe:0.1at%Sb single crystals are studied between 90 and 300 K. The samples are grown by the chemical vapor transport (CVT) method with iodine as a transport agent and doped with Sb impurity during the growth. A yellow PL band with a maximum at 2.16 eV (575 nm) at room temperature is observed for the first time. A model of a ($Sb_{Se}I_{Se}$) acceptor center with the energy level located at 0.52 eV above the valence band edge is proposed, and the mechanism of the formation of this yellow PL band under direct and indirect excitation is discussed.

1. Introduction

Radiative properties of ZnSe:Sb samples are studied in a series of papers [1–4]. The conclusions made in the papers about the effect of Sb impurity on the sample properties essentially differ, probably, due to the fact that the studied samples were grown by different methods and measured in different spectral ranges at different temperatures. For example, the authors of [1] argue that annealing of ZnSe samples in ~~an~~ Sb melt does not lead to the formation of Sb-based luminescence centers responsible for edge luminescence; however, it contributes to the "purification" of the samples from background impurities. At the same time, according to [2, 3], Sb impurity is considered to be responsible for the edge photoluminescence (PL) bands localized at 444, 450.5, 456.7, 461, and 463 nm. The PL bands localized at longer wavelengths at 550, 640, 760, and 820 nm are attributed to Sb impurity in [4]. Since the as-grown undoped ZnSe samples contain uncontrollable donor impurities of Group III elements in the unbound state (D_{Zn}), the authors consider $(A_{Se}D_{Zn})^{-}$ associative defects with various distances between the components to be responsible for the PL bands observed for ZnSe:Sb samples. At the same time, there are no bands in the PL spectra that can be attributed to $(A_{Se}D_{Se})^{-}$ centers [4]. Thus, it may be of interest to introduce D_{Se} donors to form $(A_{Se}D_{Se})^{-}$ luminescence centers and study their effect on PL spectra of the ZnSe:Sb samples.

2. Experimental

ZnSe and ZnSe:Sb samples were grown by the chemical vapor transport (CVT) method with iodine as a transport agent. An Sb acceptor impurity (0.01 at %) and Zn and Se components were loaded into quartz tubes, which were placed in a furnace so that the nutrient zone

temperature was 1180–1190 K and the crystallization zone temperature was 1165–1175 K. The purity of the chemical substances was as follows: 99.999% for Zn, Se, and Sb and 99.99% for I.

PL spectra were measured at 300 and 90 K in the wavelength range between 400 and 800 nm under excitation with laser radiation of 337 and 473 nm. The spectra were registered using a standard synchronous detection system with an MDR-23 monochromator and a FEU-100 photomultiplier and corrected for the spectral sensitivity of the detection system.

3. Experimental Results and Discussion

Figure 1 shows room-temperature PL spectra of ZnSe and ZnSe:Sb crystals excited with ultraviolet laser radiation (λ_{exc} = 337 nm). The PL spectrum of the undoped sample consists of three bands: the edge band localized at 2.68 eV (462 nm) with a full width at half maximum (FWHM) of 98 meV and two long-wavelength bands with maxima at 2.06 eV (600 nm) and 1.94 eV (640 nm) (Fig. 1, curve *1*). A wide FWHM for the edge PL band suggests that it has a complex structure. According to [5], free excitons, as well as free-bound transitions involving shallow donor and acceptor impurities, can be responsible for this PL band. The introduction of Sb impurity into the samples decreases the edge PL intensity (Fig. 1, curve *2*), apparently owing to a redistribution of the recombination channels in the doped sample, and does not change the shape and position of the edge PL spectrum.

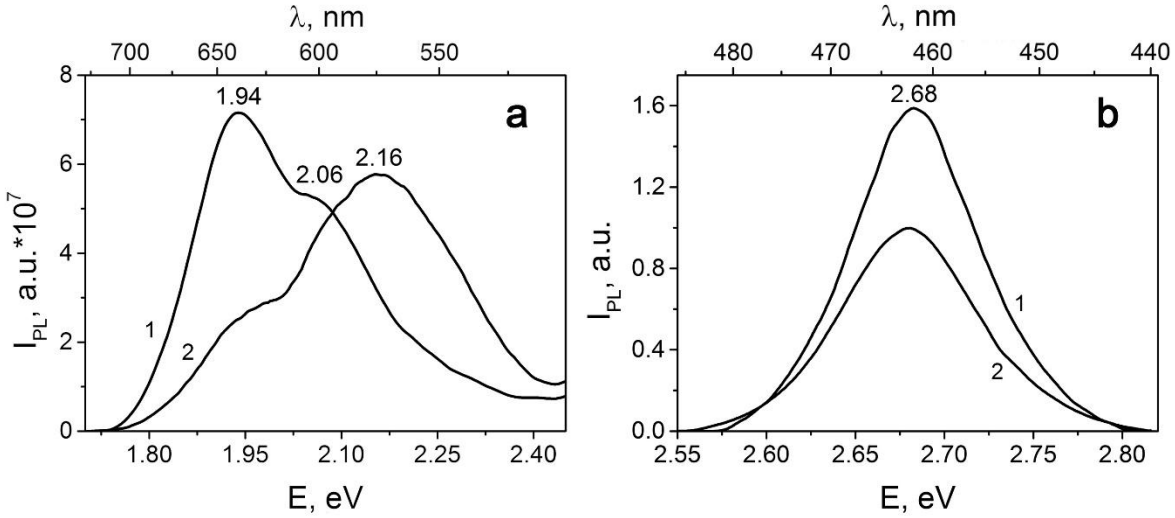

Fig. 1. (a) Long-wavelength and (b) edge PL spectra of (*1*) the undoped and (*2*) Sb-doped ZnSe samples. λ_{exc} = 337 nm ($h\nu_{excit}$ = 3.68 eV). T = 300 K.

As temperature decreases to 90 K, the edge PL band is shifted towards high energies (2.77 eV, 447 nm) and narrows to 55 meV for both the undoped and Sb-doped samples (Fig. 2). According to [6], the $^4T_1$–$^6A_1$ and $^4T_2$–$^6A_1$ intracenter transitions within the Mn^{2+} ion are considered to be the main contribution to the formation of the long-wavelength PL band for the undoped sample at both 300 K (Fig. 1) and 90 K (Fig. 2). A short-wavelength wing of the band is probably caused by [I_{Se}–($V_{Zn}I_{Se}$)] transitions or a Cu impurity [7].

The introduction of Sb impurity into the ZnSe samples changes the shape of the long-wavelength PL band, and the dominant maximum is now localized at 2.16 eV (575 nm) at 300 K (Fig. 1). Similarly to the undoped ZnSe sample, V_{Zn} and I_{Se} defects, as well as Cu and Mn ions, contribute to this PL band. However, the change in the shape of this PL band and the appearance of an additional maximum give reasons to suppose that a new recombination channel, "Sb-yellow radiation", makes a major contribution to the band. It would appear reasonable that this radiation should be attributed to the Sb-based luminescence center in ZnSe. We suppose that the ($Sb_{Se}I_{Se}$) associative center, which forms the acceptor level located at ~0.52 eV above the valence band edge, can be this Sb-based luminescence center. The process of formation of this new PL band can be illustrated by two modes of excitation of the luminescence center: indirect (Fig. 3a) and direct excitation (Fig. 3b) depending on excitation energy.

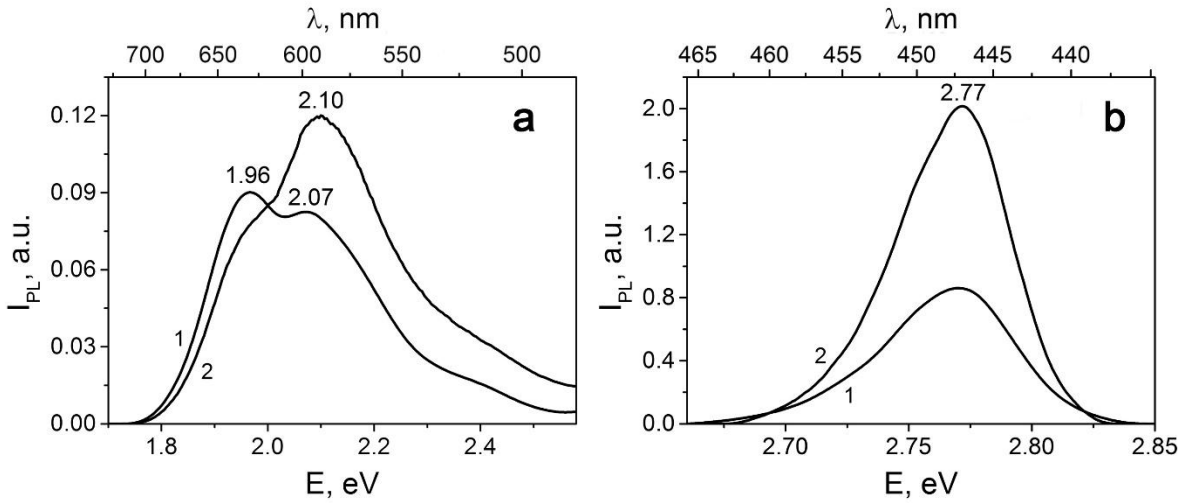

Fig. 2. (a) Long-wavelength and (b) edge PL spectra of (*1*) the undoped and (*2*) Sb-doped ZnSe samples. λ_{exc} = 337 nm ($h\nu_{excit}$ = 3.68 eV). T = 90 K.

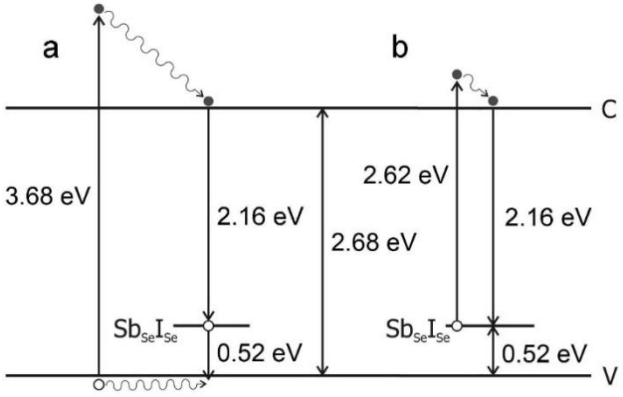

Fig. 3. Electron transitions under (a) indirect and (b) direct excitation of the ($Sb_{Se}I_{Se}$) luminescence center in the ZnSe:Sb single crystal.
λ_{exc}: (a) 337 nm ($h\nu_{excit}$ = 3.68 eV) and (b) 473 nm ($h\nu_{excit}$ = 2.62 eV). E_g(300 K) = 2.68 eV.

Under indirect excitation (Fig. 3a), after generation of nonequilibrium electron–hole pairs, the Sb-based acceptor center captures a valence hole. After that, a recombination of a nonequilibrium electron thermalized in the conduction band with this valence hole takes place. As a result, a respective photon is radiated. Under direct excitation of the luminescence center (Fig. 3b) with a photon energy below the band gap energy, a transition of the electron from the ($Sb_{Se}I_{Se}$) acceptor center deeply to the conduction band occurs. In this case, a recombination of the electron thermalized in the conduction band with a nonequilibrium hole localized at the ($Sb_{Se}I_{Se}$) associative center takes place. As a result, a respective photon is radiated.

For direct excitation of the ($Sb_{Se}I_{Se}$) luminescence center according to the scheme shown in Fig. 3b, the ZnSe:Sb samples were excited with laser radiation of 473 nm, which corresponded to an excitation energy of $h\nu_{excit}$ = 2.62 eV, the value below the ZnSe band gap energy of 2.68 eV at room temperature. The PL spectra of the ZnSe and ZnSe:Sb samples at 300 and 90 K are shown in Fig. 4. It is evident that the yellow PL band is localized at the same wavelengths as those for indirect excitation of the luminescence center (Figs. 1, 2).

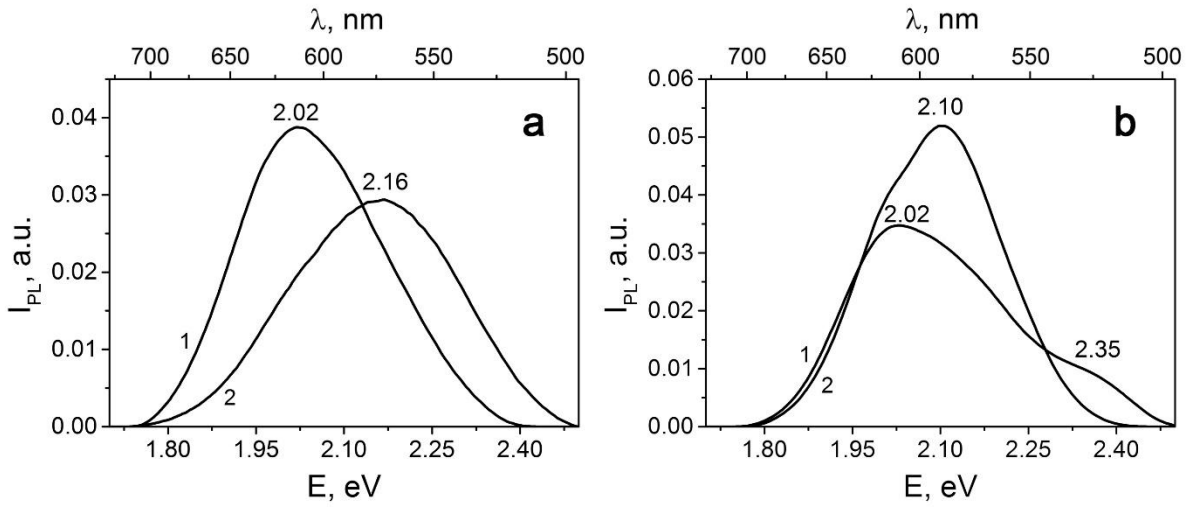

Fig. 4. Long-wavelength PL spectra of (*1*) the undoped and (*2*) Sb-doped ZnSe samples. λ_{exc} = 473 nm ($h\nu_{excit}$ = 2.62 eV). *T* = (a) 300 and (b) 90 K.

The temperature evolution of the PL spectra of the ZnSe:Sb samples under indirect excitation is shown in Fig. 5. As the temperature decreases, the PL band increases in intensity and is shifted to 2.10 eV (590 nm). Since the band has a complex structure and consists of a series of elementary PL bands, this behavior can be attributed to the fact that, with decreasing temperature, the intensity of the long-wavelength components increases faster than that of the short-wavelengths components. As a result, the yellow PL band is shifted towards long wavelengths.

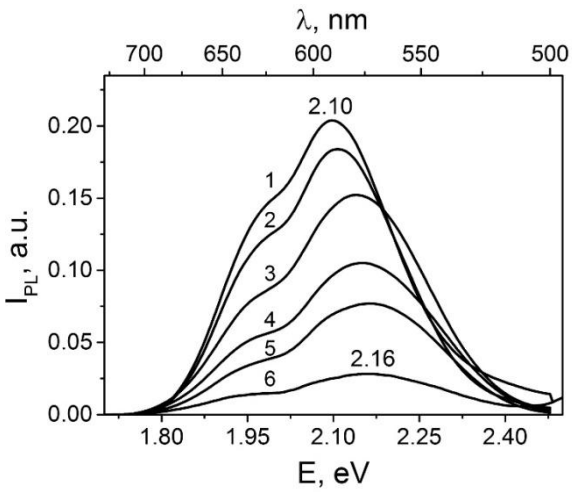

Fig. 5. Temperature evolution of the long-wavelength PL spectrum of the ZnSe:Sb sample. T = (*1*) 90, (*2*) 130, (*3*) 180, (*4*) 220, (*5*) 250, and (*6*) 300 K. λ_{exc} = 337 nm ($h\nu_{excit}$ = 3.68 eV).

4. Conclusions

A new PL band with a maximum localized at 2.16 eV (575 nm) at room temperature has been first found in the PL spectra of the ZnSe single crystals doped with Sb impurity during the growth by the CVT method with iodine as a transport agent. It has been assumed that this PL band is attributed to a ($Sb_{Se}I_{Se}$) associative center with the energy level located at ~0.52 eV above the valence band edge in the ZnSe:Sb samples. A mechanism of the formation of this PL band under direct and indirect excitation of the luminescence center has been proposed to interpret the band behavior with temperature variation.

Acknowledgments

This work was supported by the Supreme Council for Science and Technological Development of the Republic of Moldova (project no. 15.817.02.27F).

References

[1] K.D. Sushkevich, A.V. Simashkevich, A.V. Koval, and O.S. Coschug, Proc. 16th Annual Semicond. Conf. CAS'93, Romania, Sinaia, 1993, p. 513.
[2] J.F. Wang, C.B. Oh, and M. Isshiki, J. Crystal Growth 297, 95 (2006).
[3] M. Takemura, H. Goto, and T. Ido, Jap. J. Appl. Phys. 36, L540 (1997).
[4] Yu.F. Vaksman, N.N. Korneva, and V.V. Serdyuk, J. Appl. Spectroscopy 34, 526 (1981).
[5] V.I. Gavrilenko, A.M. Grekhov, D.V. Korbutyak, and V.G. Litovchenko, Opticheskie svoistva poluprovodnikov: spravochnik, Naukova Dumka, Kiev, 1987.
[6] V. Sirkeli, D. Nedeoglo, N. Nedeoglo, I. Radevich, R. Sobolevskaya, K. Sushkevich, E. Lähderanta, A. Lashkul, R. Laiho, J.-P. Biethan, O. Yilmazoglu, D. Pavlidis, and H. Hartnagel, Phys. B, 407, 3802 (2012).
[7] Physics and Chemistry of II–VI Compounds, edited by M. Aven and J.S. Prener, North-Holland, Amsterdam, 1967.

SHUBNIKOV–DE HAAS OSCILLATIONS IN $Pb_{0.82}Sn_{0.18}Te$ SINGLE CRYSTALS

D. Meglei and S. Alekseeva*

Ghitu Institute of Electronic Engineering and Nanotechnology, Academiei str. 3/3, Chisinau, MD-2028 Republic of Moldova
**E-mail: alexeeva@nano.asm.md*
alexeeva_240747@mail.ru

(Received September 3, 2019)

Abstract

Lead–tin telluride single crystals have been prepared by gas-phase synthesis. Shubnikov–de Haas effects in magnetic fields up to 12 T at low temperatures of 2.1 and 4.2 K have been studied. Parameters of the charge carrier energy spectrum have been determined. It has been found that an increase in the charge carrier concentration leads to an increase in the cyclotron effective mass, Fermi surface cross section, and relaxation time.

1. Introduction

Intense interest in studying the properties of narrow-gap semiconductors, particularly, lead–tin telluride single crystals is attributed to the wide possibilities of practical use of these materials as detectors and sources of radiation in the infrared spectral region, thermoelectric cells, strain gauges, etc. The scientific interest in these materials is primarily associated with their unusual galvanomagnetic, thermomagnetic, and magnetooptic properties [1].

The Shubnikov–de Haas (SdH) effect is a universal and powerful tool for studying the energy spectrum of degenerate electronic systems in metals, semimetals, alloys, and doped semiconductors. It was found that particularly suitable objects for the observation of this effect are $A^{III}B^{V}$ and $A^{II}B^{IV}$ group semiconductors and narrow-gap semiconductors.

The high content of information on the electronic system parameters is responsible for the widespread use of the SdH effect [2].

To obtain reliable experimental results, severe requirements are imposed on the quality of the samples under study: the volume distribution of the components should be uniform, while the amount of mechanical defects should be minimal. The most effective method for synthesizing homogeneous $Pb_{1-x}Sn_xTe$ single crystals is the gas-phase growth technique. To provide the growth of single crystals from the gas phase, we have developed a special technology using high-purity Pb, Sn, and Te of the OSCh-0000 grade as starting materials (Te was purified by multiple zone recrystallization). Microstructural and spectral studies and the Hall coefficient measurements confirmed the high quality of the synthesized $Pb_{1-x}Sn_xTe$ ($x = 0.18$) single crystals.

2. Results and Discussion

Determination of crystal parameters from experimental data on the SdH effect

In a quantizing magnetic field, taking into account the spin splitting of the levels for the Kane's dispersion law, the charge carrier spectrum (at $H \parallel z$) has the form [3]

$$\varepsilon(1+\frac{\varepsilon}{E_g}) = (n+\frac{1}{2}) * \eta\omega_c + \frac{P_z}{2m_c} + g\beta H / 2 \quad (1)$$

where n = 0,1,2... is the Landau level number, E_g is the band gap, $\beta = \frac{e\eta}{2m_0}$, P_z is the projection of the quasi-momentum vector onto the direction of magnetic field H, and ε is the charge carrier energy. This dispersion law is valid in the case of $m_c >> m_0$, which holds true in the case under consideration.

In experimental terms, the study of magnetoresistance oscillations provides the determination of a number of parameters of the energy spectrum of charge carriers. Quantum levels were determined from the ratio

$$n = k\frac{H_{n+k}}{H_n - H_{n+k}}, \quad (2)$$

where H_i is the magnetic field magnitude at the i maximum of magnetoresistance. Oscillation period was calculated by the following formula:

$$\frac{1}{H_{n+1}} - \frac{1}{H_n} = \Delta[\frac{1}{H}].$$

The experimental $n(1/H)$ dependence was used to calculate the slope and determine the SdH oscillation frequency.

$$F = \frac{\Delta n}{\Delta\frac{1}{H}}.$$

In the Kane's approximation, the frequency of magnetoresistance oscillations is as follows:

$$F_i = F\frac{1+2\frac{\varepsilon_F}{E_g}}{1+\frac{\varepsilon_F}{E_g}}, \quad (3)$$

where F is the oscillation frequency in the case of the parabolic dispersion law. Oscillation period is determined by the area of the extreme sections of the Fermi surface:

$$S_{экст.} = \frac{2\pi e}{\eta}\frac{1}{\Delta[\frac{1}{H}]} = \frac{2\pi e}{\eta}F \quad (4)$$

Cyclotron masses were determined from the temperature dependence of the SdH oscillation amplitudes, in accordance with the formula

$$m_c = \frac{e\eta H}{2\pi^2 kTc} * Arch\left[\frac{B(T_1, H_n)}{B(T_2, H_n)}\right], \quad (5)$$

$B(T,H)$ is the oscillation amplitude where at temperature T and in field H. ($T_2 = 2T_1$) Fermi energy can be calculated from the following relationship: $\varepsilon_F = (n+\frac{1}{2})\frac{e\eta H_n}{m_c}$. For the case of an

anisotropic Fermi surface, the charge carrier concentration can be calculated by the following formula:

$$\frac{p}{M} = \frac{1}{3\pi^2}\left(\frac{2e}{\eta}\frac{1}{\Delta[\frac{1}{H}]}\right)^{3/2}\frac{\left[k\cos^2\Theta + \sin^2\Theta\right]^{3/4}}{k^{1/4}}, \quad (6)$$

where M is the number of equivalent extrema in the Brillouin zone, p is the charge carrier concentration, $k = \frac{m_{\|}}{m_{\perp}}$, and Θ is the angle between the major axis of the ellipsoid and the direction of the magnetic field.

Dingle showed that the broadening of the Landau levels due to electron scattering is equivalent to an increase in temperature by the value of $T_D = \frac{\eta}{\pi k_0 \tau}$, where τ is the relaxation time.

The Dingle temperature, which characterizes the smearing of the Landau levels and determines the amplitude of quantum oscillations, can be calculated by the formula

$$T_D = \frac{e\eta}{2\pi^2 k_0 m_c} tg\alpha, \quad (7)$$

where α is the slope of the dependence of the SdH oscillation amplitude on the reciprocal magnetic field.

With an increase in the magnetic field, additional maxima associated with the spin splitting of the Landau levels appear on the oscillating resistance curve; therefore, the g-factor can be calculated:

$$g = \frac{\frac{1}{H_k} - \frac{1}{H_{k+1}}}{\frac{1}{H_k^s} - \frac{1}{H_{k+1}^s}} = \frac{\Delta[\frac{1}{H}]}{\Delta[\frac{1}{H^s}]} \quad . \quad (8)$$

Figure 1 shows the field dependence of the transverse magnetoresistance of $Pb_{0.82}Sn_{0.18}Te$ in magnetic fields up to 12 T at a temperature of 2.1 K.

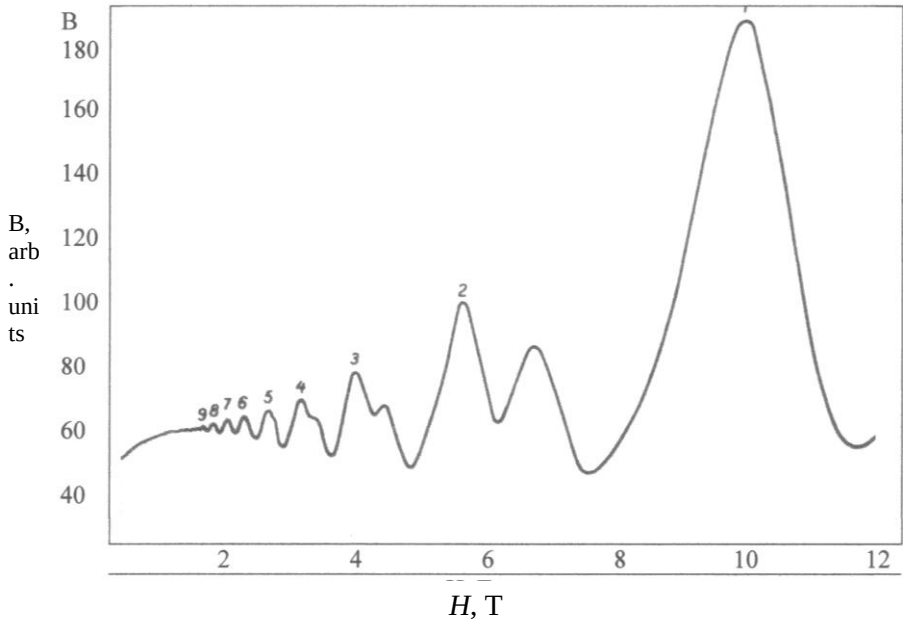

Fig. 1. Field dependence of the transverse magnetoresistance of $Pb_{0.82}Sn_{0.18}Te$ (sample 2)

The observed SdH oscillations are periodic in a reciprocal magnetic field 1/*H* (Fig. 2).

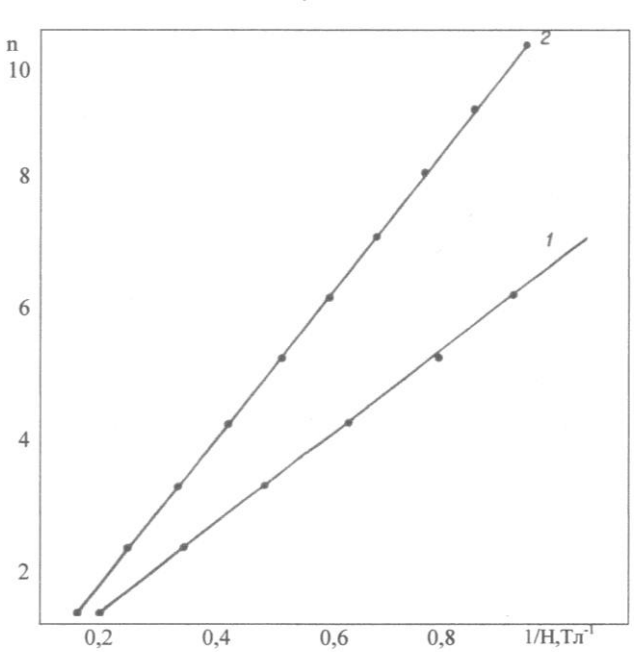

Fig. 2. Dependence of the quantum number of the SdH oscillations on reciprocal magnetic field 1/*H*.

Table 1. Parameters calculated from the field dependence of the transverse magnetoresistance of two $Pb_{0.82}Sn_{0.18}Te$ samples in magnetic fields up to 12 T at two temperatures of 4.2 and 2.1 K

Sample	p, 10^{17} cm^{-3}	$\frac{m_c}{m_0}$	S, 10^{-13} cm^{-2}	T_D, K		g		ε_F, eV	τ, 10^{-12} s		F, 10^5 G
				4.2 K	2.1 K	4.2 K	2.1 K		4.2 K	2.1 K	
1	9.6	0.07	1.12	6.4	6.0		9.1	0.057	0.38	0.405	0.304
2	4.8	0.031	0.29	11.4	10.1	5.5	12.2	0.03	0.21	0.24	1.17

3. Conclusions

Based on the effect of Shubnikov de Haas were calculated the electronic system parameters of two $Pb_{0.82}Sn_{0.18}Te$ samples in magnetic fields up to 12 T at two temperatures of 4.2 and 2.1 K.

The derived data show that an increase in the charge carrier concentration leads to an increase in the cyclotron effective mass magnitude, the Fermi surface cross section, and the relaxation time.

References

[1] B.A. Volkov, L.I. Ryabova, and D.R. Khokhlov, Usp. Fiz. Nauk 172 (8), 874 (2002).
[2] N.B. Brandt and S.M. Chudinov, Usp. Fiz. Nauk 137, 479 (1982).
[3] R. Kybo, H. Haseyawa, and N. Hashitsume, J. Phys. Soc. Jpn. 14, 56 (1969).

MAGNETOTHERMOELECTRIC PROPERTIES OF SINGLE-CRYSTAL WIRES AND FILMS BASED ON Bi–3at%Sb

A. A. Nikolaeva, L. A. Konopko, I. A. Popov, K. Slobodenyuk, G. M. Rastegaev, and E. Istrate

Ghitu Institute of Electronic Engineering and Nanotechnology, str. Academiei 3/3, Chisinau, MD-2028 Republic of Moldova
E-mail: A.Nikolaeva@nano.asm.md

(Received November 8, 2019)

Abstract

Results of a study of the magnetothermoelectric properties and the Shubnikov–de Haas effect in single-crystal wires of various diameters and films based on $Bi_{1-x}Sb_x$ semimetal alloys have been described. According to the Shubnikov–de Haas oscillations, it has been calculated that the overlap of the *L* and *T* bands in the Bi–3at%Sb semimetal wires decreases more than twofold owing to an increase in the antimony concentration. Thermoelectric gap ΔE, the dependence of the gap on wire diameter *d*, and the temperature dependence of power factor $\alpha^2\sigma(T)$ as a function of diameter and magnetic field have been calculated. It has been found that a decrease in wire diameter *d* leads to a semimetal–semiconductor transition at $d < 1.2$ μm, which is more than an order of magnitude higher than in pure Bi wires and 1.5 times higher than in wires of Bi–2at%Sb alloys. It has been shown that thermal gap ΔE increases with decreasing wire diameter *d* in accordance with a law close to $1/d$, which is consistent with theoretical calculations based on the occurrence of the quantum size effect in semimetals. A switching effect in the magnetothermopower has been found; the dependence of this effect on wire diameter *d* and temperature has been determined. It has been shown that, in a weak magnetic field, the magnetothermopower anisotropy in Bi–3at%Sb wires and films increases with decreasing temperature; this feature can be used in anisotropic thermoelectric energy converters.

1. Introduction

Bismuth and antimony form a continuous series of substitutional solid solutions; that is, during the alloying with bismuth, a Sb atom occupies the place of a Bi atom in the crystallographic structure. In this case, the symmetry of the unit cell is preserved, and the unit cell parameters vary only slightly; therefore, the addition of antimony provides a gradual rearrangement of the band spectrum of bismuth.

In $Bi_{1-x}Sb_x$ alloys, a smooth transition from the semimetallic state to the gapless state and then to the semiconductor state is observed at $x > 6$ at % Sb [1, 2].

In a concentration range of $0 < x < 4$ at % Sb, $Bi_{1-x}Sb_x$ alloys are semimetals in which the band overlap decreases with increasing antimony concentration; the process is accompanied by a decrease in the electron and hole Fermi surfaces.

The undying interest in $Bi_{1-x}Sb_x$ alloys is attributed to the fact that this alloy is, on the one hand, a promising low-temperature ($T < 200$ K) thermo- and magnetothermoelectric material [3, 4] and, on the other hand, a model material in solid state physics owing to the high sensitivity

of this alloy to composition, sizes, and the effect of external factors, such as temperature, deformation, and magnetic field [5, 6].

In recent years, interest in low-dimensional structures based on $Bi_{1-x}Sb_x$ has abruptly increased owing to the prediction of Prof. M. Dresselhaus that thermoelectric figure of merit

$$ZT = \frac{\alpha^2 \sigma}{\chi_e + \chi_L} T$$

(σ is the electric efficiency, α is the thermoelectric power, χ_e and χ_L are the points of lattice and electronic heat conductivity) in $Bi_{1-x}Sb_x$ semimetal alloys increases owing to the occurrence and implementation of a quantum size effect (QSE) [7–10]. Typically, the QSE is implemented at low temperatures.

Single-crystal samples are required for the occurrence of the QSE. A decrease in the overlap of the *L* and *T* bands in $Bi_{1-x}Sb_x$ semimetal alloys ($x < 5$ at %) can lead to an increase in the temperature or the thickness at which the QSE is implemented.

The aim of this study was to develop a technology for the preparation of single-crystal films and glass-insulated wires based on Bi–3.5at%Sb and Bi–3at%Sb semimetal alloys and determine their anisotropy and magnetothermoelectric properties as a function of diameter, temperature, and magnetic field in a temperature range of 80–300 K.

2. Experimental

Samples of $Bi_{1-x}Sb_x$ film single crystals were grown by zone melting under a protective layer [11, 12]. A finely dispersed film of the respective composition was deposited on mica by thermal evaporation in a vacuum.

After that, in a vacuum, the material of the coating (KBr) was deposited onto the resulting polycrystalline film of a bismuth–antimony solid solution to eliminate the contraction of the molten film into droplets during the subsequent zone recrystallization. The melting point of the material of the coating should be higher than the melting point of the original film.

The zone recrystallization of the film was implemented on a special setup at a zone passage velocity of 1 mm/h. The zone recrystallization process was run in an argon atmosphere.

After zone recrystallization, the sample was placed in a solvent. In the case of using KBr as the protective coating, distilled water was used to remove it.

Using the proposed method, single-crystal films of a bismuth–antimony solid solution with a uniform distribution of components throughout the volume on a mica substrate were prepared. The uniform distribution of components throughout the volume and the monocrystallinity of the structure were confirmed by experimental studies of the prepared thin films by X-ray diffraction analysis according to the width of the 5th order peak.

Thus, homogeneous single-crystal films of Bi–3.5at%Sb alloys with a thickness of 0.2–3 μm and the orientation of C_3 perpendicular to the film plane on a mica substrate were prepared.

Single-crystal Bi–3at%Sb wires of various diameters were prepared by liquid-phase casting by the Ulitovsky method [13–15]. Diameters were controlled under a BIOLAM-12 optical microscope and by test measurements on a scanning electron microscope. The monocrystallinity of the samples was determined by X-ray diffraction studies and confirmed by

transverse magnetoresistance rotation diagrams (TMRDs) and Shubnikov–de Haas (SdH) oscillations. The studied Bi–3at%Sb wires, as pure Bi wires (prepared by liquid-phase casting), have almost the same crystallographic orientation in the entire thickness range: the wire axis lies in the bisector–trigonal plane and forms an angle of ≈20° with the C_1 bisector axis (orientation 1011).

The resistance and magnetoresistance of the films were measured by the four-probe method (Fig. 1a); the thermopower was determined by the two-probe method. Studies of the wires were conducted by the two-probe method using an InGa eutectics to form ohmic contacts [14, 15].

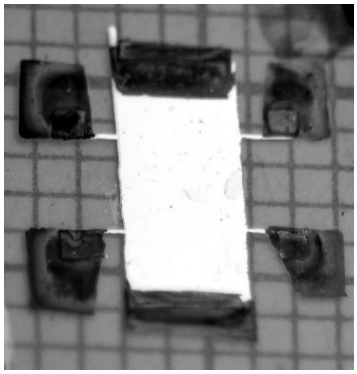

Fig. 1. Sample of the Bi–3.5at%Sb film single crystal on mica with four sprayed silver contacts.

Shubnikov–de Haas oscillations were measured at the International Laboratory of Strong Magnetic Fields and Low Temperatures (Wroclaw, Poland) in a superconducting solenoid at a temperature of 4.2 K in magnetic fields of up to 14 T.

3. Results and Discussion

3.1. Shubnikov–de Haas effect

Using Bi–3at%Sb wires (d = 1 μm), the SdH effect on longitudinal magnetoresistance $R(H)$ ($H \parallel I$) was studied. Figure 2 shows the dependences of reduced longitudinal magnetoresistance $\Delta R/R(H)$ ($H \parallel I$) of the Bi–3at%Sb wire and the pure Bi wire with d = 1 μm at 4.2 K. As in pure Bi wires, a maximum is formed in the initial portion of the $R(H)$ curves; the position of the maximum and the $\Delta R/R$ value significantly depend on wire diameter d [13, 16]. In the Bi–3at%Sb wires, the increase in $\Delta R/R$ at the maximum and the position of H_{max} at 4.2 K are 4 times higher than the respective parameters in the pure Bi wires of the same diameter.

The initial increase in resistance in a weak magnetic field $R(H)$ is attributed to both the anisotropy of the material and the occurrence of a galvanomagnetic size effect (GMSE). In a weak magnetic field, the curvature of the electron trajectory by the magnetic field leads to a decrease in the charge carrier mobility owing to an increase in the contribution of surface scattering.

Since the anisotropy of the Bi–3at%Sb wires is higher than that of pure bismuth and the charge carrier mobility increases while approaching a gapless state, an increase in $\Delta R/R$ at the maximum point and a shift of H_{max} to the region of stronger magnetic fields in the Bi–3at%Sb alloy wires compared with the pure Bi wires of the same diameter are obvious.

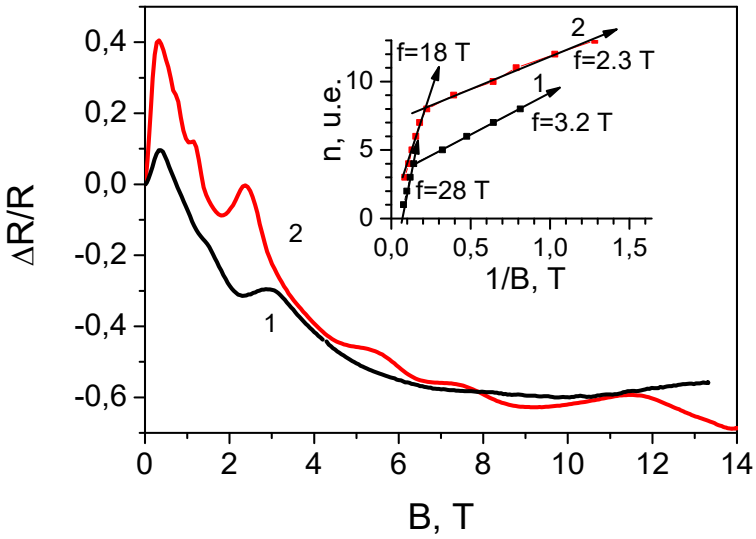

Fig. 2. Shubnikov–de Haas effect on longitudinal magnetoresistance $\Delta R/R(H)$ ($H \parallel I$) at 4.2 K: (curve *1*) the Bi–3at%Sb wire with d = 1 μm and (curve *2*) the pure Bi wire with d = 1 μm.

In the region where Larmor radius r_L is equal to wire diameter d ($r = d$), the role of the surface is excluded, and the resistance decreases tending to saturation in the region of strong magnetic fields ($\mu H >> 1$) for both the pure Bi and Bi–3at%Sb wires (Fig. 2).

The frequency of ShdH oscillations in a strong magnetic field from a *T*-hole ellipsoid $\Delta(1/H)$ decreases 1.5-fold compared with that for pure bismuth; this fact indicates a significant decrease in the cross section of the Fermi surface of *T*-holes and, together with a decrease in the volume of electron ellipsoids, proves a more than twofold decrease in the overlap of the *L* and *T* bands in the Bi–3at%Sb alloy wires, as in bulk samples of the respective composition.

3.2 Magnetothermoelectric properties

Figure 3a shows temperature dependences of relative resistance $\Delta R/R(T)$ of the Bi–3at%Sb wires with different diameters (curves *1–5*) and the Bi–3at%Sb single-crystal film with t = 1 μm (curve *6*).

It is evident from Fig. 3a that the $R(T)$ dependence exhibits a metallic behavior only in the wires with d > 1.2 μm.

The $R(T)$ dependences for the wires with d < 1.2 μm and films with t < 1.2 μm can be approximated by the expression

$$\rho = \rho_0 * exp\left(\frac{\Delta E}{2\kappa T}\right). \quad (1)$$

The $\rho(10^3/T)$ dependences were used to determine thermal gap ΔE formed owing to the occurrence of the QSE and the dependence of the gap on wire diameter d. It was found that the gap increases from ΔE = 6 meV for the wires with d = 1.2 μm to ΔE = 24 meV for the wires with d = 0.3 μm. For the Bi–3.5at%Sb single-crystal films with t = 1 μm, the gap was 4.5 meV.

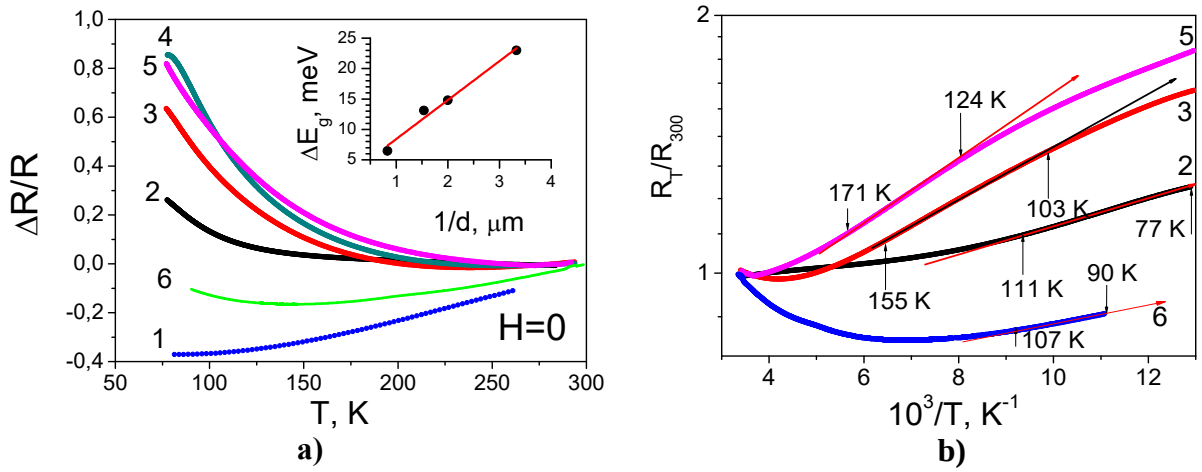

Fig. 3. (a) Temperature dependences of reduced resistance $\Delta R/R(T)$ of $Bi_{0.97}Sb_{0.03}$ thin wires and (b) R_T/R_{300} dependences on the reciprocal of temperature $10^3/T$: d = (*1*) 3.3, (*2*) 1.2, (*3*) 0.6, (*4*) 0.5, and (*5*) 0.3 μm; (*6*) the $Bi_{0.965}Sb_{0.035}$ film single crystal with t = 1 μm..

Note that the maximum gap value of ΔE = 15 and 20 meV in the pure Bi wires is achieved for diameters of 75 and 50 nm, respectively [14, 17]; in the Bi–3at%Sb wires, ΔE = 6 and 24 meV takes place for d = 300 nm; this fact suggests that the addition of antimony to bismuth leads to a decrease in the overlap of the L and T bands E_o; therefore, the QSE can be observed for thicknesses of ≈1 μm. Figure 3a (inset) shows the dependence of the thermal gap on the reciprocal of wire diameter $\Delta E(1/d)$. It is evident from the figure that the dependence is close to linear; this finding is consistent with the theoretical predictions of [7, 16] and indicates the formation of a gap of L carriers in the Bi–3at%Sb semimetal wires during the implementation of the QSE.

The magnetothermoelectric properties of the wires and single-crystal films were studied in a temperature range of 300–77 K in a magnetic field of 0.4 T ($H \perp I$).

To provide the orientation of the magnetic field ($H \perp I$, $\perp \Delta T$) in respective crystallographic directions, TMRDs $\Delta R/R(\theta)$ and thermopower $\alpha(\theta)$ were recorded, while rotating the magnetic field in the trigonal–bisector plane.

Figure 4 shows TMRDs $\Delta R/R(\theta)$ of the Bi–3.5at%Sb film with t = 1 μm at temperatures of 300 and 77 K and the Bi–3at%Sb wires with d = 6 and 0.3 μm (Fig. 8b, insert) in a magnetic field of 0.4 T.

It is evident from Fig. 4 that, at 300 K, the TMRDs $\Delta R/R(\theta)$ are symmetric with respect to the rotation axis for both the films and the wires and correspond to analogous dependences of the bulk samples at the orientation of the principal axis of the crystal along the C_1 bisector axis and in the case of magnetic field rotation in the trigonal–bisector plane.

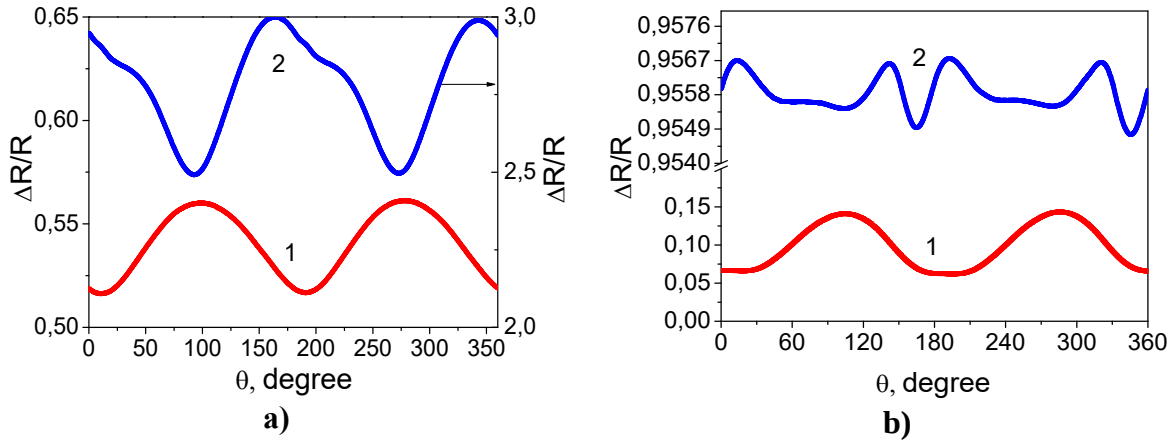

Fig. 4. TMRDs $\Delta R/R(\theta)$ (H_T = 0.4 T, $H \perp \Delta T$) of (a) the $Bi_{0.965}Sb_{0.035}$ film single crystal with t= 1 μm and (b) Bi–3at%Sb wire with d = 6 μm: (*1*) 300 and (*2*) 77 K.

With a decrease in temperature to 77 K, a decrease in anisotropy and a complication of the TMRDs $\Delta R/R(\theta)$ are observed. The slight asymmetry is associated with the deviation of the C_2 axis from the wire axis by 20° (according to X-ray diffraction studies of the single-crystal wires) [13–15].

Figure 5 shows the transverse thermopower rotation diagrams of (a) the $Bi_{0.965}Sb_{0.035}$ film and (b) the Bi–3at%Sb wire at temperatures of 300 and 80 K.

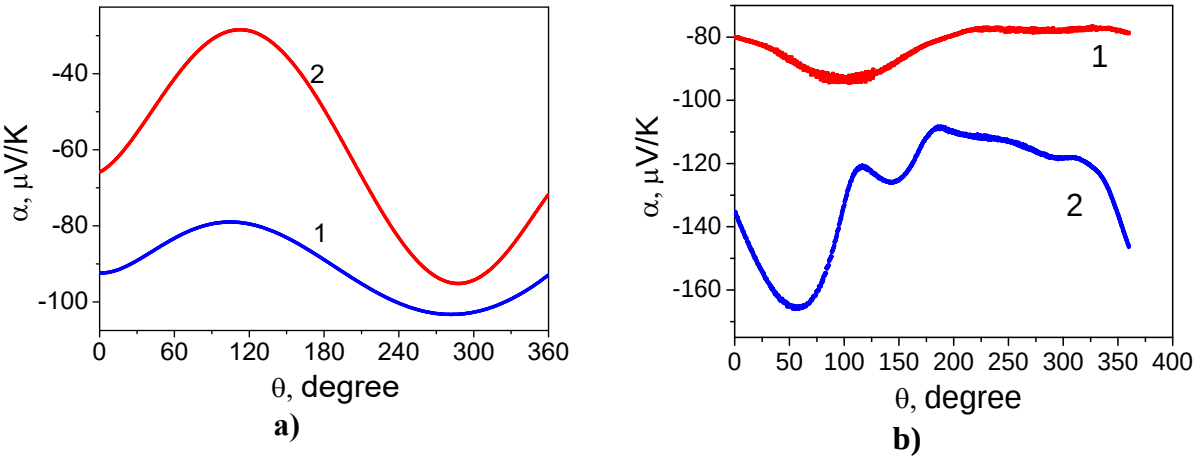

Fig. 5. Transverse magnetothermopower rotation diagrams $\alpha(\theta)$ ($H_\perp$ = 0.4 T) of (a) the $Bi_{0.965}Sb_{0.035}$ film single crystal with t = 1 μm and (b) the Bi–3at%Sb wire with d = 6 μm: (*1*) 300 and (*2*) 77 K.

Noteworthy is the fact that the magnetoresistance anisotropy is extremely low both at 300 and 77 K for wires with the different diameters (d = 6 and 0.3 μm), whereas the thermopower anisotropy significantly increases with a decrease in temperature to 80 K for both the wires with

d = 3.4 μm and the Bi–3.5at%Sb film with t = 1 μm.

Thermomagnetic effects are more sensitive to the features of the band structure, the charge carrier mobility, and the scattering process than galvanomagnetic effects; this factor leads to the occurrence of the switching effect [18–20]. The switching effect, i.e. the manifestation of the dependence of thermoelectric coefficient α(θ) on a change in the magnetic field direction α(–) and α(+) is associated with the presence of electrons and holes with different symmetries of energy extreme localization points and the slope of the isoenergetic surface relative to the crystallographic axes [18].

This effect was particularly pronounced in bulk Bi samples when the temperature gradient did not coincide with the principal axes of the crystal [21]. A decrease in the temperature and an increase in the magnetic field (>1 T) lead to a significant enhancement of the switching effect.

It is known that, in Bi and $Bi_{1-x}Sb_x$ wires, the wire axis is deflected from the bisector axis by approximately 20° in the bisector–trigonal plane and temperature gradient ΔT does not coincide with the C_2 bisector axis. Therefore, the occurrence of the switching effect in the Bi–3at%Sb wires with d = 6 μm and the Bi–3.5at%Sb films with t = 1 μm is obvious.

The occurrence of anisotropy of 60 μV/K at 77 K in the Bi–3at%Sb wires and films can be used in anisotropic thermoelectric converters at low temperatures.

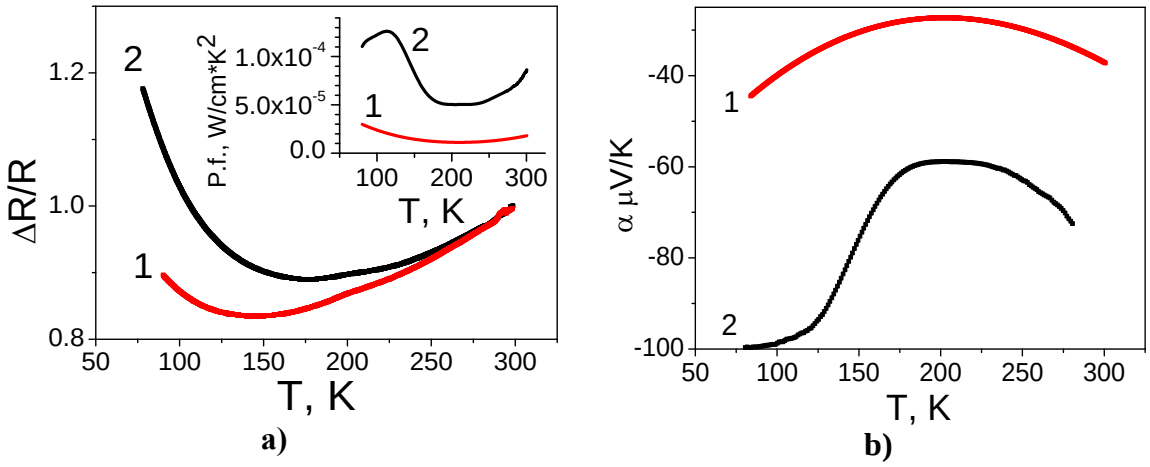

Fig. 6. Temperature dependences of (a) the reduced resistance of the film single crystal and (b) the thermopower of the $Bi_{0.965}Sb_{0.035}$ sample at H = (*1*) 0 and (*2*) 0.4 T ($H \perp I$, $H \parallel C_3$); the sample thickness is t = 1 μm. Inset: calculated values of the power factor as a function of temperature P.f.(T).

Figures 6 and 7 show the temperature dependences of the magnetoresistance $\Delta R/R(T)$ ($H \perp I$) and magnetothermopower $\alpha(T)$ ($H \perp \Delta T$, $H_\perp$ = 0.4 T) of the single-crystal film (Figs. 7, 8) with a thickness of t = 1 μm and the wires with diameters of 3.3 and 0.3 μm (Fig. 7). The magnetic field of 0.4 T ($H \perp \Delta T$) was directed along the C_3 axis (point 0 in the TMRDs) and along the C_2 axis (θ = 90°).

In wires with d > 1 μm and films with t > 1 μm, a magnetic field of 0.4 T ($H \perp \Delta T$) leads to an increase in the absolute value of thermopower with a decrease in temperature to 80 K; in the wires with d = 6 μm, the thermopower increases to –180 μV/K (Fig. 7b, curve *2*).

In thin Bi–3at%Sb wires (d = 0.3 μm), the absolute value of thermopower decreases at 80 K (Fig. 7b, 8b, curve *1*). A significant decrease in the absolute value of thermopower with a decrease in wire diameter d up to the sign reversal from (–) to (+) was observed in thin Bi wires [22] and theoretically substantiated in studies where a theoretical calculation of the thermopower in quantum bismuth wires was conducted taking into account the scattering of electrons and holes by long-wave acoustic vibrations and a rough surface (in the form of a delta-like surface fluctuation).

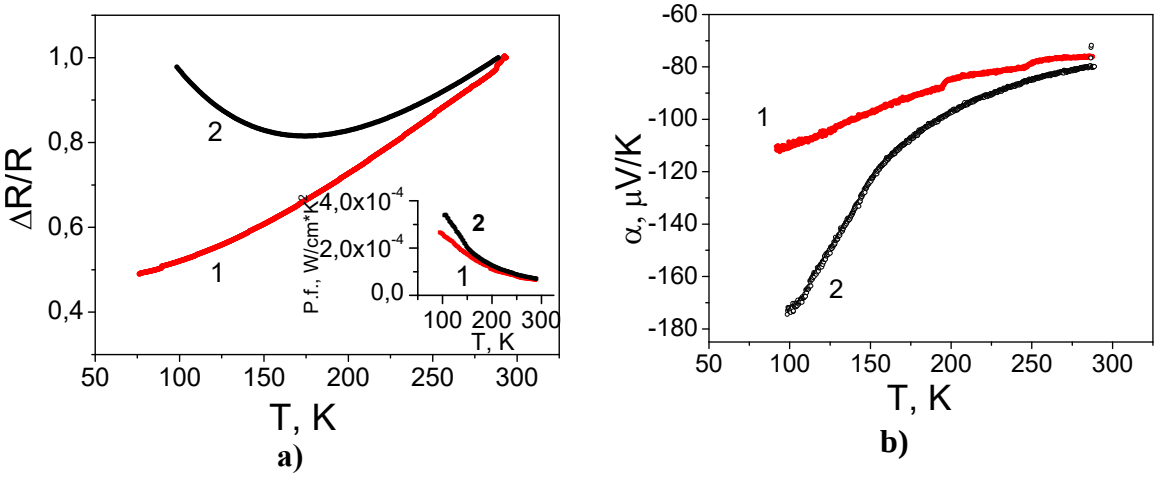

Fig. 7. Temperature dependences of (a) reduced resistance $\Delta R/R(T)$ of Bi–3at%Sb wire with d = 6 μm and (b) thermopower $\alpha(T)$ at H = (*1*) 0 and (*2*) 0.4 T. Inset: calculated values of the power factor as a function of temperature P.f.(T).

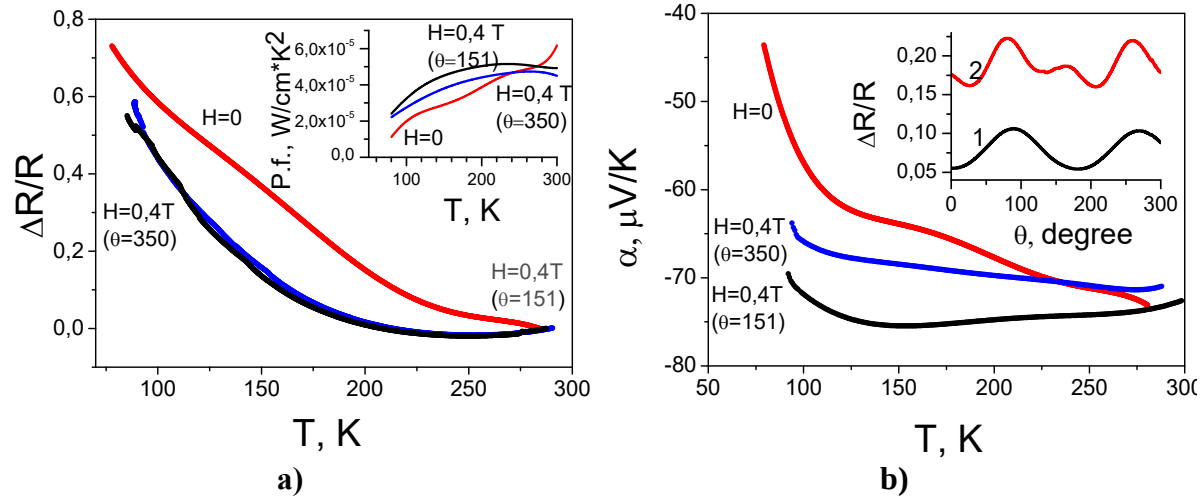

Fig. 8. Temperature dependences of (a) reduced resistance $\Delta R/R(T)$ of Bi–3at%Sb wire with d = 0.3 μm at H = (*1*) 0 and (*2*) 0.4 T and (b) thermopower $\alpha(T)$. Insets: (a) calculated values of the power factor as a function of temperature P.f.(T) and (b) TMRDs at T = (*1*) 300 and (*2*) 80 K.

The authors of [23–25] also indicated the possibility of occurrence of this mechanism. The weakening of the effect in Bi–3at%Sb wires is attributed to a decrease in the Fermi

momentum of electrons. For large wire diameters, it is necessary to take into account a larger number of dimensionally quantized levels, which leads to a weakening of the effect.

According to the experimental results, power factor $\alpha^2\sigma$ was calculated for wires and films at $H = 0$ and $H_\perp = 0.4$ T (Figs. 6a, 7a, 8a (insets)) and the temperature dependence of the power factor $\alpha^2\sigma$ (T) in a temperature range of 77–300 K was recorded.

It was found that power factor $\alpha^2\sigma$ achieves a maximum value of 3.5×10^{-4} W/(cm K^2) at 80 K in a magnetic field of 0.4 T ($H \perp \Delta T$); it is 3 times higher than the value obtained for the single-crystal film. A decrease in wire diameter d leads to a more than an order of magnitude decrease in the power factor in the Bi–3at%Sb alloys; this finding is primarily attributed to the fact that a decrease in wire diameter d (as in the pure Bi wires) leads to the thermopower sign reversal; that is, in the given ranges of temperatures and diameters, this factor leads to a decrease in the absolute value of thermopower, which in turn leads to a decrease in power factor $\alpha^2\sigma$ in thinner wires at low temperatures.

4. Conclusions

A technology for preparing single-crystal wires and films has been developed. Single-crystal wires and films based on Bi–3at%Sb semimetal alloys have been prepared.

The recorded dependences and SdH oscillations have revealed that, in the Bi–3at%Sb wires, the overlap of the L and T bands decreases more than twofold compared with that in pure Bi.

It has been found that, in Bi–3at%Sb wires, the QSE-induced semimetal–semiconductor transition occurs at diameters of $d < 1$ μm, which is more than an order of magnitude higher than in the pure Bi wires and 1.5 times higher than in Bi–2at%Sb.

It has been shown that, with a decrease in wire diameter d, the energy gap increases in accordance with a law close to $1/d$, which is consistent with theoretical calculations taking into account the quantum nature of conductivity.

It has been found that the maximum thermopower anisotropy is achieved at a temperature of ≈100 K; it is 60 μV in the single-crystal films with $t = 1$ μm and the Bi–3at%Sb wires with $d =$ 6 μm, which is an important factor for designing anisotropic thermoelectric energy converters operating in a temperature range of 100–80 K.

References

[1] S. Golin, Phys. Rev. 176, 830 (1968).
[2] A.V. Braune, G. Xuka, H.J. Gollnest, and R. Herrmann, Phys. Stat. Sol. B 89(1), 95 (1978).
[3] B. Lenoir, A. Dauscher, M. Cassart, Y.I. Ravich, and H. Scherrer, J. Phys. Chem. Solids 59(1), 129 (1998).
[4] P. Jandl and U. Birkholz, J. Appl. Phys. 76, 7351 (1994).
[5] T.A. Mironova, M.V. Sudakova, and Ya.G. Ponomarev, Zh. Eksp. Teor. Fiz. 78(5), 1830 (1980).
[6] A.A. Abrikosov and S.D. Beneslavskii, J. Low. Temp. Phys. 5(2), 141 (1971).
[7] Sh. Tang and M.S. Dresselhaus, Phys. Rev. B 89, 045424 (2014).
[8] O. Rabin, Y.-M. Lin, and M. S. Dresselhaus, Appl. Phys. Lett. 79, 81 (2001).
[9] Ph. Hofmann, Progr. Surf. Sci. 81(5), 191 (2006).

[10] D.M. Rowe, Thermoelectric Handbook: Macro to Nano (Taylor & Francis, Boca Raton, 2006).
[11] V.A. Komarov, I.A. Popov, and A.D. Grozav, Izv. Akad. Nauk SSSR, Ser. Fiz. Tekh. 2, 3 (1991).
[12] A.A. Nikolaeva, L.A. Konopko, V. M. Grabov, V.A. Komarov, N. Kablukova, Gh.I. Para, and I.A. Popov. Surf. Eng. Appl. Electrochem. 50(5), 437 (2014).
[13] N.B. Brandt, D.V. Gitsu, A.A. Nikolaeva, and Ya.G. Ponomarev, Zh. Eksp. Teor. Fiz. 72(6), 2332 (1977).
[14] T.E. Huber, D. Gitsu, and L. Konopko, Phys. Rev. B. 77, 035422 (2008).
[15] A.A. Nikolaeva, L.A. Konopko, T.E. Huber, P.P. Bodiul, and I.A. Popov, J. Solid State Chem. 193, 71 (2012).
[16] Y. Lin, X. Sun, and M.S. Dresselhaus, Phys. Rev. B 62, 4610 (2000).
[17] A.A. Nikolaeva, L.A. Konopko, Gh.I. Para, and A.K. Tsurkan, Metallofiz. Noveishie Teknol. 33(1), 65 (2011).
[18] D.V. Gitsu, I.M. Golban, V.G. Kantser, and F.M. Muntyanu, Yavleniya perenosa v vismute i ego splavakh (Shtiintsa, Kishinev, 1983).
[19] D.V. Gitsu, Doctoral (Phys.–Math.) Dissertation, Kishinev, 1972.
[20] P.P. Bodiul, A.S. Fedorko, and D.V. Gitsu. Phys. Stat. Sol. 1(2), k77 (1970).
[21] I.M. Pilat, S.V. Chaika, N.V. Kruglova, and S.I. Pirozhenko, Fiz. Tverd. Tela 17(1), 176 (1975).
[22] E.P. Sinyavskii, L.A. Konopko, A.A. Nikolaeva, V.G. Solovenko, T.E. Huber, J. Thermoel. 3, 52 (2007).
[23] E.P. Sinyavskii and R.A. Khamidullin, Fiz. Tekh. Poluprovodn. 36(8), 989 (2002).
[24] D.A. Pshenai-Severin and Yu. I. Ravich, Fiz. Tekh. Poluprovodn. 36(8), 974 (2002). http://journals.ioffe.ru/
[25] N. Trivedi and N.W. Ashcroft, Phys. Rev B. 38(17), 12298 (1988).

MICROWIRES FOR MEDICAL APPLICATIONS

E. Adar[1], A. Avdeev[2], S. Baranov[2, 6], M. Kilo[3], N. A. Sobolev[4, 5], and A. Yosher[1]

[1]*Wire Machine Technologies Ltd (WMT), Or Akiva, 30600 Israel*
[2]*Institute of Applied Physics, Chisinau, MD 2028* Republic of Moldova
[3]*Fraunhofer Institute for Silicate Research (FH-ISC), Würzburg, 97082 Germany*
[4]*Departamento de Física @ I3N, Universidade de Aveiro, Aveiro, 3810-193 Portugal*
[5]*National University of Science and Technology MISiS, Moscow, 119049 Russia*
[6]*Shevchenko Pridnestrov'e State University, str. 25 Oktyabrya 128, Tiraspol, Republic of Moldova*

**E-mail: baranov@phys.asm.md*

(Received March, 2019)

Abstract

Results of a study for the medical applications of micro- and nanowires are described. The magnetic characteristics of glass-coated Fe-based cast amorphous microwires (with a positive magnetostriction constant) are proposed. The residual stress distributions in this type of microwires determine the domain structures and the switching field behavior. These wires are characterized by a rectangular hysteresis loop and can be used in measuring and identification engineering. A model that describes the process of the reversal magnetization of an amorphous microwire with the help of a large Barkhausen jump is proposed. The model is estimated with regard to the optimization of the signal-to-noise ratio. The results obtained do not contradict the existing physical concepts concerning a domain wall motion and are more general and realistic than the previous models.

1. Introduction

The importance of the medical application is associated with the fact that internal organs requiring radiation therapy are prone to moving within the body over time. Therefore, the location of a tumor determined by X-ray computed tomography scanning or magnetic resonance imaging prior to the onset of the radiation treatment becomes inaccurate once organs readjust their position due to eating, walking, or other bodily motions. As a result, radiation extending periodically over days or weeks can miss the intended target with a collateral damage to the neighboring tissue. Magnetic sensing of the position of a small implanted tag makes it possible to pinpoint the tumor's location just prior to or during treatment.

It is known that a cast amorphous microwire (CAM) with positive magnetostriction exhibits a rectangular hysteresis loop and the magnetization of it is reversed by a large Barkhausen jump (LBJ), the coercive force of which can be regulated by both residual and external mechanical stresses (see, e.g., [1–12]).

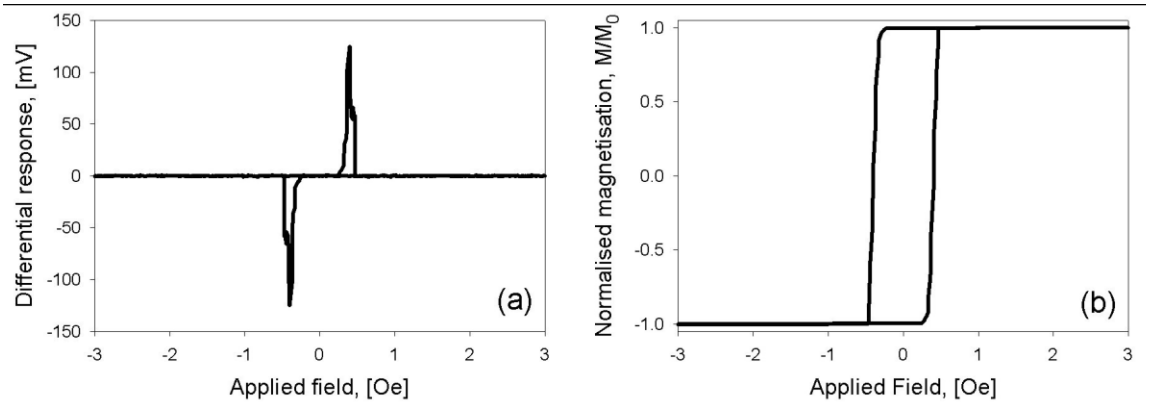

Fig. 1. (a) Differential and (b) integral hysteresis loop by an LBJ.

Various wires (including micro- and nanowires) have feature properties of magnetization reversal with the use of an LBJ; their magnetic structure can differ from the magnetic structure of a CAM. In this case, the possibility of their long-term existence in certain (one of two) magnetized states and a stepwise transition from one magnetized state to another is referred to as the magnetic bistability effect (by analogy with similar effects in other branches of physics). Typically, the bistable ferromagnet (BF) technology consist in the formation of a BF in a material with a strongly pronounced gradient of the magnetic potential profile (e.g., in CAMs) in the presence of quasi-mono-axial magnetic anisotropy. In this case, both bistable states can be abstractedly represented as energy levels of a system spaced by an energy barrier. Bistable ferromagnets were previously obtained by thermal and mechanical treatments. Thus, in particular, the well-known Wiegand Vicalloy wire was prepared [1]. Unlike the Wiegand wire, since the production moment, a CAM with a positive magnetostriction is a BF. In addition to the CAM manufacturing technology, there exists the Unitika technology (Unitika Ltd.). Wires manufactured by the Unitika technology, which is also referred to as in-rotating water quenching, have a magnetic structure and magnetic characteristics that differ from those of CAMs, although they are also attributed to a BF.

2. Theoretical Remarks

Figure 2 shows a magnetic dipole wire and pickup coils.

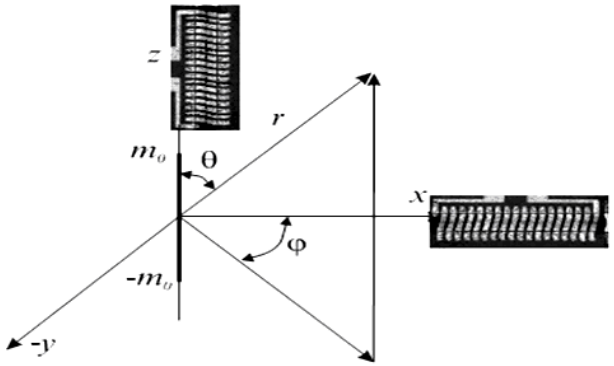

Fig. 2. Experimental arrangement of a dipole wire.

Hertz vector $\overset{\upsilon}{\Pi}_m$ for dipole is represented as follows [4–7]:

$$\overset{\text{r}}{\Pi}_m(t,r) = m_0 \frac{e^{j\omega\left(t-r/c\right)}}{4\pi\mu_0 r}, \tag{1}$$

where $\omega = 2\pi f$ (ω/c = 2π/λ, and λ is the radiation wavelength), f is the frequency , c is the velocity of light, ($\mu_0 = 4\pi \cdot 10^{-7}$ H/m, $i = \sqrt{-1}$), m_0 is the dipole moment ($\overset{\rho}{m}_0 = \overset{\upsilon}{B}_S V$, $\overset{\upsilon}{B}_S$ is the saturation induction of the CAM, V is the dipole volume), and r is the distance from a point of supervision of a field (see Fig. 2).

The function of change of the magnetic moment ($0 \le t \le \infty$) has the form

$$f(t) = Sign(t) - 2e^{-\alpha t} \cdot \theta(t), \tag{2}$$

$$Sign(t) = \begin{cases} 1 & , \ t \ge 0, \\ -1 & , \ -\infty < t < 0, \end{cases}$$

where α is the dipole switching speed.

The transformation of vector function $\overset{\upsilon}{\Pi}_m(t,r)$ is as follows:

$$\overset{\rho}{\Pi}_m(\omega) = \frac{m_0}{4\pi\mu_0 r}\left(\frac{2i}{\omega} - \frac{2}{i\omega+\alpha}\right)e^{-i\omega\frac{r}{c}}. \tag{3}$$

Vector $\overset{\upsilon}{\Pi}_m(\omega)$ is written as follows (in Cartesian coordinates):

$$\overset{\upsilon}{\Pi}_m(\omega) = \left(0, 0, \Pi_z(\omega)\right)$$

The components of function $\overset{\upsilon}{\Pi}_m(\omega)$ are written as follows (see Fig. 2, in spherical coordinates):

$$\left.\begin{aligned} \Pi_r(\omega) &= \Pi_z(\omega)\cos\theta \\ \Pi_\theta(\omega) &= \Pi_z(\omega)\sin\theta \\ \Pi_\varphi &= 0 \end{aligned}\right\}. \tag{4}$$

The magnetic field intensity is obtained as follows:

$$\overset{\upsilon}{H}(\omega) = rotrot\overset{\upsilon}{\Pi}_m(\omega).$$

The components of the magnetic intensity are written as follows:

$$\left.\begin{aligned} H_r &= 2[M_d(\omega)]\left(\frac{2\pi i}{\lambda}\frac{1}{r^2}+\frac{1}{r^3}\right)\cos\theta\, e^{i\frac{\omega r}{c}} \\ H_\theta &= [M_d(\omega)]\left[-\left(\frac{2\pi}{\lambda}\right)^2\frac{1}{r}+\frac{2\pi i}{\lambda}\cdot\frac{1}{r^2}+\frac{1}{r^3}\right]\sin\theta\, e^{i\frac{\omega r}{c}} \\ H_\phi &= 0 \\ [M_d(\omega)] &\approx \frac{[m_0]}{4\pi\mu_0} \end{aligned}\right\}, \tag{5}$$

$[M_d]$ is the absolute value of the magnetic moment, which will be applied in the further estimations.

Let us consider an extreme case, where $r/\lambda < 1$. This case corresponds to low frequencies by which the LBJ is characterized, and the contribution of the member that is proportional to $1/r^3$ is important for them:

$$\left.\begin{aligned} H_r &\sim 2[M_d]\frac{1}{r^3}\cos\theta \\ H_\theta &\sim [M_d]\frac{1}{r^3}\sin\theta \\ H_\phi &= 0 \\ [M_d] &\approx \frac{[m_0]}{4\pi\mu_0} \end{aligned}\right\}, \tag{6}$$

Equations (6) completely correspond to similar formulas for the magnetostatic case [4] and make it possible to theoretically estimate the BJ recording range low frequencies. Note the special features of recording the magnetic pulse data:

(i) The signal of scheme *X* (see Fig. 2), which is twice larger than the signal of scheme *Z*, makes this scheme preferable, and it is used in the experiment (see below). There is no radio signal in this configuration; however, it exists in measurements in accordance with operation scheme *Z*.

(ii) For the CAM dipole with a saturation induction value of $B_S \approx 1$ T (for an Fe-based microwire) and a microwire volume of $V \leq 10^{-11}$ m^3 (for a microwire with a core diameter of ~40 μm and a length of ~10^{-2} m), the equipment for recording the dipole radiation field should be sensitive to magnetic fields of 10^{-7} A/m near the dipole ($r < 1$ m). The small value of this quantity (below the magnetic noise level) is determined by the small value of the dipole volume.

3. Experimental Results

The possibility of recording the LBJ in the near-field zone of the signal by an induction

measuring coil was verified in [11, 12]. The signal of the magnetic flow variation owing to component H_r was recorded. The pickup cool was directed perpendicular to the dipole's center.

The external magnetic field, which initiated the magnetization reversal of the dipole, did not generate an induction EMF in the measuring coil. Therefore, in this scheme, a compensating coil is not required. In this case, the far-field component is absent, and the measuring coil receives the near field of the microwire dipole (with a length of 3 cm and a core diameter of ~50 μm [3]).

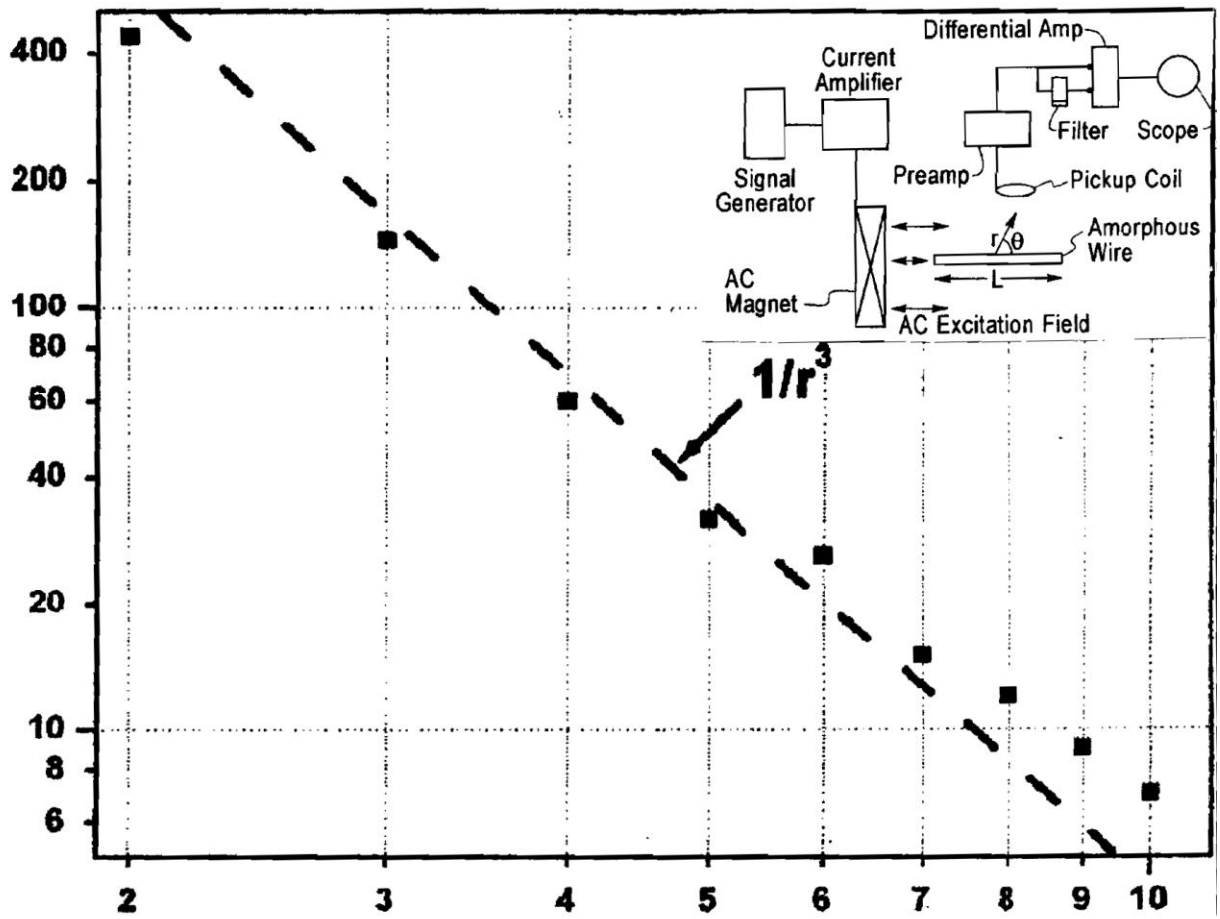

Fig. 3. Dependence of the EMF at the measuring coil plotted in the Y-direction (in mV) on the distance between the center of the dipole and the end wall of the measuring coil in the X-direction (in cm) [12]. Vector *r* (distance from the dipole to the coil) is perpendicular to the center of the dipole and the end wall of the measuring pickup coil. Inset: schematic circuit.

4. Conclusions

The critical length of the CAM sections at which the BF effect with the LBJ is preserved is about 1 mm, being as least ten times smaller than bistable tapes and wires prepared by other methods. The magnetization reversal rate of the CAM is higher than that of the counterparts. It is reasonable to expect that these parameters will be better for nanowires that can be prepared from CAMs by constriction with thinning.

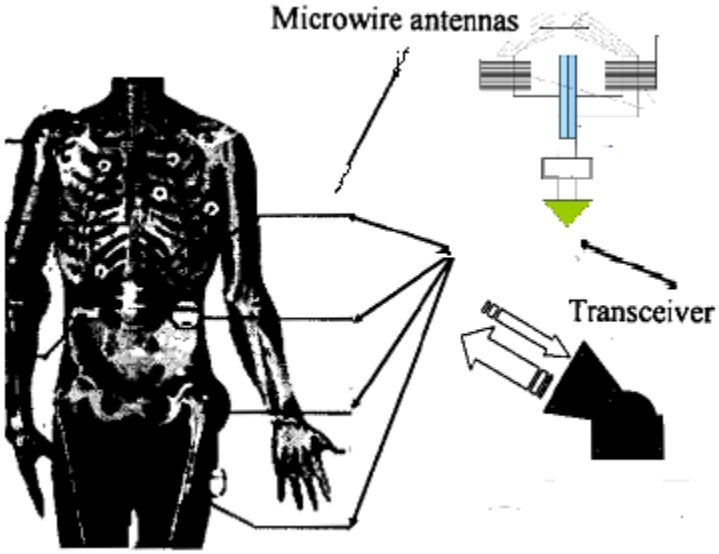

Fig. 4. Schematic possible application of a microwire in medicine.

It is commonly accepted that the widespread practical application of the BF with the LBJ started in 1975 owing to American researcher John Richard Wiegand, who designed the simplest Wiegand transducer based on a Vicalloy wire.

At present, bistable micro- and nanowires can be used for applications in code labels for goods, car parts, valuables, documents, securities, and money; the creation of informational files; for the remote control of actuating mechanisms; and the design of sensitive elements (sensors) in measuring equipment. They also find application in medicine for distinguishing affected organs or observations of transport process of medicinal preparations (with magnetic labels) in organisms. Note that this transport process can be controlled by an external magnetic field.

The obtained experimental and theoretical results testify that labels made of magnetic micro- and nanowires can be used only at small distances from the recording units (at distances of about 0.1–1 m) depending on the micro- and nanowire diameter. In this aspect, they are not competitive for the known radio-frequency identification systems.

In addition to the Barkhausen effect, CAM labels are characterized by a natural ferromagnetic resonance, which can be also used as an additional property for identification.

Acknowledgments

This work was supported by the EU project H2020 – MSCA-RISE – 2017 – 778308 – SPINMULTIFILM and by the FCT of Portugal through the project I3N/FSCOSD (Ref. FCT UID/CTM/50025/2013). N.A.S. acknowledges the support by the Increase Competitiveness Program of NUST «MISiS» (no. K-2018-025). This work was supported by the Moldavian national project (no. 15.817.02.05.A) and Shevchenko Pridnestrov'e State University project (no. 09.3.3-LMT-K-712-08-0003). One of authors (S. Baranov) thanks A.I. Dikusar for his participation in the discussion of the results.

References

[1] G. V. Lomaev, S. P. Akhizina, and T. E. Glushkova, Fiz. Met. Metalloved. 84 (5), 461 (1997).

[2] S. A. Baranov, G. V. Karimova, and G. V. Lomaev, Surf. Eng. Appl. Electrochem. 42 (2), 73 (2006).

[3] W. Döring, Usp. Fiz. Nauk 22 (5), 78 (1939).

[4] S.V. Vonsovskii, Magnetism, Nauka, Moscow, 1971; Wiley & Sons, New York, 1974, 797 p.

[5] S. A. Baranov, Surf. Eng. Appl. Electrochem. 47 (4), 316 (2011).

[6] S. A. Baranov, V. N. Berezhanskii, V. L. Kokoz, S. K. Zotov, V. S. Larin, and A. V. Torkunov, Fiz. Met. Metalloved. 67 (1), 73 (1989).

[7] S. A. Baranov, An Engineering Review about Microwire, Lambert Academic Publishing, 2017, pp. 1–42.

[8] S. A. Baranov, A. V. Torcunov, and V. S. Larin, Crystals 7 (6), 136 (2017).

[9] A. T. Savchuk and S. A. Baranov, Mold. J. Phys. Sci.. 16 (1–2), 70 (2017).

[10] A. T. Savchuk and S. A. Baranov, Mold. J. Phys. Sci. 16 (3–4), 182 (2017).

[11] S. A. Gudoshnikov, N.A Usov, A.P., Zhukov, V. Zhukova, P. S. Palvanov, B.Ya. Ljubimov, O. Serebryakova, and S. Gorbunov, Phys. Stat. Sol. A, 208 (3), 526, (2011).

[12] R.J. Von Gutfeld, J.F. Dicello, S.J. McAllister, and J.F. Ziegler, Appl. Phys. Lett. 81 (10), 1913 (2002).

ELASTOPLASTIC PROPERTIES UNDER NANO-MICROINDENTATION OF PHOSPHATE GLASSES DOPED WITH RARE-EARTH IONS

Z. Barbos

Institute of Applied Physics, str. Academiei 5, Chisinau, MD-2028 Republic of Moldova
E-mail: danitaz@mail.ru

(Received February 8, 2019)

Abstract

The microstructure and mechanical (elastic and plastic) properties of phosphate glasses (PhGs) doped with rare-earth elements (REEs), namely, Pr, Nd, Sm, Eu, Gd, Dy, Ho, Er, and Yb, have been studied in this paper. The strength parameters of the PhGs and their dependence on the load value modification have been estimated by the depth-sensing indentation method. Three specific stages have been revealed in the deformation process, including nano-, submicro, and microdeformation. It has been assumed that the elastic and plastic properties of PhGs can be associated with the specificity of the internal structure of the glasses.

1. Introduction

Intensive research into the various types of glassy materials is being conducted due to their widespread application in many areas of modern engineering. However, despite the progress made in understanding the internal structure of glassy materials on the nanometer scale, the problem of the structure of long-range order on the nano/micro/macro scale remains very hypothetical. Laser phosphate glasses (PhGs) have been intensively studied over the past decade, since (together with silicate glasses) they comprise an important group of compounds used in quantum electronics as active media of lasers, optical amplifiers, photosensitive elements, sensors, etc. [1–3]. Phosphate glasses are superior to their silicate counterparts in terms of optical properties. Knowledge of mechanical and microstructural characteristics is essential for detailed understanding of phenomena that occur during the manufacturing and processing of PhGs and strongly affect their operating parameters. Particularly, a correlation between structure and mechanical properties is determinative both in the reliability optimization of PhGs related to their use in optomechanical devices and in the design of other vitreous materials. The microstructure and mechanical properties of PhGs doped with ions of the rare-earth elements ((REEs), Pr, Nd, Sm, Eu, Gd, Dy, Ho, Er, Yb) were earlier analyzed in [4, 5]. In this paper, it is shown that other characteristics, such as "plasticity index" and "resistance index," are used to assess the mechanical properties of the materials and their resistance to plastic deformation, in addition to the well-known parameters *E* and *H*.

2. Experimental

The purpose of this paper is to study the mechanical properties of bulk PhGs belonging to the $Li_2O{\cdot}BaO{\cdot}Al_2O_3{\cdot}La_2O_3{\cdot}P_2O5{\cdot}R_2O_3$ and $SiO_2{\cdot}P_2O_5{\cdot}R_2O_3$ systems doped with REEs. The studied samples of PhGs were prepared by an unconventional ‘wet’ method [6]. Supervision of

microstructure evolution during the synthesis, processing, and operation of these materials will improve the nano- and micromechanical properties of these vitreous structures.

The microstructure of the sample surface was studied by optical, light (LM), and atomic force microscopy (AFM) methods. Mechanical parameters were studied by depth-sensing nano- and microidentation using a Nanotester PMT3-NI-02 device. The hardness and Young modulus calculations were carried out using the Oliver–Pharr method [7]. All of them were carried out automatically using the dedicated software.

3. Results and Discussion

Analysis of the surface microstructure of the samples using the LM method confirmed the data of [5], according to which all samples had a smooth surface without any cracks, pores, or defects. This finding indicates a high quality of the fine structure of the materials under study. Small globule-shaped entities of different colors were only observed on the polished surface of the samples (according to preliminary estimations, D_{gl} ~ 200–300 nm).

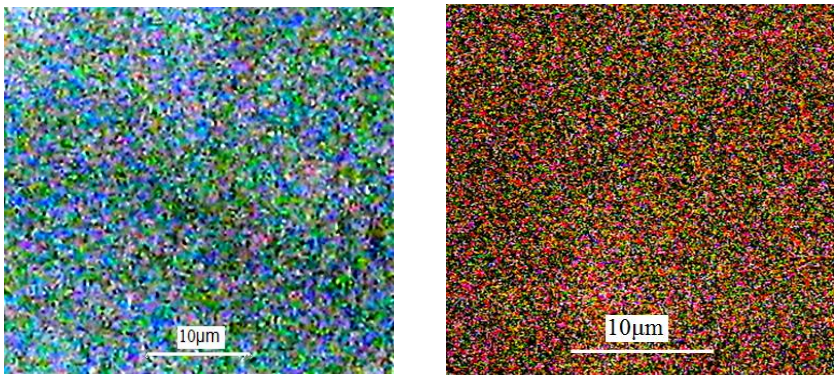

a b

Fig. 1. Surface morphology observed via LM for the PhGs samples doped with (a) Nd and (b) Pr.

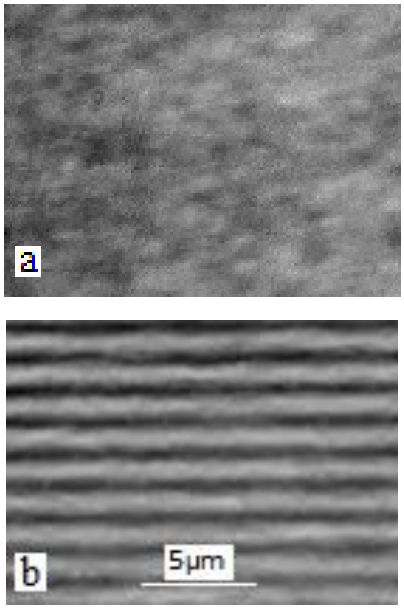

Fig. 2. LM images of the surface of the PhGs–Yb sample in (a) the normal and (b) interference mode.

This is confirmed by Fig. 1, which shows the regions of the surface of the PhGs doped with Nd and Pr. Figure 2 shows the surface relief in the interference regime for the sample containing an Yb impurity. A slight undulation of the interference lines caused by the presence of globules with a height of approximately 100 nm is observed on the surface.

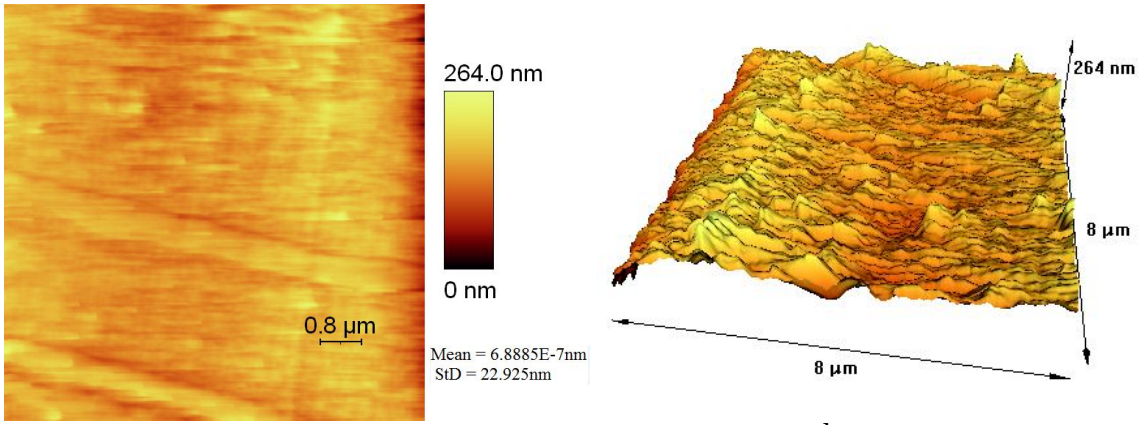

Fig. 3. (a) AFM data on the surface morphology of the sample doped with gadolinium (PhGs–Gd) and (b) a region of the surface of the PhGs–Gd sample recorded in the 3D mode.

Figure 3a shows the surface of the sample doped with gadolinium (PhGs–Gd). The pattern of globule distribution over the surface can be traced using this figure. It should be noted that the globules form unique tangles of different colors and dimension, since presumably they were formed from particles of various compositions. The same regularity can be seen for the other samples (Fig. 1). The undulated surface is more distinctly seen in the 3D mode of AFM (Fig. 3b).

Figure 4 shows results of the depth-sensing indentation tests. It should be noted that all the nano- and microindentation curves ($P(h)$) obtained for the samples under study were generally characterized by a smooth pattern of changes in the indentation depth at both the loading and unloading stages. In certain cases, at P_{max} = 500 and 900 mN, extremely slight inhomogeneity of the curves and weak undulation during the loading stage (PhGs–Yb, PhGs–Dy) were observed [5]. It is known from literature [8, 9] that breaking of atomic bonds leads to a decrease in the internal stresses in the indentation zone and thus causes an increase in the rate of penetration of the indenter into the material, due to which a nonuniform curve can be formed. Therefore, the shape of the obtained curves $P(h)$ provides data pertaining to the dynamics of the deformation process in the tested sample. Thereby, the smooth shape of the $P(h)$ curves in Fig. 4 indicates an uniform development of the process of the indenter deepening with increasing load, which can be the result of the sum of two processes, namely, the elastic compression of the crystal cell and the plastic deformation by the structure densification in the zone of load application [10, 11].

The Young's modulus (E) (Fig. 5a) and hardness (H) (Fig. 5b) exhibited a random dependence as a function of rare-earth ion atomic mass. Instead, it was found that the load value (P_{max}) affects H and E: a decrease in the peak load applied to the indenter (P_{max} = 900, 500, 100, 10 mN) was accompanied by an increase in the H and E values. The most

visible impact was observed in a range between 100 and 10 mN due to the indentation size effect (ISE) [12].

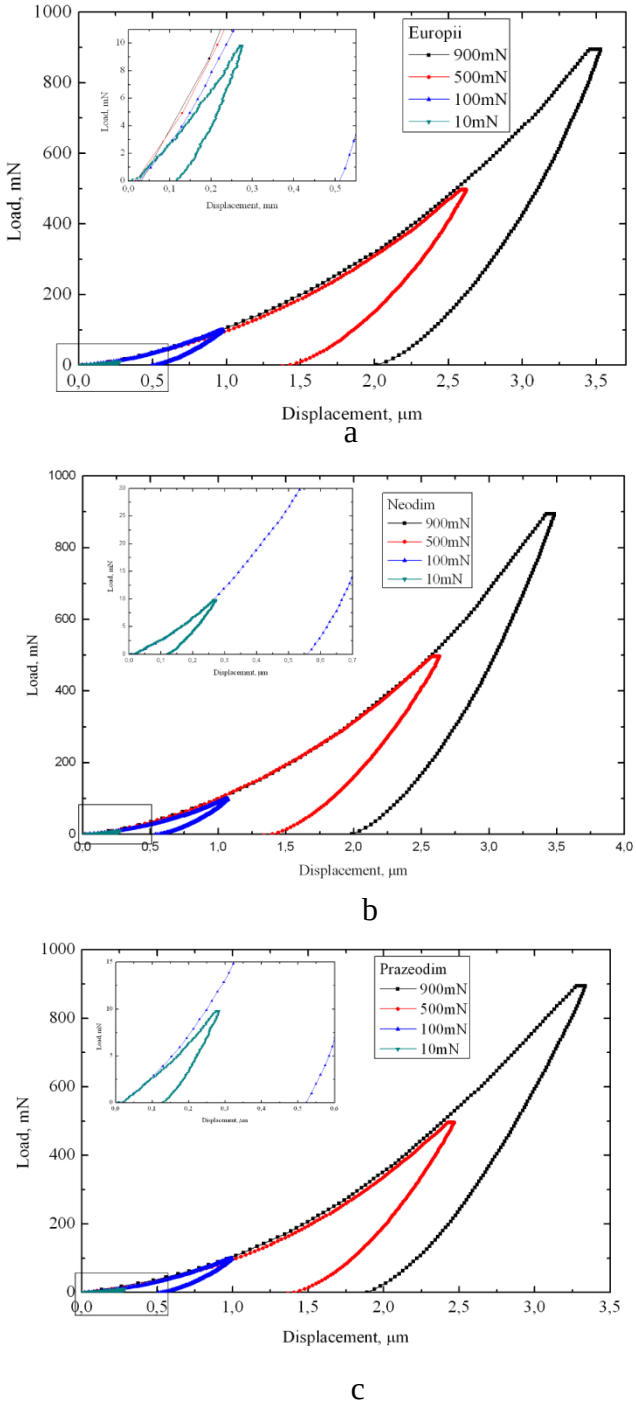

Fig. 4. Loading–unloading curves ($P(h)$) recorded at different maximum loads. Inserts: the curve for P_{max} = 10 mN on a larger scale; (a) PhG–Eu, (b) PhG–Nd, and (c) PhG–Pr.

The authors of [13] showed that the resistance of materials to plastic deformation can be determined using, in addition to well-known E and H parameters, other characteristics, such as "plasticity index" and "resistance index." These parameters describe the resistance of materials to deformation and destruction under an external concentrated load and are computed as the ratio of material hardness and Young's modulus, respectively, H/E and H^3/E^2 shown in Fig. 6. It is evident from Fig. 6 that both indexes, H/E and H^3/E^2, in common with the E and H dependences, mainly decrease with an increase in P_{max} for many studied materials. It means that the resistance to indenter penetration into the doped PhGs decreases with an increase in the load.

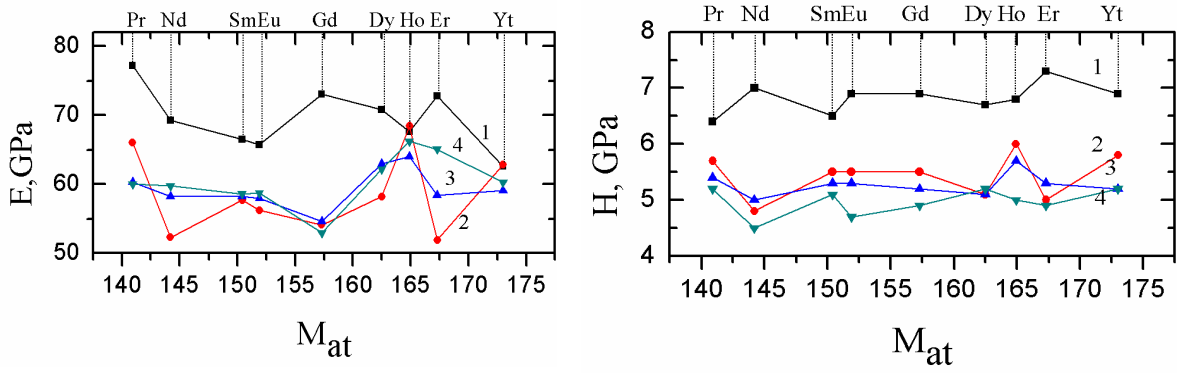

a b

Fig. 5. (a) Young modulus (E) and (b) hardness (H) as a function of REE atomic mass (M_{at}). The curves correspond to different peak values of applied load under depth-sensing indentation, P_{max} = (*1*) 10, (*2*) 100, (*3*) 500, and (*4*) 900 mN.

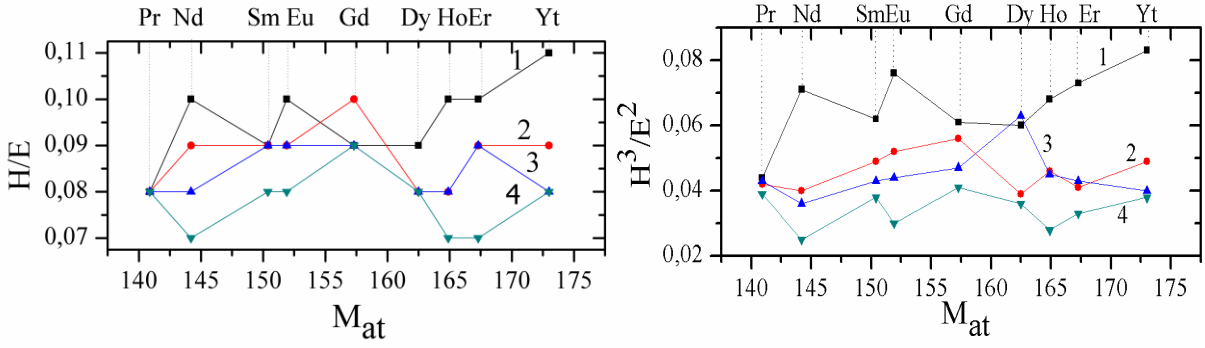

a b

Fig. 6. Variation in (a) plasticity index (H/E) and (b) resistance index (H^3/E^2) as a function of rare-earth ions atomic mass. The curves correspond to different peak values of applied load under depth-sensing indentation, P_{max} = (*1*) 10, (*2*) 100, (*3*) 500, and (*4*) 900 mN.

Comparison of the relationship between Young's modulus, hardness, plasticity indexm and resistance index with the size of ionic radii and the atomic mass of the doping REEs has not revealed a clear dependence between these parameters. Based on this fact, an assumption has been made that the elastic and plastic properties of PhGs–R are mainly determined by the internal structures of the glasses, which can contain rigid frameworks of icosahedral three-dimensional figures by analogy with the structure of the hardened gel revealed by the authors of [14].

4. Conclusions

The microstructure and mechanical properties of PhGs doped with REEs (PhGs–R, here R = Pr, Nd, Sm, Eu, Gd, Dy, Ho, Er, Yb) have been studied in this work. It has been shown that the fine structure of the surface consists of globules, which form unique tangles of different colors, presumably due to the fact that they are formed of particles with different compositions with diameters of ~200–300 nm and heights of <100 nm. The particles are appreciably densely—yet not uniformly—distributed over the surface and form a certain type of a framework structure.

The mechanical parameters, Young's modulus E, hardness H, plasticity index H/E, and resistance index H^3/E^2 exhibit a nonmonotonous dependence on the size of ionic radii and atomic mass of the doping REEs and on the load value under the depth-sensing indentation; in general, they exhibit a tendency toward decreasing with increasing load. An assumption has been made that the elastic and plastic properties of PhGs–R are mostly stipulated by the specificity of the internal structure of the glasses.

Acknowledgments

This work has been performed within the framework of the national project no. 15.817.02.06A.

References

[1] S. Jiang, T. Luo, B.C. Hwang, F. Smekatala, K. Seneschal, J. Lucas, and N. Peyghambarian, J. Non-Cryst. Solids 263–264, 364 (2000).
[2] W. Ruikun, J.D. Myers, and M.J. Myers, Proc. SPIE – Solid State Lasers X, 2001, vol. 4267, pp. 56–60.
[3] M.P. Bendett, N.A. Sanford, and D.L. Veasey, US Patent 490748, 2005.
[4] M. Elisa, C. Vasiliu, C. Grigorescu, B.A. Sava, A. Diaconu, H.J. Trodahl, and M. Dalley, Eur. J. Glass Sci. Technol. A 48 (5), 247 (2007).
[5] D.Z. Grabco, O.A. Shikimaka, M. Elisa, B.A. Sava, L. Boroica, C. Pyrtsak, A. Prisacaru, Z. Danitsa, I. Feraru, and D. Ursu, Surf. Eng. Appl. Electrochem. 48 (4), 365 (2012).
[6] M. Elisa, C. Vasiliu, C. Grigorescu, et al., Glass Tech.: Eur. J. Glass Sci. Technol. A 48 (5), 247 (2007).
[7] W.C. Oliver and G.M. Pharr, J. Mater. Res. 7 (6), 1564 (1992).
[8] Yu.S. Boyarskaya, D.Z. Grabco, and M.S. Kats, Fizika protsessov mikroindentirovaniya, Kishinev: Shtiintsa, 1986.
[9] Yu.S. Boyarskaya, R.P. Zhitaru, D.Z. Grabco, and V.A. Rahvalov, J. Mater. Sci. 33, 281 (1998).
[10] S. Yoshida, H. Sawasato, T. Sugawara, Y. Miura, and J. Matsuoka, J. Mater. Res. 25 (11), 2203 (2010).
[11] C. Hermansen, J. Matsuoka, S. Yoshida, H. Yamazaki, Y. Kato, and Y.Z. Yue, J. Non-Cryst. Solids 364, 40 (2013).
[12] W.D. Nix and H. Gao, J. Mech. Phys. Sol. 46 (3), 411 (1998).
[13] A. Leyland and A. Matthews, Wear 246 (1–2), 1 (2000).
[14] C.P. Royall, S.R. Williams, T. Ohtsuka, and H. Tanaka, Nat. Mater. 7, 556 (2008).

A HEXANUCLEAR Mn(II, III) PIVALATE CLUSTER WITH A $\{Mn_6O_2\}$ CORE

Mariana Darii

Institute of Applied Physics,
Academiei str. 5, Chisinau, MD-2028 Republic of Moldova
E-mail: mariana.darii@mail.ru

(Received November 15, 2019)

Abstract

A new $[Mn_6O_2(O_2CCMe_3)_{10}(HO_2CCMe_3)(EtOH)_3]\cdot EtOH$ hexanuclear mixed-valent coordination compound with a $\{Mn_6O_2\}$ core has been synthesized and characterized by single-crystal X-ray diffraction analysis. The central mixed-valence $[Mn^{II}_4Mn^{III}_2(\mu_4\text{-}O_2)]^{10+}$ core consists of six Mn centers, two Mn^{III} and four Mn^{II} ions, arranged as two edge-sharing flattened Mn_4 tetrahedra, with a $\mu_4\text{-}O^{2-}$ ion in the center of each tetrahedron. Peripheral ligation is provided by pivalate and ethanol groups.

1. Introduction

Hexanuclear $[Mn_6O_2(O_2CR)_{10}L_4]$ clusters (where L = neutral monodentate ligand and R = Me, Et, $CHMe_2$, CMe_3) with a central $\{Mn^{III}_2Mn^{II}_4(\mu_4\text{-}O)_2\}$ core is the most fascinating Mn oxo-carboxylate clusters used as building blocks in construction of coordination networks [1]. First, the topology of the cluster skeleton remains unchangeable, RCO_2^- carboxylate and capping ligands can be modified. Second, four capping ligands L in these clusters can be completely or partially replaced; thus, $[Mn_6O_2(O_2CR)_{10}]$ clusters can be considered as building blocks with connectivity up to four. A detailed analysis of hexanuclear $[Mn_6O_2(O_2CR)_{10}L_4]$ compounds extracted from the Cambridge Structural Database (ConQuest Version 1.19, CSD version 5.38) shows that there are more than 229 examples of these hexanuclear Mn-containing compounds with a $\{Mn^{III}_2Mn^{II}_4(\mu_4\text{-}O)_2\}$ core in which R = Me, Et, $CHMe_2$, CMe_3.

Note that the first 1D coordination polymers based on the $\{Mn_6O_2\}$ carboxylate building blocks—$[Mn_6O_2(O_2CCMe_3)_{10}(HO_2CCMe_3)_2(4,4'\text{-bpy})]_n$—were obtained by Yamashita et al. in 2002 [2]. Later on, $\{[Mn_6O_2(O_2CEt)_{10}(H_2O)_4]\cdot 2(EtCO_2H)\}_n$ [3] and $\{[Mn_6O_2(O_2CMe)_{10}(H_2O)_4]\cdot 2.5(H_2O)\}_n$ [4], in which $\{Mn_6\}$ building clusters are connected into 1D networks by shorter linkers, were prepared. In 2010, three new 1D coordination polymers $\{[Mn_6O_2(O_2CCMe_3)_{10}(Me_3CCO_2H)(EtOH)(na)]\cdot EtOH\cdot H_2O\}_n$, $\{[Mn_6O_2(O_2CCHMe_2)_{10}(pyz)_3]\cdot H_2O\}_n$ and $\{[Mn_6O_2(O_2CCHMe_2)_{10}(Me_2CHCO_2H)(EtOH)(bpe)]\cdot Me_2CHCO_2H\}_n$ (where pyrazine (pyz), nicotinamide (na), and 1,2-bis(4-pyridyl)ethane (bpe)) were reported [5].

The formation of 2D layers based on a hexanuclear $\{Mn_6O_2\}$ carboxylate motif was first reported by Ovcharenko et al. in 2013. Two new coordination polymers—$\{[Mn_6O_2(O_2CCMe_3)_{10}(ina)_2]\cdot 3(Me_2CO)\}_n$ and $\{[Mn_6O_2(O_2CCMe_3)_{10}(ina)_2]\cdot 2(EtOAc)\}_n$—were prepared using N,O-donor bridging ligands, such as isonicotinamide (ina) [6]. Employing ina and N,N′-donor aldrithiol (adt-4) spacer ligands in the reaction, new 2D coordination polymers $[Mn_6O_2(O_2CCMe_3)_{10}(ina)_2]_n$, $\{[Mn_6O_2(O_2CCMe_3)_{10}(adt\text{-}4)_2]\cdot 2(thf)\}_n$ and $\{[Mn_6O_2(O_2CCHMe_2)_{10}(adt\text{-}4)_2]\cdot(thf)\cdot 3(EtOH)\}_n$ were also synthesized [7].

Recently, a new series of hexanuclear mixed-valent $\{Mn_6O_2\}$-containing pivalate and isobutyrate clusters $[Mn_6O_2(O_2CCMe_3)_{10}(Me_3CCO_2H)_3(EtOH)]\cdot(Me_3CCO_2H)$, $[Mn_6O_2(O_2CCMe_3)_{10}(Me_3CCO_2H)_2(EtOH)_2]\cdot 2(EtOH)$, and $[Mn_6O_2(O_2CCMe_3)_{10}(Me_3CCO_2H)_2(MeOH)_2]\cdot 2(MeOH)\cdot H_2O$ and coordination polymers that incorporate these clusters, namely, $[Mn_6O_2(O_2CCHMe_2)_{10}(pyz)(MeOH)_2]_n$, $\{[Mn_6O_2(O_2CCHMe_2)_{10}(pyz)_{1.5}(H_2O)]\cdot 0.5(H_2O)\}_n$, and $[Mn_6O_2(O_2CCMe_3)_{10}(HO_2CCMe_3)_2(en)]_n$ have been synthesized (where pyz = pyrazine, en = ethyl nicotinate) [8]. As an extension of the previous study on the synthesis of oxo-bridged polynuclear hexanuclear Mn(III, II) containing clusters, herein the synthesis and X-ray characterization of a new hexanuclear $[Mn_6O_2(O_2CCMe_3)_{10}(HO_2CCMe_3)(EtOH)_3]\cdot EtOH$ (**1**) pivalate cluster compound are reported.

2. Experimental

2.1. Materials, methods, and X-ray crystallography

All reactions were run under aerobic conditions using chemical and solvents as received without further purification. The $Mn(Me_3CCO_2)_2$ precursor compound was prepared as described in [9]. A Bandelin Sonorex RK-100H ultrasonic bath operating at 45 kHz with a maximum power output of 160 W was used for the ultrasonic irradiation.

X-ray data were collected at room temperature on an Oxford Diffraction Xcalibur diffractometer equipped with a CCD area detector and a graphite monochromator utilizing MoK_a radiation (λ = 0.71073 Å). Final unit cell dimensions were determined and refined on an entire dataset. All calculations to solve the structures and refine the proposed models were carried out with the SHELX suite of programs [10]. The C-bounded H-atoms were placed in calculated positions and treated using a riding model approximation with $U_{iso}(H) = 1.5U_{eq}(C)$ for methyl group and $1.2U_{eq}(C)$ for other hydrogen atoms, while the oxygen-bounded H-atoms were found from differential Fourier maps and isotopically refined with isotropic displacement parameter $U_{iso}(H) = 1.5U_{eq}(O)$. The X-ray data and the details of the refinement for **1** are summarized in Table 1; the selected geometric parameters are given in Tables 2 and 3. The figures were drawn using the Mercury program. Crystallographic data of the new compound reported herein was deposited with the Cambridge Crystallographic Data Centre and allocated the deposition number CCDC 1972569.

2.2. Synthesis

Synthesis of $[Mn_6O_2(O_2CCMe_3)_{10}(HO_2CCMe_3)(EtOH)_3]\cdot EtOH$ (1). $Mn(Me_3CCO_2)_2$ (0.10 g, 0.38 mmol) and N-phenyldiethanolamine (0.018 g, 0.09 mmol) were dissolved in an $EtOH/CH_2Cl_2$ mixture (4 mL/4 mL). The resulting brown solution was treated in an ultrasonic bath for 30 min. The solution was filtered off and allowed to evaporate slowly at room temperature. Brown crystals of **1** suitable for X-ray measurements were obtained within 1 week, washed with EtOH, and dried in air. Yield (based on Mn): 0.064 g, 60 %.

3. Results and Discussion

The reaction of manganese(II) pivalate with N-phenyldiethanolamine in an $EtOH/CH_2Cl_2$ mixture results in a new hexanuclear compounds with a stable $[Mn_6O_2(O_2CCMe_3)_{10}]$ unit, while comprising a coordinated neutral monodentate ligand: one pivalic and three ethanol molecules in

$[Mn_6O_2(O_2CCMe_3)_{10}(HO_2CCMe_3)(EtOH)_3]\cdot EtOH$ (**1**).

X-ray analysis showed that the cluster contains a $\{Mn^{II}_4Mn^{III}_2O_2\}^{10+}$ core of two edge sharing Mn_4 tetrahedra with a μ_4-O^{2-} ion in the center of each tetrahedron. Peripheral ligation is provided by ten bridging pivalate monoanionic ligands (Fig. 1a). Four of them coordinate in a μ_3-mode and bridge three Mn centers, whereas each of the other six bridges two Mn centers in a μ_2-mode.

The shortest intracluster Mn^{III}_1–Mn^{III}_2 distance, being 2.8108(11) Å, is formed by two Mn^{III} ions that occupied the common edge of the Mn_4 tetrahedra, with a μ_4- O_2 –ion in the center of each tetrahedron. All other Mn^{III}–Mn^{II} and Mn^{II}–Mn^{II} bond distances in Mn_4 tetrahedra are longer (3.145(2)–3.169(1) and 3.720(2)–4.837(1) Å, respectively). In **1**, two peripheral Mn atoms (Mn_5 and Mn_6) in Mn_4 tetrahedra are additionally capped by ethanol molecules. Two peripheral Mn atoms in the second Mn_4 tetrahedra (Mn_3 and Mn_4) are capped by ethanol and pivalic acid molecules. All Mn^{II} atoms have a near-octahedral surrounding. The Mn^{III} ions (Mn_1 and Mn_2) have an elongated octahedral MnO_6 environment. The axial and equatorial Mn^{III}–O bond distances are in the range of 2.211(2)–2.275(5) and 1.883(4)–1.978(2) Å, respectively. Selected bond distances are summarized in Table 2. Four terminal Mn atoms are in the lower oxidation state +2 and have longer Mn–O_{carb} bond distances ranging from 2.333(5) to 2.370(6) Å.

Analysis of the mode of packing of the components revealed a system of inter- and intra-molecular O–H…O hydrogen bonds in **1** (Fig. 1b, Table 3). The coordinated pivalic acid forms a short intramolecular hydrogen bond O(24)–H(24)...O(22) of 2.559(8) Å with the bridging pivalate. The solvent EtOH molecule forms intermolecular O–H···O hydrogen bonds (2.59(3), 2.65(4), and 2.73(2) Å) with the coordinated EtOH and pivalate molecules from $\{Mn_6\}$ cluster.

Table 1. Crystal data and structure refinement for **1**

Empirical formula	$C_{67}H_{126}Mn_6O_{30}$	V, Å^3	2265.4(3)
Formula weight	1741.31	D_{calc} (g /cm^{-3})	1.276
T (K)	293(2)	μ(mm^{-1})	0.880
Crystal system	Triclinic	F(000)	918
Space group	P-1	Crystal size (mm)	0.50 × 0.50 × 0.40
Z	1	Reflections collected/unique	3.112 / 25.048
a, Å	13.5932(7)	Reflections with $I > 2\sigma(I)$	15038
b, Å	14.0742(7)	Data/restraints/parameters	10367 / 252 / 917
c, Å	15.2032(9)	Goodness-of-fit on F^2	1.001
α (º)	114.592(5)	R_1, wR_2 [$I > 2\sigma(I)$]	0.0438, 0.1151
β (º)	90.231(5)	R_1, wR_2 (all data)	0.0543, 0.1240
γ (º)	117.874(5)	$\Delta\rho_{max}$, $\Delta\rho_{min}$, (e·Å^{-3})	0.586 and –0.298

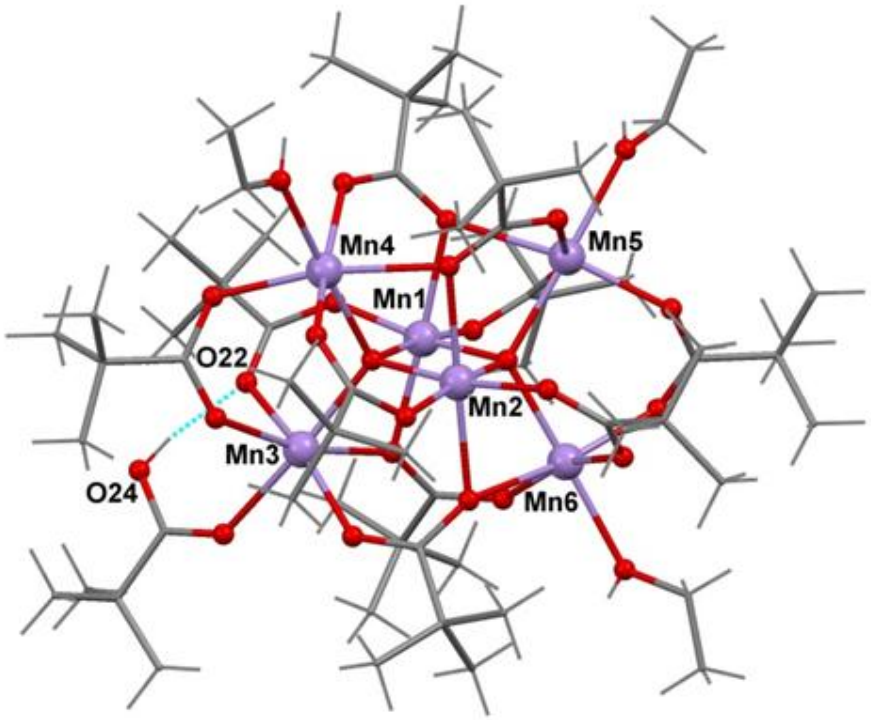

(**a**)

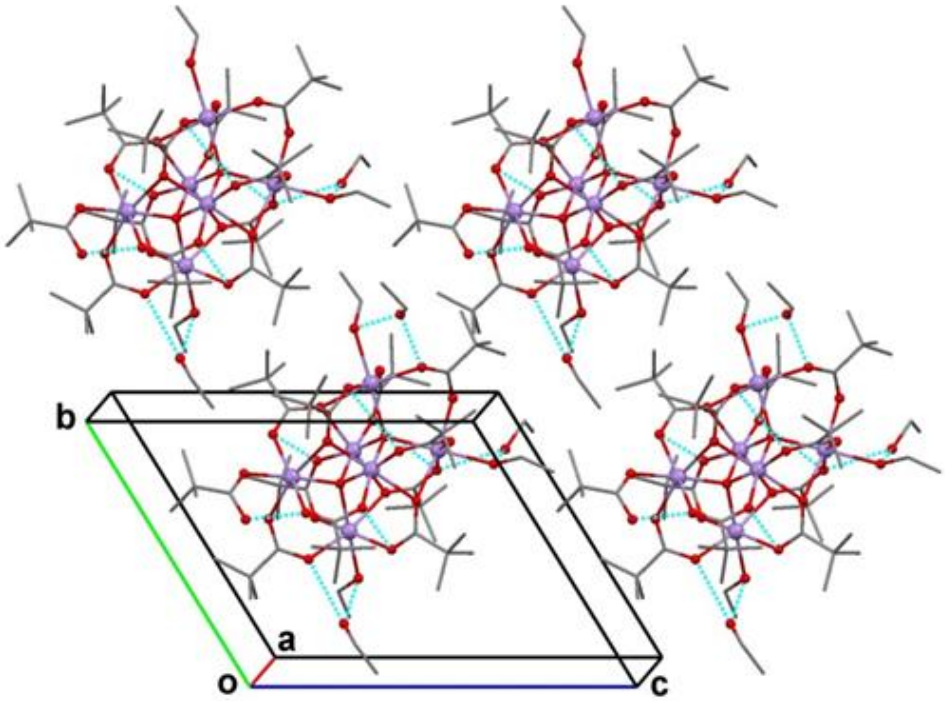

(**b**)

Fig. 1. Molecular structure (a) and fragment of crystal packing (b) in **1**. Color code: Mn is denoted by purple spheres; O, red balls; C, grey sticks; and H, grey lines.

Table 2. Selected bond distances (Å) for **1**

Mn(1)-O(1)	1.888(4)	Mn(4)-O(7)	2.140(5)
Mn(1)-O(2)	1.880(4)	Mn(4)-O(9)	2.334(5)
Mn(1)-O(8)	2.250(5)	Mn(4)-O(25)	2.257(6)
Mn(1)-O(16)	1.951(4)	Mn(5)-O(2)	2.180(4)
Mn(1)-O(18)	2.229(4)	Mn(5)-O(8)	2.322(5)
Mn(1)-O(21)	1.967(4)	Mn(5)-O(10)	2.152(5)
Mn(2)-O(1)	1.901(4)	Mn(5)-O(13)	2.122(6)
Mn(2)-O(2)	1.896(4)	Mn(5)-O(15)	2.154(4)
Mn(2)-O(6)	1.949(4)	Mn(5)-O(26)	2.251(5)
Mn(2)-O(9)	2.246(5)	Mn(6)-O(2)	2.177(4)
Mn(2)-O(11)	1.952(5)	Mn(6)-O(12)	2.126(5)
Mn(2)-O(19)	2.240(5)	Mn(6)-O(14)	2.143(6)
Mn(3)-O(1)	2.160(4)	Mn(6)-O(17)	2.129(5)
Mn(3)-O(3)	2.101(5)	Mn(6)-O(19)	2.371(5)
Mn(3)-O(18)	2.325(5)	Mn(6)-O(27)	2.259(6)
Mn(3)-O(20)	2.090(5)	Mn(1)-Mn(2)	2.811(1)
Mn(3)-O(22)	2.218(4)	Mn(1)-Mn(3)	3.155(1)
Mn(3)-O(23)	2.256(5)	Mn(1)-Mn(5)	3.145(1)
Mn(4)-O(1)	2.176(4)	Mn(2)-Mn(4)	3.169(1)
Mn(4)-O(4)	2.137(5)	Mn(2)-Mn(6)	3.165(1)
Mn(4)-O(5)	2.128(5)		

Table 3. Selected hydrogen bonds (Å) for **1**

D-H...A	d(D-H)	d(H...A)	d(D...A)	∠(DHA)	Symmetry transformation for A
O(24)-H(24)...O(22)	0.82	1.75	2.559(8)	169	x, y, z
O(25)-H(25D)...O(28A)	0.85	2.04	2.65(4)	129	x, y, z
O(26)-H(26A)...O(30)	0.85	2.21	2.73(2)	120	x+1, y, z
O(27)-H(27A)...O(29A)	0.85	1.98	2.59(3)	128	x, y+1, z

4. Conclusions

A new $[Mn_6O_2(O_2CCMe_3)_{10}(HO_2CCMe_3)(EtOH)_3]\cdot EtOH$ hexanuclear mixed-valent coordination compound with a $\{Mn^{III}_2Mn^{II}_4(\mu_4\text{-}O)_2\}$ core has been synthesized and characterized by single-crystal X-ray diffraction analysis. The synthesized mixed–valent hexanuclear carboxylate manganese coordination cluster can be used as a supramolecular building block and offers additional possibilities for crystal engineering of new interesting materials with high porosity and magnetic properties and new avenues to be explored.

References

[1] S.G. Baca, in Advances in Chemistry Research, ed. by J.C. Taylor (Nova Science Publishers, New York, (2018), vol. 43, ISBN: 978-1-53613-079-9.
[2] K. Nakata, H. Miyasaka, K. Sugimoto. T. Ishii, K. Sugiura, and M. Yamashita, Chem. Lett. 31, 658 (2002). doi: 10.1246/cl.2002.658.
[3] C.-B. Ma, M.-Q. Hu, H. Chen, C.-N. Chen, and Q.-T. Liu, Eur. J. Inorg. Chem. 2008 (33), 5274 (2008). doi.org/10.1002/ejic.200800508.
[4] E.E. Moushi, A.J. Tasiopoulos, and M.J. Manos, Bioinorg. Chem. Appl. 2010, 367128 (2010). doi:10.1155/2010/367128.
[5] I.L. Malaestean, V.C. Kravtsov, M. Speldrich, G. Dulcevscaia, Y.A. Simonov, J. Lipkowski, A. Ellern, S.G. Baca, and P. Kögerler, Inorg. Chem. 49, 7764 (2010). doi: 10.1021/ic100541m.
[6] E.Y. Fursova, V.I. Ovcharenko, A.S. Bogomyakov, and G.V. Romanenko, J. Struct. Chem. 54, 164 (2013). doi: 10.1134/S0022476613010241.
[7] I.L. Malaestean, A. Ellern, J. van Leusen, V.C. Kravtsov, P. Kögerler, and S.G. Baca, Cryst. Eng. Comm. 16, 6523 (2014). doi.org/10.1021/ic100541m.
[8] M. Darii, I.G. Filippova, J. Hauser, S. Decurtins, S.-X. Liu, V.Ch. Kravtsov, and S.G. Baca, Crystals 8, 100 (2018). doi:10.3390/cryst8020100.
[9] S.G. Baca, I.L. Malaestean, T.D. Keene, H. Adams, M.D. Ward, J. Hauser, A. Neels, and S. Decurtins, Inorg. Chem. 47, 11108 (2008). doi: 10.1021/ic8014145.
[10] G.M. Sheldrick, Acta Crystallogr. A64, 112 (2008). doi.org/10.1107/S0108767307043930.

SPECTRAL AND DYNAMICAL CHARACTERIZATION OF MULTIEXCITON COMPLEXES IN CdSe/CdS/CdZnS COLLOIDAL QUANTUM DOTS

V. I. Pavlenko[1], I. V. Beloussov[1], I. I. Dobynde, and D. I. Ozol[2]

[1]Institute of Applied Physics, Chisinau, Republic of Moldova
[2]Moscow Institute of Physics and Technology, Dolgoprudny, Moscow oblast, Russian Federation
E-mail: pavlenko@phys.asm.md

(Received August 15, 2019)

Abstract

The kinetics of a strongly nonequilibrium state of electrons and holes excited in quantum dots by a long laser pulse in the *p*-states are studied using time-resolved photoluminescence. Three bands of the transient photoluminescence spectra are identified, and the ignition and decay of each of them is studied. The complex picture of the time evolution of the bands is attributed to the fast processes of cascade intraband relaxation and the Pauli Exclusion Principle. The durations of the formation and decay for each of the photoluminescence bands are determined.

1. Introduction

Multiexciton states in semiconductor quantum dots (QDs) with two or more excited electron–hole (e–h) pairs play an important applied role in some devices, such as lasers, photodetectors, solar cells, light-emitting diodes, and photon pair sources [1–6]. Owing to the enhanced interaction of charge carriers under conditions of quantum confinement, multiexcitons in QDs are scattered mainly through a nonradiative Auger process; effective photoluminescence (PL) can be implemented only by single excitons [1, 7]. In the simplest two-exciton case, the biexciton in an ordinary CdSe QD can emit a photon during its subnanosecond Auger lifetime [8], which is much shorter than the radiation lifetime of tens of nanoseconds for the remaining single exciton. This transient presence of biexcitons is not pronounced in time-integrated (or *cw*) PL spectra and necessitates the use of ultrafast spectroscopic techniques and high-sensitivity experiments to detect their fundamental optoelectronic properties, such as PL lifetimes, spectral positions, and binding energies [9–15].

The relaxation kinetics of two, three, and four e–h pairs in CdSe QDs were studied in [1] using femtosecond transient absorption spectroscopy. It was shown that the relaxation cascades are mediated by Auger processes. The studies of ultrafast PL of colloidal CdSe/ZnS QDs were carried out in [10]. A new transient emission band red-shifted by about 10–30 meV relative to the band-gap luminescence was extracted. The authors attributed it to the neutral biexciton with extremely short measured lifetimes (100 ps for a QD radius of 3.5 nm) in agreement with transient absorption studies of the two e–h pairs in [1]. The bands associated with the radiative decay of the single exciton, biexciton, and triexciton in the transient spectra of time-resolved PL were clearly observed in [11] for CdSe QD in hexane. The detailed study of the multiexcitonic effects in CdSe QDs, based on the energetics, the lifetimes, and the pump-power dependence of the various emission bands was presented in [12, 13]. All measurements in [10–13] were performed at room temperature. We also draw attention to works [14–17] on this issue. It was shown in [10, 11, 13] that the positions of the exciton and biexciton bands do not depend on the

pump power; this fact suggests that each of them is due to the emission from QDs in the well-defined one- and two-particle states.

To interpret the time evolution of the system, the following scenario was expected. Initially, the sample is excited by an ultrashort laser pulse, so that a certain number of e–h pairs with the energy much higher than the QD energy gap are generated in a selected QD. For example, in [11] a pulse of 300 fs at 400 nm was used. After that, the system was left to itself (without any external influence). At the next stage, the electrons and holes relax to the lowest states on a picosecond time scale [18–22] due to the fast intraband Auger-like and phonon emission processes. Next, at the third stage, a relatively slow process of recombination of e–h pairs occurs within a time interval of a few tens of picoseconds to a few tens of nanoseconds. This final stage of the time evolution of the system can be described by a simple set of coupled rate equations [11] and reflects in the time-resolved kinetics of PL studied in [10–13].

After rapid intraband relaxation, a quasi-equilibrium state is established in the sample. In different QDs, one (exciton) to several (multiexciton) e–h pairs can be excited depending on the excitation intensity. Their number in the selected QD is described by the Poisson statistics [18]. The Poisson distribution is valid, if the probability of generating the e–h pair in a QD is independent of the number of e–h pairs already existing in it [23]. Therefore, it is applicable for the case of ultrashort pulse excitation well above the PL band edge and makes it possible to supplement the set of rate equations by the initial conditions [11].

The population of the QD states can change quite rapidly; a high time resolution is required to study the dynamics. Therefore, in experiments of [10–13], ultrashort laser pulses and high-resolution measuring equipment were used. In this paper, we report that PL from biexciton states in QD can be observed by more modest measuring means and with a laser pulse whose duration is comparable to the lifetime of biexcitons and far exceeds the intraband relaxation time.

2. Main Results

The time-resolved PL triggered by a ~30-ps-long exciting pulse centered at the time of 154 ps was studied. The use of long pulses makes it possible not only to trace the decay of multi-exciton complexes, but also to study the process of their formation and, thus, give a more complete picture of the physical processes occurring in the system. In addition, in contrast to [10–13], to achieve a fast relaxation to the lowest state, we excite e–h pairs by a laser directly near the *p*-states.

From the spectrogram with ~50 ps resolution, the temporal trace of PL in the main (low-energy) spectral range was obtained. The entire process of the PL decay can be conventionally divided into three consecutive stages (I, II, and III) characterized by the different rates of intensity decrease. We will assume that this difference is associated with sequential processes; in each of them, the decay of a spectral component is accompanied by the excitation of the other, lower-lying energy state. However, unlike these works, we will not assume a single- or multi-exponential character of the decay, expecting that, while some states are depleted, the filling of others can increase, and their decay will begin later. Therefore, the total radiation from these states will not have a simple form of decreasing exponents in the entire studied PL region.

The fitting function for the time-integrated PL spectrum can be decomposed into two Gaussian functions and a constant part that takes into account the noise background. The first of these functions, which is associated with the radiation from the *s*-states of electrons and holes, has a maximum at 1.98 eV and a full width at half maximum of the peak of ~100 meV. The second function, which is associated with radiation from the *p*-states, significantly overlaps the

first one and has a maximum at 2.1 eV and a width of ~340 meV. A strong overlap of the spectral bands occurs due to the inhomogeneous broadening associated with the size dispersion of the QDs. Since the radiation of biexcitons is a fast transient process, the time-integrated PL spectrum does not contain any information about their presence. However, they can be detected by studying transient spectra at different points in time. This would make it possible to determine some parameters of biexcitons, such as binding energy, excitation, and decay times.

We obtained a series of transient PL spectra extracted at different delays relative to the center of the exciting laser pulse using a 50 ps integration window. The asymmetric fitting function can be presented as a sum of three Gaussian components $F_i \exp\left(-\left(\varepsilon-\varepsilon_i\right)^2/\gamma_i^2\right)$ centered at $\varepsilon=\varepsilon_i$ $(i=x,xx,xxx)$ and some background constant F. We associate the broad peak in each transient PL spectrum described by the Gaussian function with a maximum at $\varepsilon_{xxx}=2.1\,\text{eV}$ with the radiative recombination of e–h pairs in *p*-states. It rapidly disappears; however, since it has a large width, it also appears in the time-integrated spectrum. The high peak at $\varepsilon_x=1.98\,\text{eV}$ makes a major contribution to the time-integrated spectrum. We associate it with the decay of single excitons. Finally, we interpret the peak at $\varepsilon_{xx}=1.92\,\text{eV}$, which first arises and then disappears, as the decay of biexcitons [11]. This peak is relatively low and strongly overlapped by the other peaks; therefore, we can say that *biexcitons hide behind excitons*. The binding energy $2\varepsilon_x-\varepsilon_{xx}$ of two excitons in the biexciton is $60\,\text{meV}$.

Comparison of the spectral dependences shows that the parameters of the fitting function change with time. To find out how this occurs, let us study the time dependences of the amplitudes of Gaussian functions and their widths. The results are shown in Figs. 1 and 2.

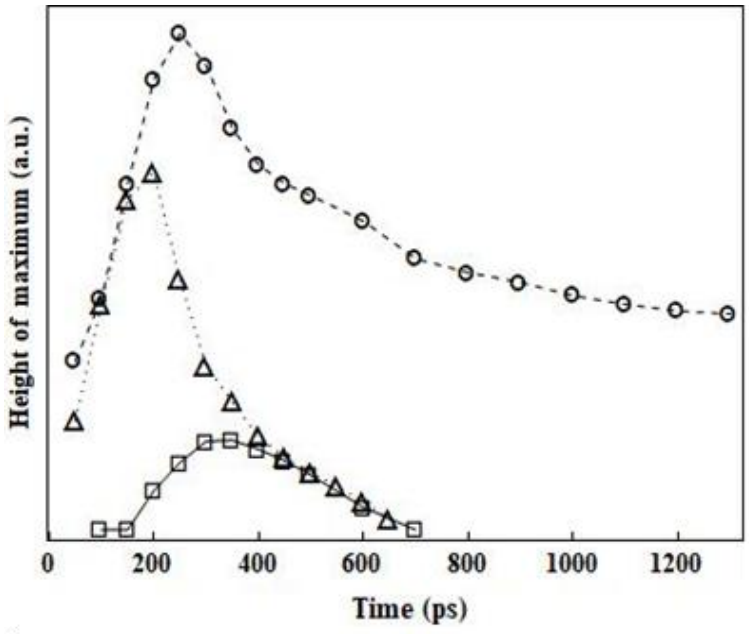

Fig. 1. Time dependence of the height of the maximum of the fitting function at $\varepsilon=\varepsilon_x$ (circles), $\varepsilon=\varepsilon_{xx}$ (squares), and $\varepsilon=\varepsilon_{xxx}$ (triangles).

It is evident from Figs. 1 and 2, the laser pulse excites radiation mainly from the *p*-states of electrons and holes that occurs in a wide energy range and reaches a maximum value at 200 ps. Simultaneously, radiation appears from the *s*-states. It has an almost unchanged spectral range and reaches a maximum at 250 ps. The emission of biexcitons appears with even greater delay and much slower. It ceases to grow at 350 ps when two previous PL bands are already significantly reduced. The spectral range where this radiation occurs hardly changes either. Starting from 350 ps, the decay of triexcitons is accompanied by the decay of biexcitons within ~140 ps. The decrease in radiation from single excitons slows down within this time interval. After 700 ps, only an extremely slowly decreasing emission of single excitons occurs; it can be described by a simple exponential curve. Using the exponential function for fitting only at times longer than 700 ps, we obtain a value of ~10 ns for the decay time of a single exciton.

We assume that all microscopic processes occurring in the system can be divided into fast and slow ones. The accuracy of the measurements does not allow us to follow the fast processes; however, we can take into account the results of their actions. These processes involve an Auger-like scattering of the electron by the hole and subsequent intraband relaxation of the scattered hole with emission of phonons. This sequence of processes leads to the fact that e–h pairs excited by a laser pulse near the $1P_e$–$1P_{3/2}$ state are converted into e–h pairs in the lowest $1S_e$– $1S_{3/2}$ state. Moreover, due to the described mechanism of intraband relaxation, the formation of pairs in the *s*-states may continues even after the end of the action of the laser pulse, if this is allowed by the filling of the $1S_e$–$1S_{3/2}$ states of the e–h pairs in accordance with the Pauli Exclusion Principle. The number of pairs in *p*-states at this time decreases. This explains the behavior of the curves in Fig. 1 within the time interval of 100–200 ps.

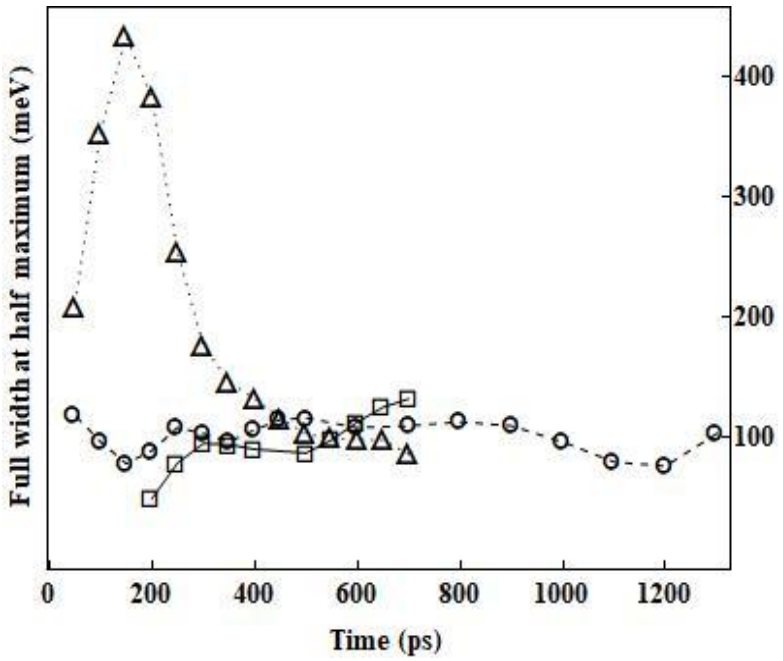

Fig. 2. Time dependence of the width of the maximum of the fitting function at $\varepsilon = \varepsilon_x$ (circles), $\varepsilon = \varepsilon_{xx}$ (squares), and $\varepsilon = \varepsilon_{xxx}$ (triangles).

If there is only one e–h pair in the *s*-states, then, taking into account the Coulomb interaction, we can speak about the formation of an exciton. If the number of e–h pairs in this state reaches a maximum value equal to two, we can speak about the formation of a biexciton. In this terminology, the appearance of the second pair in the state where one pair is already present automatically means the disappearance of both pairs (or two excitons) and the formation of a biexciton. The second pair, like the first one, can rapidly transit to the *s*-state from the *p*-state as a result of fast intraband relaxation. In this case, the appearance of a biexciton means the disappearance of one pair from the *s*-state and one pair from the *p*-state. The corresponding behavior of the curves in Fig. 1 manifests itself within the time interval of 200–350 ps, where the ignition of the biexciton band of PL is accompanied by a rapid decrease in both the radiation from the single excitons and the emission from the e–h pairs in the *p*-states.

By the time of 350 ps, the generation of biexcitons seems to reach saturation, and their decay begins. We can consider the annihilation of any constituent e–h pair of the biexciton as a decay of the biexciton resulting in the creation of an exciton and a photon. The remaining pair can also annihilate; this means a radiative decay of the exciton. Another channel for the biexciton's decay is associated with an Auger-like interband process where the annihilating e–h pair transfers its energy to an electron or hole of the second e–h pair. It is evident that the biexciton and exciton decay processes are slower than those indicated for the formation of excitons and biexcitons. Note that the decay of the biexciton PL band in the interval of 350–700 ps is accompanied by almost the same decay of other bands. In our opinion, this fact also indicates the saturation of biexciton states. Electrons and holes in the *p*-states *do not hasten* to radiatively recombine; instead, they wait for an opportunity to stay in a lower energy state.

Thus, stage I of the PL decay corresponding to the peak is the shortest and fastest; it has the widest spectrum and associated with the recombination of electrons and holes from the *p*-states. Stage II located at the foot of the peak is characterized by complex processes associated with both the formation and decay of biexcitons and the slowing down of the decay of triexcitons and single excitons. Finally, the slowest stage III located in the tail of the dependence is associated with the radiative decay of single excitons.

3. Conclusions

We excited electrons and holes near the energy of the *p*-states expecting to get their fast relaxation in one step. However, the obtained results are extremely different from those previously described in [10–13], where the excitation was high in the energy zone. We managed to trace not only the disintegration of the main PL bands, but also their ignition.

This finding gives evidence that the allowance for the Pauli Exclusion Principle plays a significant role in the description of the temporal evolution of the system. An external pulse can excite only six e–h pairs in the *p*-state, while the *s*-states are ready to accept only two. Therefore, the pair conversion from *p*- to *s*-state does not occur until the *s*-state is at least partially vacant. The results show that, in our case, the Poisson distribution cannot be used as an initial condition for the rate equations at any fixed point in time. The rate equations themselves cannot be linear, since one should take into account the saturation of the state of Fermi particles.

References

[1] V. I. Klimov, A. A. Mikhailovsky, S. Xu, A. Malko, J. A. Hollingsworth, C. A. Leatherdale, H.-J. Eisler, and M. G. Bawendi, Science 290, 314 (2000).
[2] V. Sukhovatkin, S. Hinds, L. Brzozowski, and E. H. Sargent, Science 324, 1542 (2009).
[3] J. B. Sambur, T. Novet, and B. A. Parkinson, Science 330, 63 (2010).
[4] O. E. Semonin, J. M. Luther, S. Choi, H.-Y. Chen, J. Gao, J. Nozik, and M. C. Beard, Science 334, 1530 (2011).
[5] W. K. Bae, Y.-S. Park, J. Lim, D. Lee, L. A. Padilha, H. McDaniel, I. Robel, C. Lee, J. M. Pietryga, and V. I. Klimov, Nat. Commun. 4, 2661 (2013).
[6] B. Fisher, J. M. Caruge, D. Zehnder, and M. Bawendi, Phys. Rev. Lett. 94, 087403 (2005).
[7] J. Zhao, G. Nair, B. R. Fisher, and M. G. Bawendi, Phys. Rev. Lett. 104, 157403 (2010).
[8] H. Htoon, J. A. Hollingsworth, R. Dickerson, and V. I. Klimov, Phys. Rev. Lett. 91, 227401 (2003).
[9] V. Klimov, S. Hunsche, and H. Kurz, Phys. Rev. B 50 8110 (1994).
[10] M. Achermann, J. A. Hollingsworth, and V. I. Klimov, Phys. Rev. B 68, 245302 (2003).
[11] J.-M. Caruge, Y. Chan, V. Sundar, H. J. Eisler, and M. G. Bawendi, Phys. Rev. B 70, 085316 (2004).
[12] C. Bonati, M. B. Mohamed, D. Tonti, G. Zgrablic, S. Haacke, F. van Mourik, and M. Chergui, Phys. Rev. B 71, 205317 (2005).
[13] C. Bonati, A. Cannizzo, F. van Mourik, and M. Chergui, Proc. SPIE 6892, 68920H-11 (2008).
[14] M. Marceddu, M. Saba, F. Quochi, A. Lai, J. Huang, D. V. Talapin, A. Mura, and G. Bongiovanni, Nanotechnology 23, 015201 (2012).
[15] S. Kono, A. Kirihara, A. Tomita, K. Nakamura, J. Fujikata, K. Ohashi, H. Saito, and K. Nishi, Phys. Rev. B 72, 155307 (2005).
[16] C. Smith and D. Binks, Nanomaterials 4, 19 (2014).
[17] Y. Choi, S. Sim, S. J. Lim, and Y. H. Lee, and H. Choi, Sci. Rep. 3, 3206 (2013).
[18] Al. L. Efros, V. Kharchenko, and M. Rosen, Solid State Commun. 93, 281 (1995).
[19] V. I. Klimov and D. W. McBranch, Phys. Rev. Lett. 80, 4028 (1998).
[20] V. I. Klimov, D. W. McBranch, C. A. Leatherdale, and M. G. Bawendi, Phys. Rev. B 60, 13740 (1999).
[21] V. I. Klimov, J. Phys. Chem. B 104, (26) 6112 (2000).
[22] P. Guyot-Sionnest, M. Shim, and C. Wang, Nanocrystal Quantum Dots, 2nd ed., CRCPress,Taylor and Francis Group, ch. 4., pp. 133–145, 2010.
[23] V. I. Klimov, Semiconductor and Metal Nanocrystals: Synthesis and Electronic and Optical Properties, vol. I, Marcel Dekker: New York, ch. 5, pp. 153–206, 2003.

IMPACT OF HEAT AND MASS TRANSFER ON THE UNSTEADY SQUEEZING FLOW OF A NANOFLUID WITH MULTIPLE CONVECTIVE CONDITIONS

A. Sarkar and P. K. Kundu

Dept. of Mathematics, S.A. Jaipuria College, Kolkata, West Bengal, 700005 India
Dept. of Mathematics, Jadavpur University, Kolkata, West Bengal, 700032 India
E-mail: amitformath@gmail.com, kunduprabir@yahoo.co.in

(Received June 9, 2019)

Abstract

In this study, the effect of multiple convective conditions on a viscous unsteady incompressible electrically conductive nanofluid is analyzed. In addition, the fluid is squeezed between two parallel plates in the presence of an applied magnetic field. Nonlinear partial differential equations are remodelled into ordinary ones by introducing similarity transformations, which are solved numerically using the shooting iteration technique together with the Runge–Kutta sixth-order integration scheme; after that, the impact of affined parameters on the temperature and velocity distribution is shown by means of tables and graphs. Our studies suggest that the fluid temperature and the heat transfer rate decrease with the squeeze parameter.

1. Introduction

Studies of heat and mass transfer of a viscous liquid in squeezing drift are important not only for chemical/mechanical engineering (polymer processing, compressing, chemical material loading, and chocolate filtering) but also for our every day life's relevancy. The first study in this context was conducted by Stefan [1]. Mahmood et al. [2] numerically depicted the squeezed Newtonian flow over a porous surface. An axisymmetric and 2D squeezing drift was exhibited by Rashid et al. [3]. Siddiqui et al. [4] addressed the squeezing flow of a magnetic hydrodynamic fluid between infinite parallel plates. Domairry and Aziz [5] analytically extracted a solution for the squeezing flow of a viscous fluid between two parallel disks with blowing. Later, the above work was extended by Hayat et al. [6] to analyze second-grade fluids. Mustafa [7] revealed the squeezing flow of an unsteady viscous liquid. In the presence of Brownian motion, Sheikholeslami et al. [8] analytically (DTM) studied the flow characteristics of a nanofluid drift between two parallel plates. The literature that spotlighted these achievements can be traversed in [9–12].

In the boundary layer drift scenario, two types of conditions—specified surface temperature and specified surface heat flux—are commonly used. It takes place when a linear correlation exists between the surface temperature and the surface heat transfer. Usually, under conditions of Newtonian heating, which is well known as a conjugate convection flow, heat is issued to the convective fluid via the boundary layer with a finite heat capacity. This phenomenon in heat transport rate depends on the local difference in the temperature with the ambient situations. This transcendent aspect of Newtonian heating occurs in many vital engineering devices, such as heat exchanger devices. Relevant studies regarding convective boundary conditions were conducted in [13–16]. Aziz and Khan [17], Das et al. [18], Uddin et al. [19] discussed the convective boundary layer flow of a nanofluid over a convectively heated

surface.

The convective heat transfer phenomenon for nanofluid flows over a shrinking sheet was studied by Das et al. [20]. Diversely, in many engineering and technological fields, the solutal boundary condition does a momentous job in the mass transport problems. Tanveer et al. [21] studied the peristaltic flow of a Jeffery nanofluid drift through a curved channel with multiple convective boundary conditions. In that study, they used the mechanism for both heat and mass transfer convective conditions and solved the problem numerically. Recently, multiple convective conditions for non-Newtonian nanofluids have been authorized by Uddin et al. [22]. Later on, Uddin et al. [23] used multiple convective boundary conditions in their study on the free convective dilatant nanofluid flow through a Darcian porous medium. The domination of the second-order slip on nanofluid flow through a permeable sheet was scrutinized by Acharya et al. [24].

In this paper, the foremost objective is to study the aftermath of multiple convective boundary conditions on a squeezing nanofluid flow between two parallel plates. The similarity solutions are derived and used to predict the heat and mass transfer characteristics of the flow. The coordination of the piece is given as follows. Section 2 deals with the mathematical formulation of the flow model. The numerical method and validation of the code are given in Section 3. Results and discussion are presented in Section 4. Conclusions are summarized in Section 5.

2. Mathematical Formulation of the Problem

Consider an unsteady symmetric squeezing nanofluid flow between two parallel plates, as shown in Fig. 1. The fluid is assumed to be incompressible and electrically conducting. In addition, the distance between these plates is $h(t) = H(1 - \alpha t)^{1/2}$, where the plates are squeezed and separated to each other for $\alpha > 0$ and $\alpha < 0$, respectively. Let us consider an unsteady symmetric flow of an incompressible electrically conducting viscous nanofluid between two parallel plates separated by a variable distance $h(t) = H(1 - \alpha t)^{1/2}$, where α is a characteristic parameter having dimensions of time inverse. The upper plate at $y = h(t)$ is approaching the lower stationary plate at $y = 0$ at velocity $v(t)= dh/dt$ until they touch each other, as shown in Fig. 1. A uniform magnetic field of strength $B(t) = B_0(1-\alpha t)^{-1/2}$ (Fig. 1) is adopted perpendicular to the plates where B_0 is the initial intensity of the magnetic field. Here, the electric field is taken as zero. The magnetic Reynolds number is presumed to be small so that the induced magnetic field can be ignored. In the mathematical formulation of the problem, it is supposed that there is no chemical reaction and radiative heat transfer. All body forces are presumed to be ignored. The entire nanofluid structure is in local thermodynamic equilibrium.

Under the stated assumptions, the governing conservation equations in an unsteady state can be expressed as follows [11, 12]:

$$u_x + v_y = 0, \tag{1}$$

$$\rho\left(u_t + uu_x + \mathrm{v}u_y\right) = -p_x + \mu\left(u_{xx} + u_{yy}\right) - \sigma \mathrm{B}^2(\mathrm{t})u, \tag{2}$$

$$\rho\left(\mathrm{v}_t + u\mathrm{v}_x + \mathrm{v}\mathrm{v}_y\right) = -p_y + \mu\left(\mathrm{v}_{xx} + \mathrm{v}_{yy}\right), \tag{3}$$

$$T_t + uT_x + \mathrm{v}T_y = \frac{k}{\rho C_p}\left(T_{xx} + T_{yy}\right) + \tau\left[D_B\left(C_xT_x + C_yT_y\right) + \frac{D_T}{T_m}\left(T_x^2 + T_y^2\right)\right], \tag{4}$$

$$C_t + uC_x + \mathrm{v}C_y = D_B\left(C_{xx} + C_{yy}\right) + \frac{D_T}{T_m}\left(T_{xx} + T_{yy}\right) \tag{5}$$

where (u,v) signifies the velocity components along the x- and y-axis, respectively; σ characterizes the electrical conductivity; ρ is the density of the nanofluid; μ is the dynamic viscosity; D_B is the Brownian motion coefficient; D_T is the thermophoretic diffusion coefficient; C is the nanoparticle concentration; $\tau = \left(\rho c_p\right)_p / \left(\rho c_p\right)_f$, where $\left(\rho c_p\right)_p$ describes the effective heat capacity of the nanoparticles; T is the temperature of the fluid; T_{m} is the mean fluid temperature, and κ is the effective heat capacity.

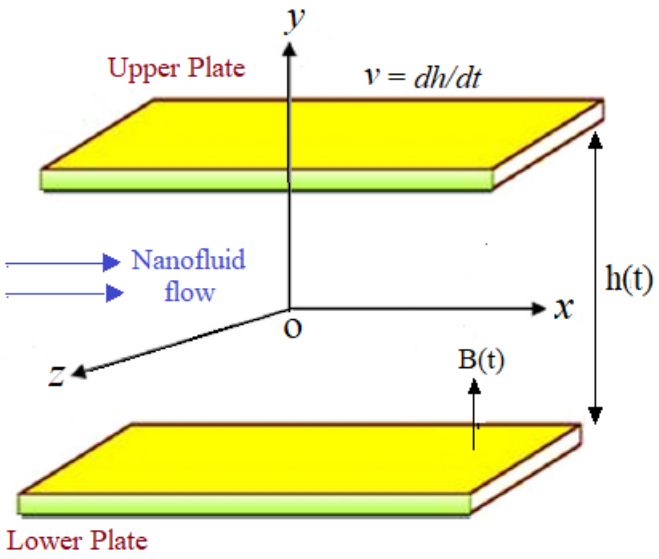

Fig. 1. Geometry of the problem.

The essential boundary conditions for the current study are as follows [11, 12, 24]:

$$\left.\begin{aligned} &u = 0, \mathrm{v} = \frac{dh}{dt},\ T = T_h,\ C = C_h \ \text{at}\ y = h(t) \\ &u = 0,\ \mathrm{v} = 0,\ -\kappa\frac{\partial T}{\partial y} = h_f\left(T_h - T\right),\ -D_m\frac{\partial C}{\partial y} = h_m\left(C_h - C\right) \ \text{at}\ y = 0 \end{aligned}\right\} \tag{6}$$

where T_h and C_h are the temperature and the nanoparticle concentration at the upper plate, respectively. It is assumed that the lower plate is getting hot by means of a hot fluid having temperature T_H and offers the heat transmission coefficient as h_f; D_m stands for the molecular diffusivity of the species concentration; and h_m is the wall mass transfer coefficient.

Using boundary layer approximation and the following similarity transformations:

$$u = \frac{bx}{1-\alpha t} f'(\eta),\ \mathrm{v} = -\sqrt{\frac{b\nu}{1-\alpha t}} f(\eta),\ \theta = \frac{T - T_h}{T_f - T_h},\ \phi = \frac{C - C_h}{C_f - C_h},\ \eta = \sqrt{\frac{b}{\nu(1-\alpha t)}} y \tag{7}$$

equations (1)–(5) reduce to

$$f'''' + ff''' - f' \cdot f'' - \lambda\left(\eta f''' + 3f''\right) - M^2 f'' = 0, \tag{8}$$

$$\theta'' + \Pr(f - \lambda\eta)\theta' + Nb\phi'\theta' + Nt(\theta')^2 = 0 \tag{9}$$

$$\phi'' Nb + LeNb\left(f - \lambda\eta\right)\phi' + Nt\theta'' = 0 \tag{10}$$

with the boundary conditions

$$\left.\begin{array}{l} f(1)=1,\ f'(1)=0,\ \theta(1)=1,\ \phi(1)=0 \\ f(0)=f'(0)=0,\ \theta'(0)=-\beta_1\left(1-\theta(0)\right),\ \phi'(0)=-\beta_2\left(1-\phi(0)\right) \end{array}\right\} \tag{11}$$

Here, $M = HB_0\sqrt{\frac{\sigma}{\mu}}$ is the symbol for Hartmann parameter, $\lambda = \frac{\alpha H^2}{2\nu}$ is the squeeze number, $\beta_1 = \frac{h_f}{\kappa}\sqrt{\frac{\nu}{b}}$ is the thermal Biot number, $\beta_2 = \frac{h_m}{D_m}\sqrt{\frac{\nu}{b}}$ corresponds to the concentration Biot number, $Nt = \frac{\tau D_T\left(T_w - T_h\right)}{\nu T_m}$ represents the thermophoresis parameter, $Nb = \frac{\tau D_B\left(C_w - C_h\right)}{\nu}$ denotes the Brownian motion parameter, $\Pr = \frac{\nu}{\alpha}$ is the Prandtl number, $Le = \frac{\nu}{D_B}$ describes the Lewis number.

The most important characteristics of heat and mass transfer are reduced Nusselt number Nur and reduced Sherwood number Shr, which are defined as follows:

$$Nur = -\theta'(0) \text{ where } Nur = \sqrt{1-\alpha t}\,Nu \tag{12}$$

and

$$Shr = -\phi'(0) \text{ where } Shr = \sqrt{1-\alpha t}\,Sh \tag{13}$$

3. Solution Method

The set of equations (8)–(10) under boundary conditions (11) was solved numerically using a shooting iteration technique together with the Runge–Kutta sixth-order integration scheme. The unspecified primary conditions were assumed and then integrated numerically as an initial valued problem to a given terminal point. Enhancement was made on the values of assumed missing initial conditions by iteratively comparing the calculated value of the dependent variable at the terminal point with its value given there. The computations were performed using a written program based on the symbolic and computational computer language MAPLE.

To ascertain the accuracy of our numerical results, the present study (in absence of thermal radiation) was compared with the study of Muhammad et al. [12]. The values of Nur and Shr were calculated for various Nt values. Excellent agreement was found between these two sets of results, as shown in Table 1. Thus, the use of the present numerical code for the current model was justified.

Table 1. Comparison of *Nur* and *Shr* values for different *Nt* values

N_t	Present work		Muhammad et al. [12]	
	Nur	*Shr*	*Nur*	*Shr*
0.5	2.599805	0.988231	2.5923	0.9901
1.0	1.747822	0.900912	1.7456	0.9020
1.5	1.108564	0.858981	1.1196	0.8615
2.0	1.011226	-	1.0072	-

4. Results and Discussion

To get an insight into the effects of different parameters of practical importance on the flow characteristics, the numerical results are presented graphically in Figs. 2–11 for several sets of values of the pertinent parameters. In the simulation, the following default values of the parameters are considered: Nb = 0.4, Nt = 0.5, β_1 = 0.2, β_2 = 0.15, λ = –0.5, Le = 1.0, M = 0.5, and Pr = 0.7, unless otherwise specified. Figure 2 shows the effect of squeeze number λ on fluid temperature. With an increase in squeeze number λ (absolute value), θ decreases near the boundary layer region. The upshot is perceptible only in a region close to the lower plate, because the curves tend to merge at large distances from the lower plate. It is worth noting that an increase in λ can be associated with a decrease in the kinematic viscosity, an increase in the distance between the plates, and an increase in the velocity at which the plates move. It is observed from Table 2 that an increase in λ (absolute value) results in a decrease in Nur . Thus, the squeeze number λ has a significant effect on heat transfer due to an increased temperature gradient on the lower plate wall. It is evident from Fig. 3 that θ increases with increasing thermal Biot number β_1 in the boundary layer region and it is maximal near the wall region of the lower plate. A stronger convection leads to a higher heat transfer rate and provokes the thermal effect to penetrate deeper into the quiescent fluid, as shown in Table 2. It is also observed that the heat transfer rate at the lower plate increases with increasing β_1 values. It is evident that the thermal Biot number has a strong impact on the heat transfer and enhances it by almost 116% with a change in the thermal Biot number from 0.1 to 0.3. The effects of the parameters controlling the Brownian motion and thermophoresis on temperature distribution are well presented in Figs. 4 and 5 in the presence of surface convection. It is evident from the figures that θ increases in both the Nb and Nt values and the effect is high up to the lower plate region. As both Nb and Nt increase, the thickness of the thermal boundary layer increases, while the curves become less steep near the upper plate region; this fact indicates a decrease in Nur , as evident from Table 2.

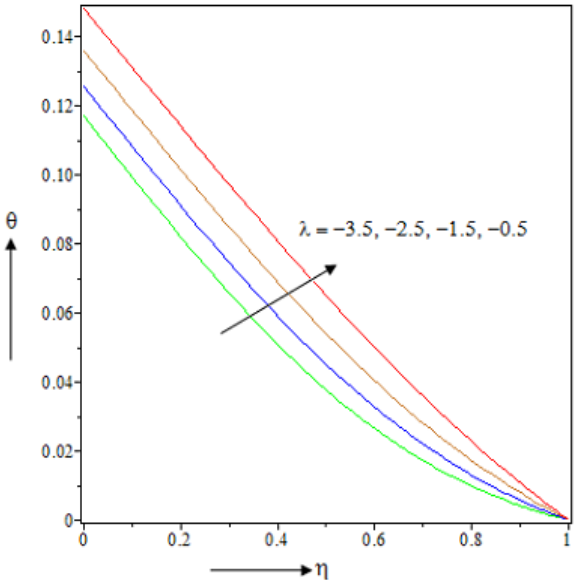

Fig. 2. Concentration profiles for various λ values.

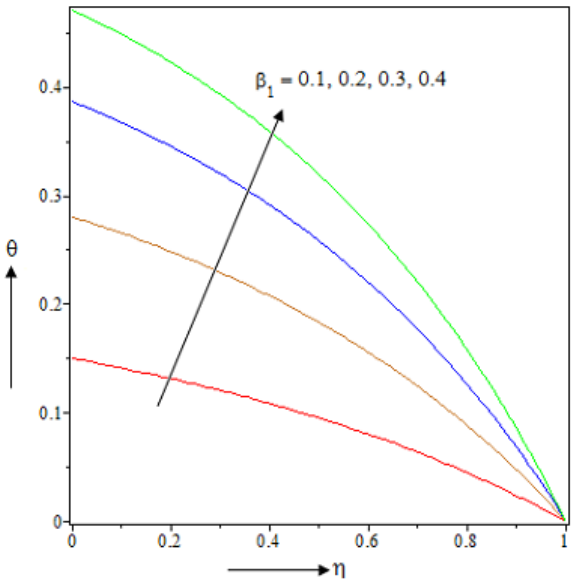

Fig. 3. Concentration profiles for various β_1 values.

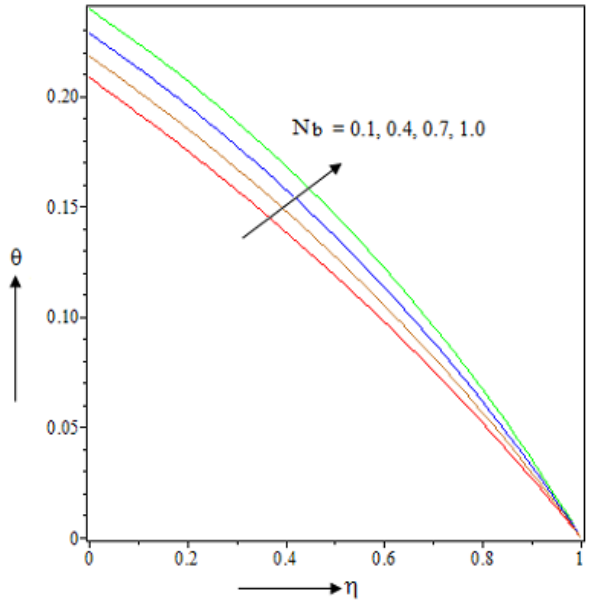

Fig. 4. Concentration profiles for various Nb values.

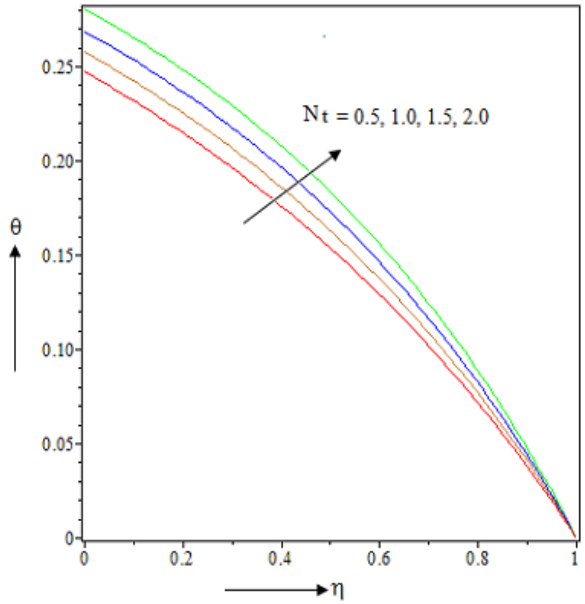

Fig. 5. Concentration profiles for various Nt values.

Table 2. Effects of physical parameters on reduced Nusselt number

Nb	*Nt*	β_1	λ	*Nur*
0.1	0.5	0.2	–0.5	0.15827411
0.4	–	–	–	0.15629526
0.7	–	–	–	0.15420971
0.4	0.5	–	–	0.16107681
–	1.0	–	–	0.15957895
–	1.5	–	–	0.15798790
–	0.5	0.1	–	0.08497693
–	–	0.2	–	0.14385373
–	–	0.3	–	0.18389034
–	–	0.2	–1.0	0.16309775
–	–	–	–1.5	0.16197683
–	–	–	–2.0	0.15886899

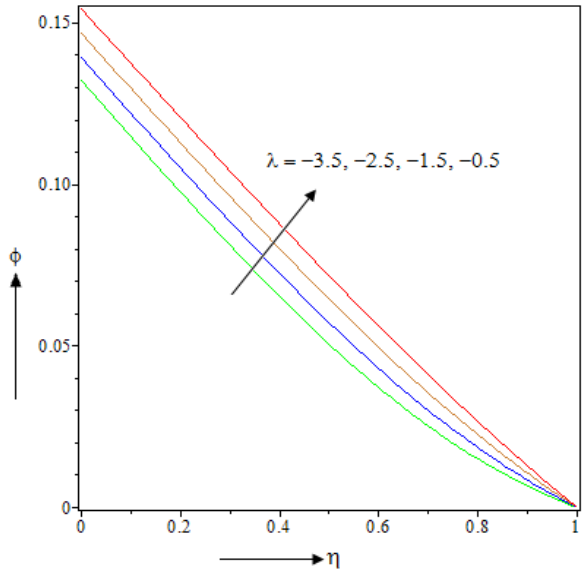

Fig. 6. Concentration profiles for various λ values.

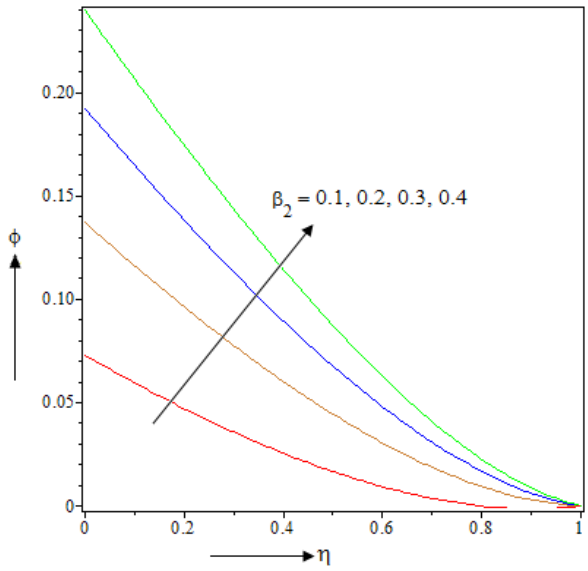

Fig. 7. Concentration profiles for various β_2 values.

With an increase in λ (absolute value), the nanoparticle concentration distribution decreases near the lower plate region, i.e., for η < 0.4 (not precisely determined); after that, it starts decreasing with an increase in η near the upper plate region, as shown in Fig. 6. It is evident from Table 3 that *Shr* decreases with an increase in λ (absolute value) on the lower plate wall in

the presence of surface convection. Figure 7 depicts the variation in the concentration distribution across the boundary layer for different values of concentration Biot number β_2. It is evident that, with an increase in β_2, ϕ significantly increases across the boundary layer near the lower plate. The cause of this trend is that the nanoparticle concentration near the boundary layer becomes wide for larger values of β_2. Further, it follows from Table 3 that Shr increases due to surface convection parameter β_2. Figure 8 reveals that ϕ uniformly increases with increasing Nb values at the squeeze number of $\lambda < 0$. The figure shows that the effect of Nb on the nanoparticle concentration is noticeable only in a region close to the lower plate, as the curves tend to merge at larger distances from the lower plate and, consequently, the concentration boundary layer thickness decreases with increasing Nb. Table 3 shows the effect of Nb on the reduced Sherwood number. It is evident that Shr decreases due to the Brownian motion parameter of nanoparticles. The impact of Nt on ϕ is presented in Fig. 9. It is seen that an increase in the values of the thermophoresis parameter Nt leads to a rapid decrease in the concentration distribution near the lower plate wall region, whereas the concentration decreases gradually from the lower plate region to the upper plate region. It is evident from Table 3 that the thermophoretic effect exerts a strong domination on the mass transfer and enhances it by almost 15.9% with a change in Nt from 0.5 to 1.5.

Table 3. Effect of physical parameters on reduced Sherwood number

Nb	Nt	β_2	λ	Shr
0.1	0.5	0.15	–0.5	0.67302245
0.4	–	–	–	0.43010935
0.7	–	–	–	0.39602982
0.4	0.5	–	–	0.33621418
0.4	1.0	–	–	0.35867916
–	1.5	–	–	0.38970853
–	0.5	0.15	–	0.13297462
-	–	0.25	–	0.20313607
-	–	0.35	–	0.26250404
-	–	0.15	–1.0	0.34039567
-	–	–	–1.5	0.33621418
-	–	–	–2.0	0.33207471

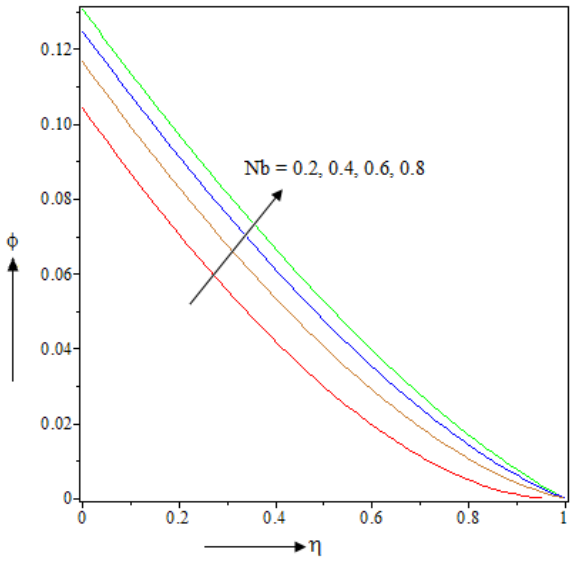

Fig. 8. Concentration profiles for various Nb values.

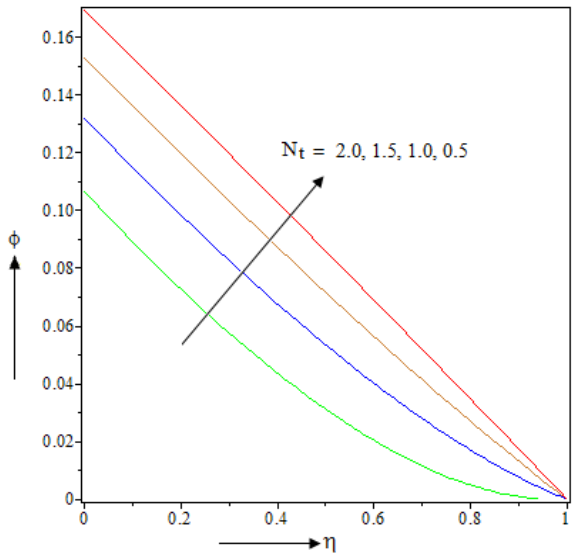

Fig. 9. Concentration profile for various Nt values.

5. Conclusions

In this study, the unsteady squeezing flow in a viscous incompressible electrically conducting nanofluid between two parallel plates is analyzed using a numerical technique. The shooting iteration technique together with the Runge–Kutta sixth-order integration scheme is used to obtain the numerical solution of the nonlinear flow problem. Numerical out-turns are presented through graphs to decorate the details of the heat and mass characteristics and their dependence on material parameters. The use of multiple convective boundary conditions makes the study more general and novel. The results presented here are potentially important for controlling the heat transfer rate and the mass transfer rate. According to the study, some key features are presented as follows:

(i) The Sherwood number at the lower plate decreases with an increase in Brownian motion parameter Nb, squeeze number λ, and Lewis number Le.

(ii) The mass transfer rate vigorously increases due to the occurrence of thermophoresis and surface convection.

(iii) An increase in thermal Biot number β_1 and squeeze number λ leads to an increase in the heat transfer rate at the lower plate.

(iv) It is also observed that, as the Brownian motion intensifies, it affects a larger extent of the fluid and leads to an increase in the thickness of the thermal boundary layer, which in turn decreases the reduced Nusselt number.

Acknowledgments

The authors express their cordial thanks to the respected Editor-in-chief and the honorable reviewer for valuable suggestions and comments to improve the presentation of this manuscript.

References

[1] M.J. Stefan, Abt. II, Österr. Akad. Wiss., Math.-Naturwiss. Kl. 69, 713 (1874).
[2] M. Mahmood, S. Asghar, and M.A. Hossain, Heat Mass Transfer 44, 165 (2007).
[3] M.M. Rashidi, Math. Probl. Eng. 2008, 935095 (2008).
[4] A.M. Siddiqui, S. Irum, and A.R. Ansari, Math. Model. Anal. 13, 565 (2008).
[5] G. Domairry and A. Aziz, Math. Probl. Eng. 2009, 603916 (2009).
[6] T. Haya, A. Yousaf, M. Mustafa, and S. Obaidat, Int. J. Numer. Meth. Fluids 69, 399 (2011).
[7] M. Mustafa, T. Hayat, and S. Obaidat, Meccanica 47, 1581 (2012).
[8] M. Sheikholeslami and D.D. Ganji, Comput. Meth. Appl. Mech. Eng., 283, 651 (2015).
[9] M. Sheikholeslami, D.D. Ganji, and H.R. Ashorynejad, Powder Tech. 239, 259 (2013)..
[10] O. Pourmehran, M. Rahimi-Gorji, M. Gorji-Bandpy, and D.D. Ganji, Alexandria Eng. J. 54, 17 (2015).
[11] N. Acharya, K. Das, and P.K. Kundu, Alexandria Eng. J. 55, 1177 (2016).
[12] S. Muhammad, S.I.A. Shah, G. Ali, M. Ishaq, S.A. Hussain, and H. Ullah, Asian Res. J. Math. 10(1), 1 (2018).
[13] A. Aziz, Commun Nonlinear Sci. Numer. Simul. 14, 1064 (2009)..
[14] O. D. Makinde and A. Aziz, Int. J. Therm. Sci. 49, 1813 (2010).
[15] A. Ishak, Appl. Math. Comput. 217, 837 (2010)..
[16] O.D. Makinde, and A. Aziz, Int. J. Thermal Sci. 50, 1326, (2011)..
[17] A. Aziz and W.A. Khan, Int. J. Therm. Sci. 52, 83 (2012).
[18] K. Das, P.K. Duari, and P.K. Kundu, J. Egypt. Math. Soc. 23(2), 435 (2015)..
[19] M.J. Uddin, O.A. Beg, and I. Md. Ismail, Math. Probl. Eng. 2014, 179172 (2014).
[20] K. Das, N. Acharya, and P.K. Kundu, Appl. Therm. Eng. 103, 38 (2016).
[21] A. Tanveer, T. Hayat, and A. Alsaedi, Neural. Comput. 32(2), 437 (2016).
[22] M.J. Uddin, O.A. Beg, and I. Md. Ismail, Int. J. Numer, Meth. Heat Fluid Flow 26(5), 1526 (2016).
[23] M.J. Uddin, B. Rostami, M.M. Rashid, and P. Rostami, Alexandria Eng. J. 55, 263 (2016).
[24] N. Acharya, K. Das, and P.K. Kundu, Can. J. Phys. 96, 104 (2018).

BROWNIAN ALTERNATOR

J.-S. Rattinacannou

Member of the European Physical Society
180 rue du Centre Aéré, Saint Paul lès Dax, 40990 France
E-mail: jsrtncn@free.fr

(Received July 22, 2019)

Abstract

The two-resonator device and the pillar-array version thereof described in a previous manuscript are the subject of a more precise study. The physical interpretation of the device operation is changed for a more appropriate one. The hypothesis on which the pillar-array version is based is revisited and clearly formulated. The pillar-array device is considered under the aspect of an electric generator. This study leads to a new design for this generator. Another resonator is added in order to increase vibrations. The feasibility of an experimental device is addressed. Instructions for the fabrication of a prototype are given.

1. Introduction

In 2017 in [1], we were mostly focused on thermodynamic considerations; here, we envisage the devices described in Figs. 4 and 7a in [1] only in terms of energy production. The first device is made up of a nanopillar subjected to Brownian motion and coupled with a much bigger pillar, the Resonator (Fig. 1). In the second device, an array of nanopillars is used instead of a single nanopillar, and the Resonator has no longer the shape of a pillar; it is a piezoelectric thin film with two electrodes (Fig. 2). This last device is referred to as "the Brownian alternator" because, from the Brownian motions of nanopillars, it produces a permanent alternating voltage, like an alternating-current generator.

2. Single-Nanopillar Device

In this paper, the nanopillar and the Resonator of the device are described as coupled oscillators, either in a free-standing system (Fig. 3) or on a support (Fig. 4). The free-standing system is first studied in terms of the theory of coupled oscillators, which can be found in textbooks [2–5] on mechanics and radioelectricity (coupled oscillating circuits), under an assumption that there is no dissipation in the two oscillators. The nanopillar is characterized by displacement x_1, mass m, and spring constant k_1. The Resonator is characterized by displacement x_2, mass M, and spring constant k_2. The spring constant of the coupled oscillators is k. It can be found that $k = k_1k_2/k_1+k_2$; however, this value can be ignored in the calculations.

The nanopillar is subjected to Brownian motion, the time history of which looks like a sine wave of varying amplitude and phase yet constant frequency [6–9], with a mean amplitude a_1 given by:

$$a_1 = \left(\frac{k_B T}{k_1} \right)^{\frac{1}{2}}, \tag{1}$$

where k_B is the Boltzmann's constant and T is the absolute temperature.

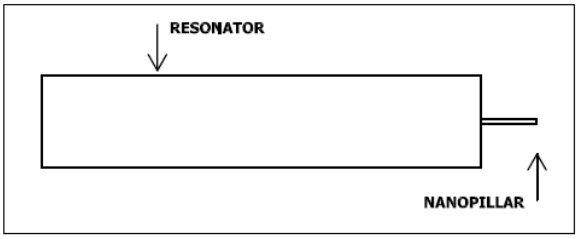

Fig. 1. Single-nanopillar device.

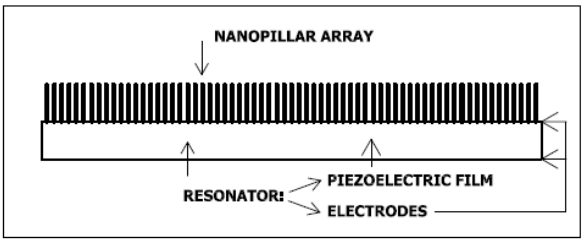

Fig. 2. Brownian alternator.

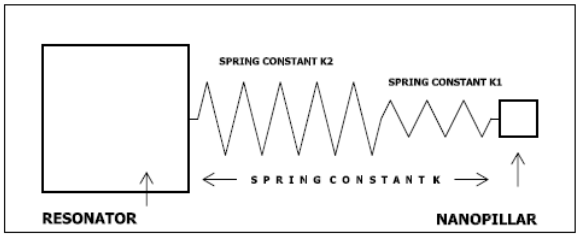

Fig. 3. Free-standing coupled oscillators.

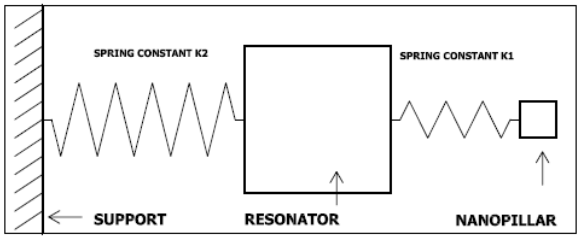

Fig. 4. Coupled oscillators on a support.

If the Resonator is at rest with $x_2=0$, the equation of motion of the nanopillar will be as follows (t is the time):

$$m\frac{d^2x_1}{dt^2} + kx_1 = 0, \text{ with the nanopillar resonant frequency } \omega_1 \text{ given by } \omega_1^2 = \frac{k}{m}, \tag{2; 3}$$

If the nanopillar is at rest with $x_1=0$, the equation of motion of the Resonator will be as follows:

$$M\frac{d^2x_2}{dt^2} + kx_2 = 0, \text{ with the Resonator's resonant frequency } \omega_2 \text{ given by } \omega_2^2 = \frac{k}{M}, \tag{4; 5}$$

The two equations of motion of the system of coupled oscillators are as follows:
for the nanopillar:

$$m\frac{d^2x_1}{dt^2} + kx_1 = kx_2, \text{ or using Eq. (3): } \frac{1}{\omega_1^2}\frac{d^2x_1}{dt^2} + x_1 = x_2, \tag{6; 7}$$

for the Resonator:

$$M\frac{d^2x_2}{dt^2} + kx_2 = kx_1, \text{ or using Eq. (5): } \frac{1}{\omega_2^2}\frac{d^2x_2}{dt^2} + x_2 = x_1, \tag{8; 9}$$

For the nanopillar Brownian motion, the model of a sinusoidal oscillation of amplitude a_1 is taken as follows:

$$x_1 = a_1 \cos\omega t, \text{ and therefore: } \frac{d^2x_1}{dt^2} = -a_1\omega^2 \cos\omega t, \tag{10; 11}$$

where ω is the angular frequency. Inserting the values of Eqs. (10) and (11) into Eq. (7), we obtain:

$$x_2 = \left(1 - \frac{\omega^2}{\omega_1^2}\right) a_1 \cos \omega t \text{ , and therefore: } \frac{d^2 x_2}{dt^2} = -\left(1 - \frac{\omega^2}{\omega_1^2}\right) a_1 \omega^2 \cos \omega t \,. \qquad (12; 13)$$

Thus, the Resonator vibrates in phase or in phase opposition (depending on $\omega^2/\omega_1{}^2$) with respect to the nanopillar with an amplitude a_2 given by:

$$a_2 = \left(1 - \frac{\omega^2}{\omega_1^2}\right) a_1 \,, \qquad (14)$$

Inserting the values of Eqs. (12) and (13) into Eq. (9), we obtain:

$$\left[1 + \left(1 - \frac{\omega^2}{\omega_1^2}\right)\frac{\omega^2}{\omega_2^2} - \left(1 - \frac{\omega^2}{\omega_1^2}\right)\right] a_1 \cos \omega t = 0 \,, \qquad (15)$$

This equation implies that:

$$\omega^4 - \omega^2\left(\omega_1^2 + \omega_2^2\right) = 0 \,, \qquad (16)$$

which has two solutions ω' and ω'':

$$\omega'^2 = 0 \text{ , and: } \omega''^2 = \omega_1^2 + \omega_2^2 \,, \qquad (17; 18)$$

The nanopillar and the Resonator oscillate in phase opposition at frequency ω''. If both oscillators have the same resonant angular frequency ($\omega_2 = \omega_1$), that of the system is given by:

$$\omega'' = \omega_1 \sqrt{2} \,, \qquad (19)$$

From Eqs. (3) and (5), the Resonator vibration amplitude a_2 is as follows:

$$a_2 = \left(1 - \frac{\omega_1^2 + \omega_2^2}{\omega_1^2}\right) a_1 = -\frac{m}{M} a_1 \,, \qquad (20)$$

For the second system (coupled oscillators, both of resonant angular frequency ω_1', on a support), the equations of motion are as follows:
for the nanopillar:

$$m \frac{d^2 x_1}{dt^2} + k_1 x_1 = k_1 x_2 \,, \qquad (21)$$

for the Resonator:

$$M \frac{d^2 x_2}{dt^2} + \left(k_1 + k_2\right) x_2 = k_1 x_1 \,. \qquad (22)$$

Similar to the free-standing system, the calculations show that the Resonator vibration amplitude is exactly like that given by Eq. (20) with two solutions for the frequency of the coupled system:

$$\omega'^2 = \omega_1'^2 \left(1 - \frac{m}{M}\right), \text{ (in-phase oscillations)} \qquad (23)$$

$$\omega''^2 = \omega_1'^2 \left(1 + \frac{m}{M}\right), \text{ (phase-opposition oscillations)} \qquad (24)$$

with ω_1' given by:

$$\omega_1'^2 = \frac{k_1}{m} = \frac{k_1 + k_2}{M} \,, \qquad (25)$$

In the conclusion of Section 2, it is shown that, in terms of the model of coupled oscillators, the amplitude of the Resonator vibration is considerably smaller than that of the nanopillar. The vibration energy of the Resonator is also extremely low; therefore, it should be noted that there is no decrease in entropy in the single-pillar device studied in [1], contrary to what was written in that paper.

However, Eq. (20) allows us to catch sight of what should be done in order to get energy from Brownian motion. This is the subject of the next section.

3. Brownian Alternator

3.1. Design of the Brownian alternator

As noted in the Introduction, the "Brownian alternator" refers to a nanopillar-array device. The result of Eq. (20) indicates that the solution, to provide a large amplitude a_2 and then extract useful work from Brownian motion, is that the second oscillator should have the same mass as the first one.

For the Brownian alternator, this means that each nanopillar of the array should act on an extremely small part of the Resonator. This part should have the same mass as that of the nanopillar, so the shape of the Resonator has to be modified. Instead of a large pillar (see Fig. 6 in [1]), it takes the form of a thin film, the thickness of which is equal to the length of the nanopillars.

If this thin film were (in imagination) "cut" in small parts of the size of a nanopillar, this latter being only involved in the part facing itself, by gathering and "sticking" all these parts together, the uncut Resonator would vibrate as a whole at the nanopillar amplitude, with the essential condition being that the nanopillars vibrate in phase. This is the main condition for the device operation.

In the array, the nanopillars should be tightly packed by designing, for instance, hexagonal sections for the nanopillars with a narrow spacing between them.

In addition to the single-array design, the solution (Eqs. (21)–(25)) for the second system (coupled oscillators on a support) suggests another design (Fig. 5), where two devices are joined, each one acting as a support for the other one.

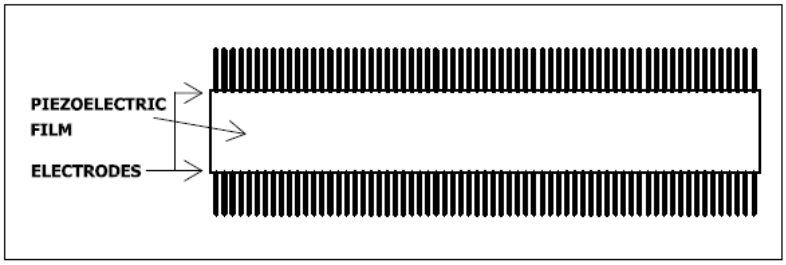

Fig. 5. Double-array Brownian alternator.

3.2. Operation principle

The following operation principle of the Brownian alternator is proposed: the Resonator has a much more regular vibration than that of the nanopillars subjected to the disorder, in amplitude and phase, of thermal agitation. However, the basis of coupling between oscillators is

that they act on each other: each nanopillar of the array keeps the Resonator vibration going, and the Resonator acts on each nanopillar: if there is any out-of-phase nanopillar in the array, the coupling with the Resonator makes it come back to the in-phase state: the Resonator, because of vibrating as a whole, maintains the nanopillars of the array in phase (for starting the pillar in-phase motion see [1]).

To date, calculations and deductions have been made under the theoretical assumption of no dissipation in the Resonator. Now, in the actual case of dissipation, the Resonator amplitude can be smaller than that of the nanopillars; however, if dissipation is not too high, the two amplitudes are close to each other. The condition that the Brownian alternator also operates with low dissipation in the Resonator is still part of the previous proposition. This proposition explains how the condition of in-phase nanopillars of Section 3.1 could be fulfilled, and is nothing but a supposition. Therefore, the following hypothesis should be formulated.

3.3. Fundamental hypothesis

The working of the Brownian alternator relies on the following.

In the steady state of the system of coupled oscillators comprising an array of nanopillars subjected to Brownian motion and the underdamped Resonator, with the amplitude of the Resonator close to that of the nanopillars, we make the fundamental hypothesis that the Resonator maintains one single phase in the nanopillar Brownian motions.

These in-phase Brownian motions were referred to as “coherent Brownian motion” elsewhere [10].

3.4. Increased voltage with a resonant circuit

There are not many electric charges which appear at the electrodes of the piezoelectric film, because the vibration amplitude of the Resonator does not exceed that of the nanopillars. In order to get an increased amplitude, another resonator should be added to the Brownian alternator. This resonator is a resonant circuit connected to the electrodes, and the increased amplitude is that of a voltage, rather than of a mechanical vibration. The voltage inside the resonant circuit is considerably enhanced compared with that of the electrodes. The enhanced voltage makes the produced energy easier to use. Because of the size of the nanopillars, both the vibration of the piezoelectric film and the oscillation of the electric charges belong to the hyperfrequency range, and the resonant circuit would be rather a resonant cavity.

4. Experimental Device

The main part of the device is a piezoelectric film, which should have low losses and withstand hyperfrequency use in the 10 to 100 GHz range, depending on the nanopillar length. An array of nanopillars could be etched either in a thin film of any suitable material or directly on one of the two electrodes of the piezoelectric film [11–13]. Nanopillars with a hexagonal section, aspect ratio (length/diameter) of about 10, and a narrow spacing can be prepared by any technique providing smooth surfaces and accurate dimensions, for instance, by RIE or ICP [14]. The different thin layers constituting the device are as follows: the bottom electrode, the piezoelectric film, the top electrode, the nanopillar array. They could be deposited on a sacrificial layer, which can be easily removed to make the device free-standing, linked by electric connections to a support. The thickness of the layers should be determined by taking into account the wavelength of the frequency under consideration for each layer. The feasibility of the device

does not present any insurmountable difficulty; it is within the reach of the present technology. Another issue is the hyperfrequency part of the device. It is a case for hyperfrequency physicists to carefully design the circuit to be connected to the electrodes of the Brownian alternator.

5. Discussion and Conclusion

Nanopillars driven by thermal agitation can be taken as sustained oscillators coupled with an underdamped oscillator, the Resonator. In this particular case, each nanopillar can be seen as having a negative mechanical resistance r_1, which cancels a small part of the positive mechanical resistance r_2 of the Resonator. If there are n nanopillars in the array, the effect of n negative r_1 is to cancel a large part or even the totality of r_2 [15]. In this last case, the Resonator amplitude $|a_2|$ equals the nanopillar amplitude $|a_1|$. It is evident that, in this system, the amplitude of the underdamped oscillator is dependent not only on r_2, but also on n and r_1.

The question is now arising, whether the n negative r_1 are able to cancel r_2, that is, which resistance of the Resonator the Brownian motions of the nanopillar array can cancel. This question is possibly related to the following one: how much time does it take, starting from amplitude zero, for thermal agitation to "refuel" nanopillar Brownian motion, that is, to reach the mean amplitude of Brownian motion? We suppose that this time is extremely short, possibly on the order of one period. These two questions could be the subject of a future paper.

In conclusion, we would like to underline that this paper on the Brownian alternator is far from being complete. It should be regarded as a contribution to the study of systems where nanosize elements (pillars) are in interaction with a macroscopic size component (Resonator). Within the framework of coupled oscillators we have shown that, although the single-pillar device does not supply any energy, useful work could be produced by the Brownian alternator, provided that the fundamental hypothesis is met. This hypothesis is worth testing with an experimental device. Current technology is able to produce high-quality piezoelectric thin films and high-aspect-ratio nanopillars, so that it would not be too difficult to build prototypes of the Brownian alternator.

References

[1] J.-S. Rattinacannou, Mold. J. Phys. Sci. 16, 101 (2017).
[2] G. Bruhat, Mécanique, 5th ed., Masson, Paris, 1955.
[3] F. S. Tse, I. E. Morse, and R.T. Hinkle, Mechanical Vibrations, 2nd ed., Allyn and Bacon, Inc., Boston, MA, 1978.
[4] M.P. Norton and D. G. Karczub, Fundamentals of Noise and Vibration Analysis for Engineers, 2nd ed., Cambridge University Press, New-York, 2003.
[5] F. Langford-Smith, Radiotron Designer's Handbook, 4th ed., RCA, Harrison, NJ, 1957.
[6] V. B. Braginsky and A. B. Manukin, Measurement of Weak Forces in Physics Experiments, University of Chicago Press, Chicago, 1977.
[7] P. R. Saulson, Phys. Rev. D, 42, 2437 (1990). doi: 10.1103/PhysRevD.42.2437.
[8] G. I. González and P. R. Saulson, Phys. Lett. A 201, 12 (1995).
[9] González G. I., Brownian Motion of a Torsion Pendulum Damped by Internal Friction, Ph.D. thesis, Syracuse University, Syracuse, NY, 1995.
[10] page 113 in [1], Ref. [17].
[11] Y.-F. Chang, Q.-R. Chou, J.-Y. Lin, and C.-H. Lee, Appl. Phys. A 86, 193 (2007).
[12] K. J. Morton, G. Nieberg, S. Bai, and S. Y. Chou, Nanotechnology 19, 345301 (2008).

[13] M. D. Henry, ICP Etching of Silicon for Micro and Nanoscale Devices, Ph.D. Thesis, Caltech, CA, 2010.
[14] T. Lill and O. Joubert, Science 319, 1050 (2008).
[15] page 432 in [2].

AN UNINTERRUPTIBLE POWER SYSTEM CONTAINING A BRIDGE INVERTER COMBINED WITH A BATTERY CHARGING UNIT

Iu. Sainsus, A. Conev, Iu. Russev, and A. Sidorenko

Ghitu Institute of Electronic Engineering and Nanotechnologies, Academiei str. 3/3, Chisinau, MD-2028 Republic of Moldova,
E-mail: yenergy@mail.ru

(Received July 3, 2019)

Abstract

Uninterruptible power systems (UPSs) have been commonly used for powering computers and for continuous technological processes in various branches of industry and medicine [1]. The lives of people and the safety of large streams of information depend on the reliability of operation of UPSs. Regardless of the topology of implementation of UPSs, they contain batteries that should be recharged. In most cases, separate assembly units are used; they increase the cost of the devices and decrease their reliability. This paper describes a method for charging the battery without changing the circuit in cases where a bridge circuit is used in the inverter part.

1. Introduction

The developed device can be used in the field of powered electrical engineering, namely, single-phase bridge transistor inverters used in various uninterruptible power systems (UPSs). The technical problem that can be solved by means of this device is the simplification of the battery charging circuit owing to a variation in the control pulses as indicated in Fig. 1. The two included lower power switches, together with the secondary winding of the power transformer, accumulate the energy received from the network in the form of a magnetic field, which subsequently, during the locked state of these power switches, is released in the form of a current flowing alternately through their free-wheeling diodes. This current charges the battery during both half-periods of the mains voltage.

The use of microprocessors made it possible to develop a simple and still efficient control circuit for all four power switches.

The novelty is that the original circuit of the bridge inverter is not changed, and the technical result is achieved owing to the introduction of an additional algorithm of operation of the power switch control circuit, while the UPS containing a bridge inverter combined with a battery charging unit is connected to the industrial network. Figure 1 shows a well-known single-ended flyback step-up inverter.

It is evident from Fig. 1 that, with the closed switch *K*, energy accumulates in inductor *L*1 by loop current *I*1, which, after closing switch *K*, continues as loop current *I*2, which charges battery *Acc* via diode *VD*.

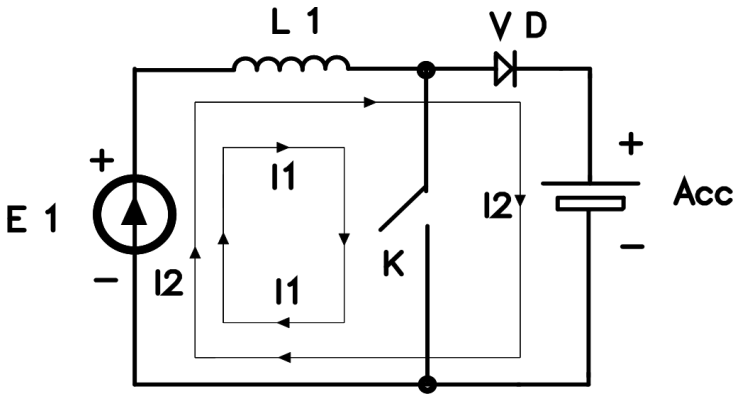

Fig. 1. Circuit and current flow in a single-ended flyback step-up inverter.

If we assume that, in Figs. 3 and 4, the two lower power switches of the bridge inverter *Q*3 and *Q*4 form switch *K* and the secondary winding *W*2 of the power transformer forms inductor *L*1 and if we replace current source *E*1 with the induced voltage in the secondary winding of the power transformer cut into mains, then, by changing the control signals as shown in Fig. 2, it is possible to form a circuit of a single-ended flyback step-up inverter from the bridge circuit of a two-stroke inverter. The control pulses applied to the input of the power switches are represented by the oscillograms shown in Fig. 2.

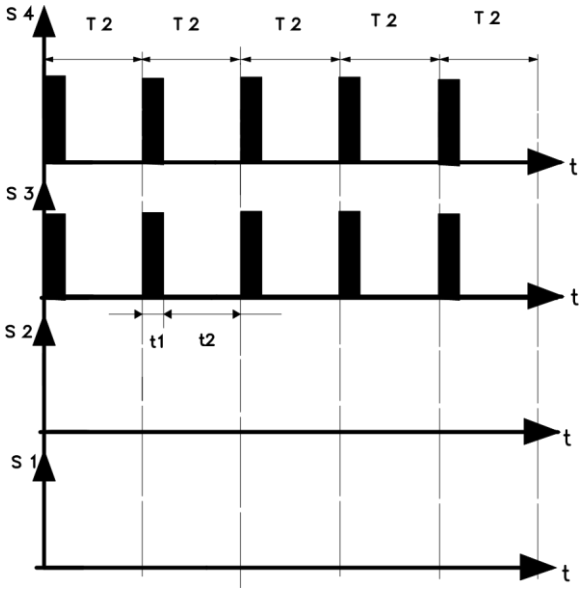

Fig. 2. Oscillograms of signals supplied to the input of the power switches.

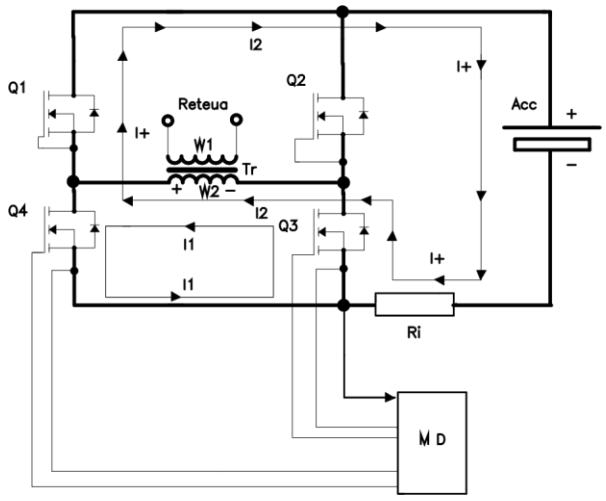

Fig. 3. Passage of the charging current during the positive half-wave of the mains voltage.

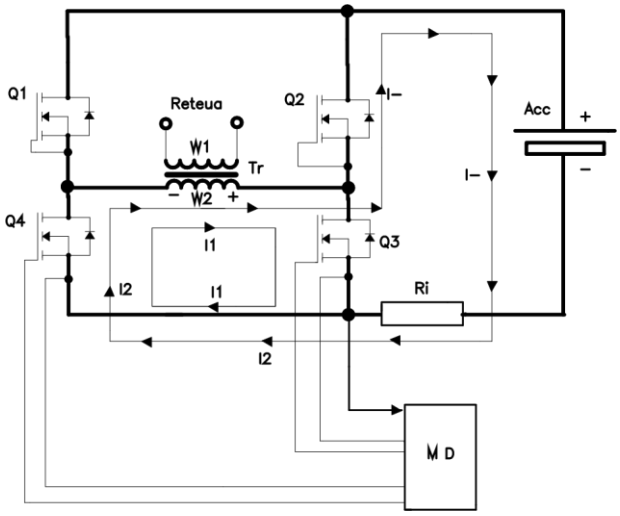

Fig. 4. Passage of the charging current during the negative half-wave of the mains voltage.

The passage of the charging currents during the positive and negative half-waves of the mains voltage is shown in Figs. 3 and 4, respectively. Currents *I*1 and *I*2 correspond to time periods *t*1 and *t*2 in Fig. 2.

An UPS containing a bridge inverter combined with a battery charging unit is shown in Fig. 5.

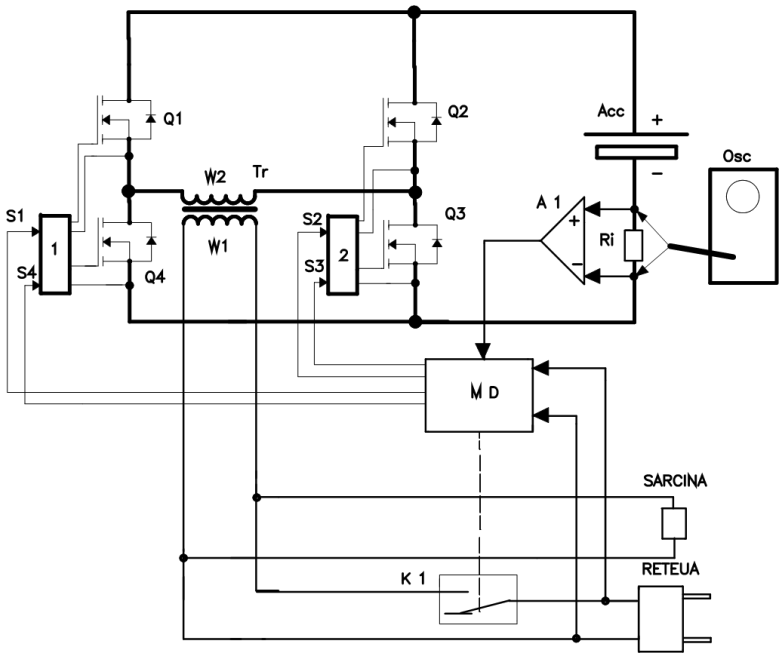

Fig. 5. UPS containing a bridge inverter combined with a battery charging unit.

Here, *1* and *2* are drivers; *Q*1, *Q*2, *Q*3, and *Q*4 are power switches; *Tr* is a power transformer; *W*1 is the primary winding of the power transformer; *W*2 is the secondary winding of the power transformer; *Acc* is a battery; *Ri* is a current sensor; *A*1 is a direct current amplifier; *Osc* is an oscillograph; *S*1, *S*2, *S*3, and *S*4 are signals at the input of the power switches; *MD* is a control unit; *K*1 is a relay; SARCINA is load; and RETEUA is network.

The UPS containing a bridge inverter combined with a battery charging unit, which is shown in Fig. 5, operates as follows: if the mains voltage is below or above the set values, control unit *MD* analyzes it and preserves the position of relay *K*1 as indicated in the circuit; in addition, it generates control signals *S*1, *S*2, *S*3, and *S*4 at regular intervals of 10 ms; the signals activate power switches *Q*1, *Q*2, *Q*3, and *Q*4 and generate heteropolar current pulses on secondary winding *W*2 of power transformer *Tr*; the pulses are induced in primary winding *W*1 of power transformer *Tr* connected to load SARCINA. If the mains voltage lies within the specified limits, control unit *MD* analyzes it and switches the relay to the upper position according to the circuit and simultaneously changes control signals *S*1, *S*2, *S*3, and *S*4 as shown in Fig. 2; the mains voltage is simultaneously supplied to load SARCINA and primary winding *W*1 of power transformer *Tr*; as a result, a heteropolar current is induced on secondary winding *W*2 of power transformer *Tr* at regular intervals of 10 ms; every 50 μs, the current is closed for a short time by power switches *Q*4 and *Q*3, and the power transformer accumulates energy in the form of a magnetic field. After switching off power switches *Q*4 and *Q*3, this energy is released in the form of current pulses, which flow through the free-wheeling diodes of locked power switches *Q*1 or *Q*2 and charge the battery with a current whose strength depends on the duration of the opening pulses and is set by control unit *MD* according to the voltage across current sensor *Ri*.

2. Experimental

A 500-W prototype model of this UPS was assembled. An ATMEGA 8 microprocessor was used in control unit *MD*; a special program was developed for this microprocessor. Power transformer *Tr* was wound on an S-shaped transformer iron frame of the EI133 type; IRF2804 field-effect transistors were used as the power switches; IR2011 drivers and a GP12200 battery (CSB, China) were used. The maximum (ultimate) charging current was selected to be *Imax* = 3A; to increase the efficiency of the device, the ohmic resistance of the current sensor was low (*Ri* = 0.001 Ω); a low-noise direct current amplifier *A*1 (K_{am} = 1000) was introduced. At variations in the mains voltage from 180 to 250 V, the charging current oscillation was no more than $\Delta I = \pm 0.15$A.

The shape of the charging current observed on oscillograph *Osc* (see Fig. 5) connected in parallel to current sensor *Ri* is shown in Fig. 6.

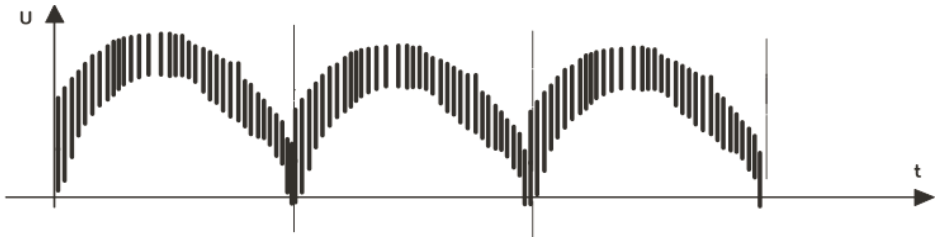

Fig. 6. Charging current oscillogram.

The physical form of the prototype model is shown in Fig. 7.

Fig. 7. Physical form of the prototype model of an UPS containing a bridge inverter combined with a battery charging unit.

According to the results of the work, an application for an invention was submitted [2].

3. Conclusions

This design has been tested in real time and proved to be very reliable. The long-term tests have shown that the simplicity of the design does not interfere with the reliable operation of the inverter circuit and charging the battery. The level of interference generated in the network during the battery charging is easily suppressed by a simple filter and does not exceed the maximum allowed.

The temperature of all the power elements and the power transformer during the tests was 10–15°C above the ambient temperature. This finding suggests that the system will reliably operate in the future.

References

[1] M.A. Shustov, Prakticheskaya skhemotekhnika. Preobrazovateli napryazheniya, Altex, Moscow, book 3, 2002.

http://publ.lib.ru/ARCHIVES/P/"Prakticheskaya_shemotehnika"/_"Prakticheskaya_shemotehnika".html

[2] Iu. Sainsus, A. Conev, Iu. Russev, and A. Sidorenko, MD Short-Term Patent no. 1822 (2016).

A HIGHLY EFFICIENT BRIDGE INVERTER WITH DOUBLED OUTPUT VOLTAGE

Iu. Sainsus, A. Conev, Iu. Russev, and A. Sidorenko

Ghitu Institute of Electronic Engineering and Nanotechnologies, Academiei str. 3/3, Chisinau, MD-2028 Republic of Moldova
E-mail: yenergy@mail.ru

(Received June 20, 2019)

Abstract

A common problem in equipping cars, buses, and other vehicles is the incompatibility of household appliances (coffee makers, converters, radio-receiving sets, audio amplifiers, etc.) that are powered by a constant current with a nominal voltage of 12 or 24 V, which differs from the vehicle's onboard voltage. This problem can be solved by using inverters that provide a twofold decrease or a twofold increase in the output voltage with minimal losses [1]. In this paper, a circuit of this highly efficient inverter is proposed.

1. Introduction

The impetus for designing the proposed inverter was the task of developing a powerful and still cost-effective adapter for powering the equipment with an input supply voltage of +/–24 V, while the vehicle in which this equipment was used had an onboard voltage of +/–12 V. Preliminary prototyping with circuits containing a double-wound transformer and circuits with high-frequency boost did not give the desired results because of high heat losses. The primary winding of the transformer connected to the diagonal of a power bridge composed of four field-effect transistors was initially designed for an AC voltage of 12 V, while all the field-effect transistors were excited by means of two standard drivers.

2. Experimental

The solution of the problem, as shown in Fig. 1, consisted in the replacement of one primary winding designed for a voltage of 12 V by two series-connected center-tapped windings, while the secondary winding of the power transformer was eliminated; in other respects, the circuit remained unchanged. The terminals to which a source voltage of +/–12 V was applied were replaced by the center tap of the primary winding and the sources of the lower power switches, rather than by the drains and sources of the power transistors, as was the case with the secondary circuit. The synchronous operation of the power switches located diagonally in the bridge made it possible to construct a push–pull inverter from two windings of the power transformer and two lower power switches of the bridge; in this case, the two upper power switches of the power bridge act as a synchronous rectifier, in which the drain voltage is two times higher than the input voltage. Taking into account the low ohmic resistance of the field effect transistors (0.002 Ω for IRF2804), the heat losses were extremely small. Figure 1 shows the circuit of this inverter.

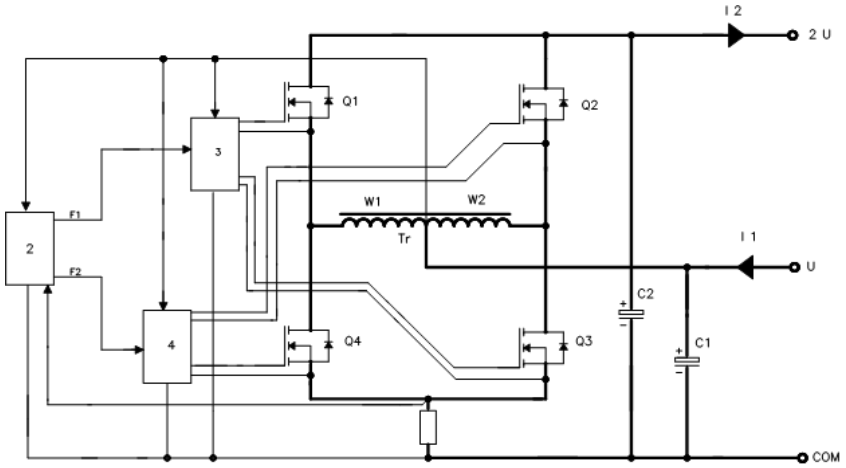

Fig. 1. Circuit of a highly efficient inverter with doubled output voltage.

Here, *2* is a pulse generator based on the KA3525 microcircuit (F = 400 Hz); *3* is a driver based on the IR2011 microcircuit; *4* is a driver based on the IR2011 microcircuit; *C*1 is an input capacitor 3 × 22000 µF/16V; *C*2 is an output capacitor 2 × 10000 µF/35V; *Q*1, *Q*2, *Q*3, and *Q*4 are field-effect transistors of the bridge IR2804 (*Z* = 0.002 E); *Tr* is a power transformer; *W*1 and *W*2 are the windings of the power transformer *S* = 20 mm²; COM is a common bus; *U* is the input voltage bus of 12 V; and 2*U* is the output voltage bus of 24 V.

3. Results and Discussion

To determine the parameters and efficiency of the inverter, respective measurements were conducted. The results are as follows:

— voltage across terminal «*U*» is 12.77 V;
— voltage across terminal «2*U*» is 24.01 V;
— «*I*1» current is 61.2 A;
— «*I*2» current is 34.5 A.

The calculated efficiency is as follows:

$$\mu 1 = (12.77\ \text{V} \times 61.2\ \text{A})/(24.01\ \text{V} \times 34.5\ \text{A}) = 0.943\ (94.3\%).$$

At a laboratory temperature of +21°C, measurements of the temperatures of the different parts of the inverter gave the following results: the temperature of the field-effect transistor heat sink (60 × 40 × 2 mm) is 43.6°C, the temperature of the power transformer core is 39.2°C, and the temperature of the power winding is 54.6°C. The ideas embedded in this design were described in the application for an invention [2].

Figure 2 shows the physical form of the inverter. It is mounted in a rectangular metal casing, without using forced ventilation methods.

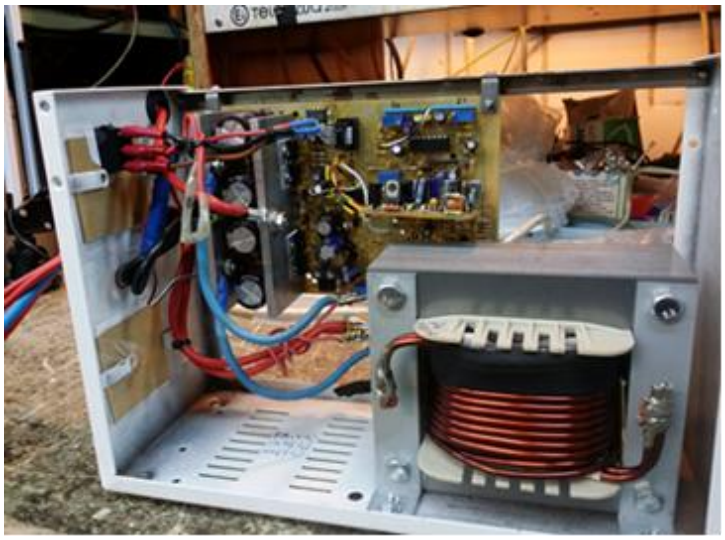

Fig. 2. Physical form of the inverter.

4. Conclusions

The results obtained during the tests suggest a high efficiency of the inverter. The operating temperature of the transformer and power elements makes it possible to predict the high reliability of the inverter over time.

References

[1] M.A. Shustov, Prakticheskaya skhemotekhnika. Preobrazovateli napryazheniya, Altex, Moscow, book 3, 2002.
http://publ.lib.ru/ARCHIVES/P/"Prakticheskaya_shemotehnika"/_"Prakticheskaya_shemotehnika".html

[2] Iu. Sainsus, A. Conev, Iu. Russev, and A. Sidorenko, MD Short-Term Patent no. 1797 (2018).

INVARIANTS OF ENERGY CHARACTERISTICS OF TWO-PORTS WITH VARIABLE LOADS

A. Penin and A. Sidorenko

Ghitu Institute of Electronic Engineering and Nanotechnologies,
Academiei str.3/3, Chisinau, MD-2028 Republic of Moldova
E-mails: aapenin@mail.ru, anatoli.sidorenko@kit.edu

(Received July 22, 2019)

Abstract

Energy characteristics as the load power and efficiency via the load resistance are the well-known two-valued cubic curves. The consideration of these quadratic fractional expressions as geometric projective transformations makes it possible to introduce the cross ratio of four points in limited single-valued working areas. The cross ratio is accepted as the regime parameter in a relative form, which is invariant to a type of the actual regime parameters and circuit sections. The form of expressions for the actual parameter changes depends on the actual regime type. Changes in regime parameters are proved; direct formulas of recalculation are proposed.

1. Introduction

Expressions for different branches of a circuit have a typical homographic or fractionally linear view for currents and resistances [1, 2], which gives solid grounds for consideration of these fractionally linear expressions as a projective transformation of projective geometry and a common use of this method [3–6].

The projective transformations preserve a cross ratio (double proportion) of four samples (values) of the variable resistance and respective currents and voltages. It is convenient to use typical regime values, which can be easily determined at a qualitative level, as the three respective samples; that is, a short circuit, an open circuit, and so on. In turn, the running regime value is the fourth sample. Therefore, the cross ratio is accepted as the regime parameter in a relative form, which is invariant to a type of the actual regime parameters and circuit sections, for example, the input–output of two-port. Hence, obvious changes in regime parameters in the form of increments are formal and do not represent the substantial aspect of the mutual influences: resistance → current.

Next, the invariant properties of two-ports allow transmitting measuring signals, using even the joint or combined wire line for communication and power supply. The cross ratio value does not depend on two-port (wire line) parameters, accuracy of measuring devices, because measuring errors of the currents mutually are reduced. In addition, the cross ratio method allows increasing the accuracy of measuring instruments with a linear-fractional scale [7, 8].

In addition to the above fractionally linear expressions, there are quadratic fractional expressions for some parameters of a circuit. For example, regulated voltage converters with limited voltage source power have two-valued regulation or stabilization characteristics as cubic curves. It was

found that the cross ratio takes place in a limited unambiguous or single-valued working area of these characteristics.

In addition, some important energy characteristics of two-ports, such as the load power and efficiency via the load resistance, are similar cubic curves. In this paper, the above-mentioned results are developed for determining these energy characteristics.

2. Typical Points on Plots of Power Load Characteristics: Choice of a Single-Valued Limited Working Area

Let us consider a two-port with a variable load shown in Fig. 1.

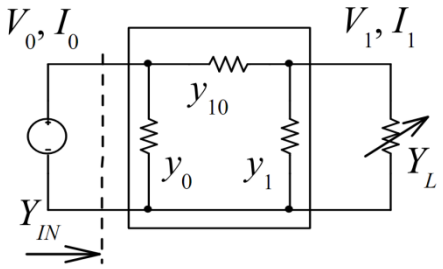

Fig. 1. Two-port with a variable load.

It is known [1, 2], that the system of equation of this two-port is as follows:

$$\begin{bmatrix} I_1 \\ I_0 \end{bmatrix} = \begin{bmatrix} -Y_{11} & Y_{10} \\ -Y_{10} & Y_{00} \end{bmatrix} \cdot \begin{bmatrix} V_1 \\ V_0 \end{bmatrix},$$

where Y parameters $Y_{00} = y_{10} + y_0$, $Y_{11} = y_{10} + y_1$, $Y_{10} = y_{10}$. The determinant of Y matrix $\Delta_Y = Y_{00}Y_{11} - (Y_{10})^2$.

Next, we use the equation of this two-port by the transmission a parameters

$$\begin{bmatrix} V_0 \\ I_0 \end{bmatrix} = \begin{bmatrix} a_{11} & a_{12} \\ a_{21} & a_{22} \end{bmatrix} \cdot \begin{bmatrix} V_1 \\ I_1 \end{bmatrix} = \frac{1}{Y_{10}} \begin{bmatrix} Y_{11} & 1 \\ \Delta_Y & Y_{00} \end{bmatrix} \cdot \begin{bmatrix} V_1 \\ I_1 \end{bmatrix}. \tag{1}$$

In turn, the admittance transformation $Y_{IN}(Y_L)$ has the following fractionally linear form:

$$Y_{IN} = \frac{I_0}{V_0} = \frac{a_{22}Y_L + a_{21}}{a_{12}Y_L + a_{11}}. \tag{2}$$

The determinant of a matrix $\Delta_A = a_{11}a_{22} - a_{12}a_{22} = 1$.

This feature of a parameters allows introducing the hyperbolic functions

$$ch^2\gamma = \frac{Y_{00}Y_{11}}{Y_{10}^2},\ sh^2\gamma = \frac{\Delta_Y}{Y_{10}^2}, \tag{3}$$

where γ is an attenuation coefficient.
Then, equation (1) can be written as

$$\begin{bmatrix} V_0 \\ \dfrac{I_0}{Y_{IN}^{CR}} \end{bmatrix} = \begin{bmatrix} ch\gamma & sh\gamma \\ sh\gamma & ch\gamma \end{bmatrix} \cdot \begin{bmatrix} V_1 \dfrac{Y_L^{CR}}{\sqrt{\Delta_Y}} \\ \dfrac{I_1}{\sqrt{\Delta_Y}} \end{bmatrix}, \tag{4}$$

where characteristic admittance at the input and output are

$$Y_{IN}^{CR} = \sqrt{\frac{Y_{00}}{Y_{11}}\Delta_Y}\ ,\ Y_L^{CR} = \sqrt{\frac{Y_{11}}{Y_{00}}\Delta_Y}\ . \tag{5}$$

In addition, we introduce the normalized value

$$\overline{Y}_L = \frac{Y_L}{Y_L^{CR}}. \tag{6}$$

Let us use the Thévenin equivalent generator. Then, we get the open circuit OC voltage V_1^{OC} and internal conductivity Y_i as follows:

$$V_1^{OC} = \frac{Y_{10}}{Y_{11}}V_0\,,\ Y_i = Y_{11}\,. \tag{7}$$

Next, we obtain the following voltage transfer ratio

$$K_G = \frac{V_1}{V_1^{OC}},\ K_G = \frac{1}{1+Y_L/Y_i},\ V_1 = K_G V_1^{OC}\,. \tag{8}$$

In addition, we use an effectiveness parameter as

$$A = \frac{P_{0MAX}}{P_{GMAX}} = ch^2\gamma\,, \tag{9}$$

where maximum powers of the voltage source and Thévenin equivalent generator at the load sort circuit are as follows:

$$P_{0MAX} = Y_{00}V_0^{\,2},\ \ P_{GMAX} = Y_i \cdot (V_1^{OC})^2\,. \tag{10}$$

First, we consider a simple case of the load power via the voltage transfer ratio. Using (1), (7), and (8), we obtain

$$\frac{P_1(K_G)}{P_{GMAX}} = \tilde{P}_1(K_G) = K_G - K_G^{\,2}\,. \tag{11}$$

This dependence determines a two-valued parabola with the characteristic points in Fig. 2.

We must prove the limited single-valued working area of this characteristic. To do this, we consider this parabola, as a closed curve, in the projective coordinates. Then, point S is the pole and straight line M^+M^- is the polar. Therefore, we get some symmetry or mapping of a "right-hand" working part onto "left" part. Hence, point $K_G = 1$ of the OC regime corresponds to

point $K_G = 0$. In turn, points M^+, M^- are fixed or base points. This implies the correspondence of the typical and running values of $\tilde{P}_1, K_G$.

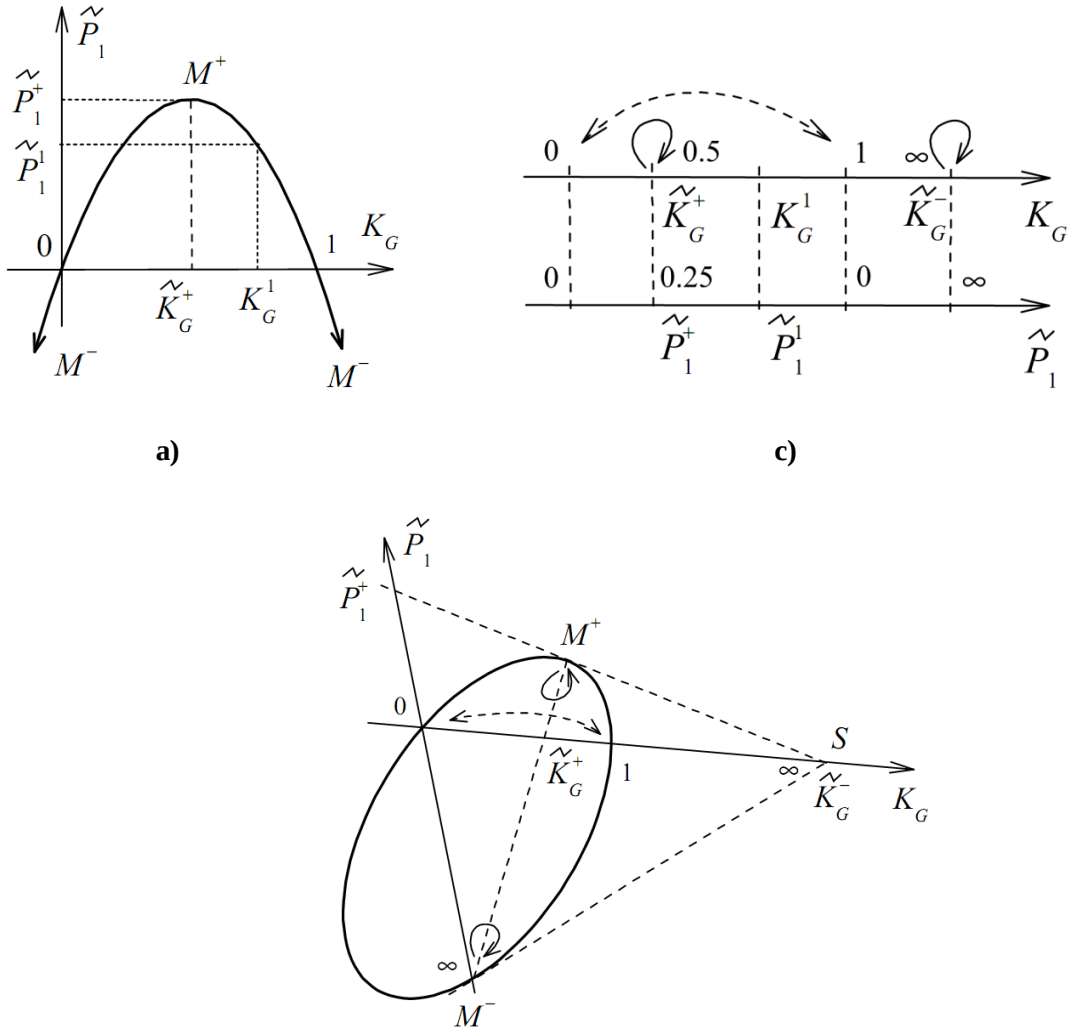

Fig. 2. Load power via the voltage transfer ratio: (a) Cartesian coordinates, (b) projective coordinates, and (c) correspondence of the typical and running values.

A more complicated case corresponds to load power P_1 via load conductivity. Using (8) and (11), this power is as follows:

$$\frac{P_1(Y_L)}{P_{GMAX}} = \frac{Y_L / Y_i}{\left(1 + Y_L / Y_i\right)^2} = \tilde{P}_1(\tilde{Y}_L) = \frac{\tilde{Y}_L}{\left(1 + \tilde{Y}_L\right)^2}. \tag{12}$$

This dependence determines a cubic curve in Fig. 4.

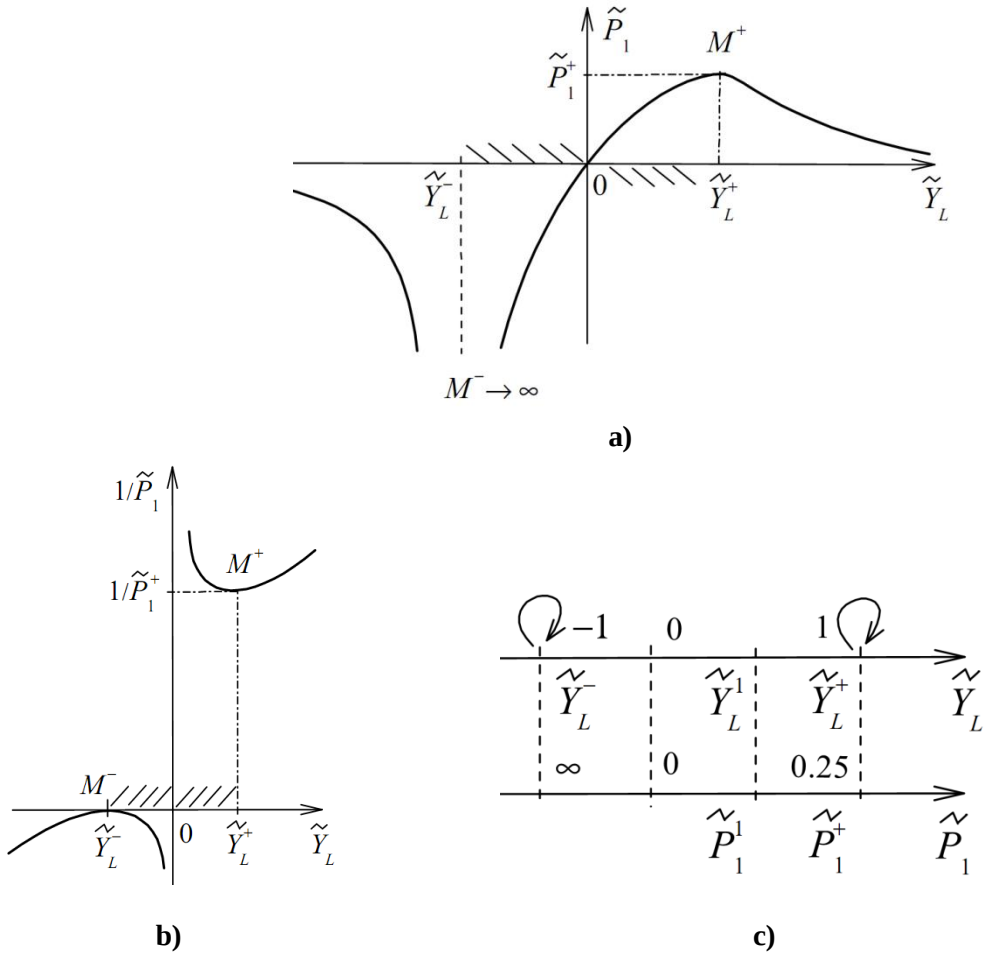

Fig. 4. (a) Load power and (b) this inverse load power via the load conductivity, and (c) correspondence of the typical and running values.

The limited single-valued working area $-1 \le \widetilde{Y}_L \le 1$, which encloses OC regime, is illustrated by dash lines. For explanation of this area, we consider the inverse load power $1/\widetilde{P}_1$ via load conductivity. This dependence determines the hyperbola and the correspondence of the typical and running values $\widetilde{Y}_L, \widetilde{P}_1$ in the single-valued working area.

The most complex case corresponds to efficiency K_P via load conductivity. Using (4)–(6), we obtain

$$K_P(\overline{Y}_L) = \frac{1}{ch^2\gamma + sh^2\gamma + ch\gamma \cdot sh\gamma \cdot \left(\overline{Y}_L + \frac{1}{\overline{Y}_L}\right)} \,. \tag{13}$$

This dependence determines a compound cubic curve in Fig. 5. Points M^+, M^- are fixed base points. In turn, $K_P = \infty$ corresponds to the two load conductivities

$$\overline{Y}_L = -\frac{1}{th\gamma} = -\frac{Y_i}{Y_L^{CR}} = -\overline{Y}_i\,,\ \overline{Y}_L = -\frac{1}{\overline{Y}_i}\,.$$

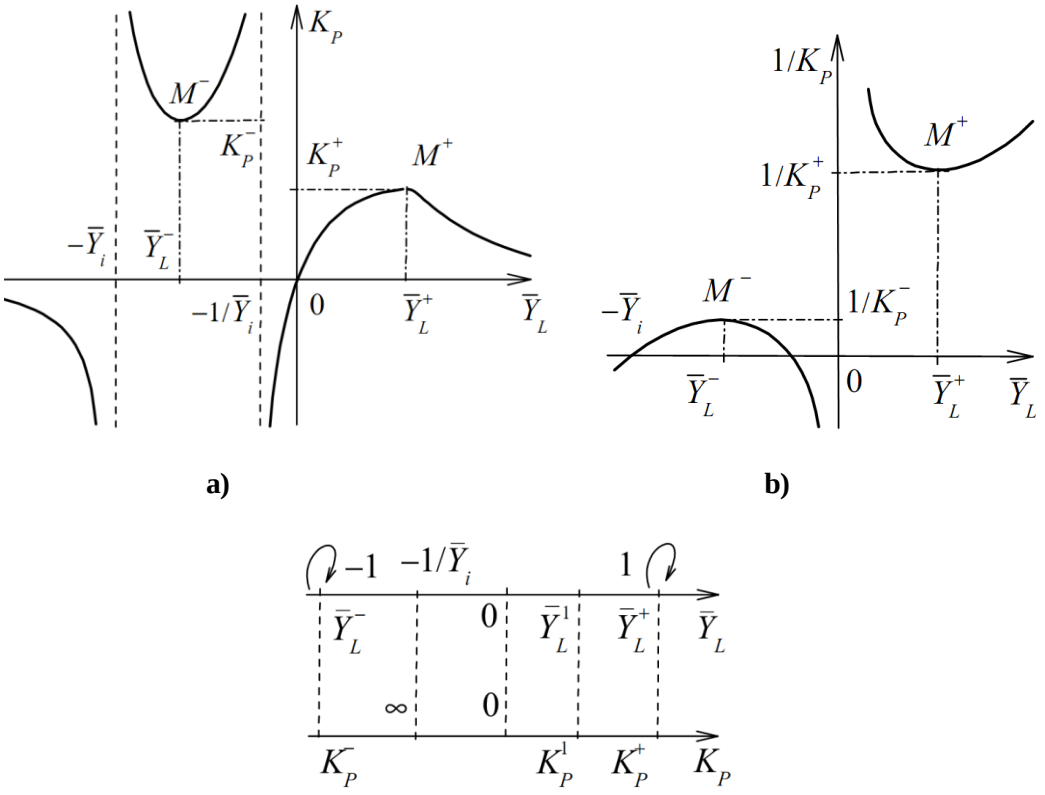

Fig. 5. (a) Efficiency and (b) this inverse efficiency via the load conductivity, and (c) correspondence of the typical and running values,

The limited single-valued working area $-1 \le \overline{Y}_L \le 1$ also encloses the *OC* regime. For explanation of this area, we consider inverse efficiency $1/K_P$ via load conductivity. This dependence determines the hyperbola, similar to Fig. 4b.

3. Invariant Characteristics of Load Power

We consider the load power via the load conductivity and voltage transfer ratio. For clarity, the correspondence of the typical and running values of these parameters is shown in Fig. 6.

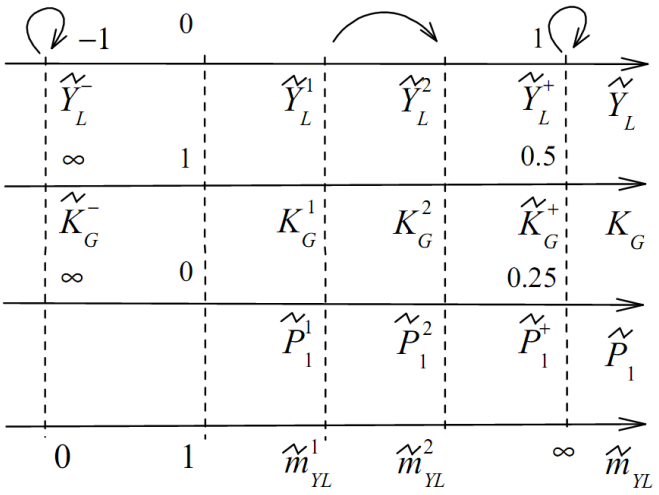

Fig. 6. Correspondence of the typical and running regime values.

The cross ratio for initial values are

$$\tilde{m}^1_{YL} = (\tilde{Y}^-_L \;\; \tilde{Y}^1_L \;\; 0 \;\; \tilde{Y}^+_L) = \frac{\tilde{Y}^1_L + 1}{\tilde{Y}^1_L - 1} \div \frac{0+1}{0-1} = \frac{1+\tilde{Y}^1_L}{1-\tilde{Y}^1_L}. \tag{14.1}$$

$$\begin{aligned} \tilde{m}^1_{KG} &= (\tilde{K}^-_G \;\; K^1_G \;\; 1 \;\; \tilde{K}^+_G) = (\infty \;\; K^1_G \;\; 1 \;\; 0.5) \\ &= \frac{K^1_G - \infty}{K^1_G - 0.5} \div \frac{1-\infty}{1-0.5} = \frac{1-0.5}{K^1_G - 0.5} = \frac{1}{2K^1_G - 1}, \end{aligned} \tag{14.2}$$

$$\tilde{m}^1_{P1} = (\infty \;\; \tilde{P}^1_1 \;\; 0 \;\; \tilde{P}^+_1) = (\infty \;\; \tilde{P}^1_1 \;\; 0 \;\; 0.25) = \frac{1}{1-4\tilde{P}^1_1}. \tag{14.3}$$

The following equality takes place

$$\tilde{m}^1_{P1} = (\tilde{m}^1_{YL})^2 = (\tilde{m}^1_{KG})^2. \tag{15}$$

Next, we consider a regime change due to a load change $\tilde{Y}^1_L \to \tilde{Y}^2_L$. Taking into account (14.1), the cross ratio for this regime changes:

$$\begin{aligned} \tilde{m}^{21}_{YL} &= \tilde{m}^2_{YL} \div \tilde{m}^1_{YL} = (\tilde{Y}^-_L \;\; \tilde{Y}^2_L \;\; \tilde{Y}^1_L \;\; \tilde{Y}^+_L) \\ &= \frac{\tilde{Y}^2_L + 1}{\tilde{Y}^2_L - 1} \div \frac{\tilde{Y}^1_L + 1}{\tilde{Y}^1_L - 1} = \frac{1 + \dfrac{\tilde{Y}^2_L - \tilde{Y}^1_L}{1 - \tilde{Y}^2_L \cdot \tilde{Y}^1_L}}{1 - \dfrac{\tilde{Y}^2_L - \tilde{Y}^1_L}{1 - \tilde{Y}^2_L \cdot \tilde{Y}^1_L}}. \end{aligned} \tag{16}$$

Then, there is strong reason to introduce a conductivity load change value as follows:

$$\tilde{\tilde{Y}}_L^{21} = \frac{\tilde{\tilde{Y}}_L^2 - \tilde{\tilde{Y}}_L^1}{1 - \tilde{\tilde{Y}}_L^2 \cdot \tilde{\tilde{Y}}_L^1}. \tag{17}$$

Therefore, we obtain the typical expression for the regime change:

$$\tilde{\tilde{m}}_{YL}^{21} = \frac{1 + \tilde{\tilde{Y}}_L^{21}}{1 - \tilde{\tilde{Y}}_L^{21}}. \tag{18}$$

Then, the subsequent value is as follows:

$$\tilde{\tilde{Y}}_L^2 = \frac{\tilde{\tilde{Y}}_L^{21} + \tilde{\tilde{Y}}_L^1}{1 + \tilde{\tilde{Y}}_L^{21} \cdot \tilde{\tilde{Y}}_L^1}. \tag{19}$$

Next, taking into account (14.2), we write the cross ratio or regime change for the voltage transfer ratio change $K_G^1 \to K_G^2$:

$$\tilde{\tilde{m}}_{KG}^{21} = (\tilde{\tilde{K}}_G^- \;\; K_G^2 \;\; K_G^1 \;\; \tilde{\tilde{K}}_G^+) = (\infty \;\; K_G^2 \;\; K_G^1 \;\; 0.5) = \frac{2K_G^1 - 1}{2K_G^2 - 1}. \tag{20}$$

We introduce a voltage transfer ratio change value $\tilde{\tilde{K}}_G^{21}$. Then, similarly to (18), the regime changes:

$$\tilde{\tilde{m}}_{KG}^{21} = \frac{1 + \tilde{\tilde{K}}_{KG}^{21}}{1 - \tilde{\tilde{K}}_{KG}^{21}}, \quad \tilde{\tilde{K}}_{KG}^{21} = \frac{\tilde{\tilde{m}}_{KG}^{21} - 1}{\tilde{\tilde{m}}_{KG}^{21} + 1}. \tag{21}$$

Using (20),

$$\tilde{\tilde{K}}_G^{21} = \frac{K_G^1 - K_G^2}{K_G^1 + K_G^2 - 1}. \tag{22}$$

Then, the subsequent value follows:

$$K_G^2 = \frac{K_G^1 (1 - \tilde{\tilde{K}}_G^{21}) + \tilde{\tilde{K}}_G^{21}}{1 + \tilde{\tilde{K}}_G^{21}}. \tag{23}$$

We obtain also the group hyperbolic projective transformation with the base fixed points. For example, if the initial value is $K_G^1 = 0.5$, the subsequent value is $K_G^2 = 0.5$ for various $\tilde{\tilde{K}}_G^{21}$ values.

In addition, similar to (15), the following equality exists:

$$\tilde{\tilde{m}}_{YL}^{21} = \tilde{\tilde{m}}_{KG}^{21}.$$

Then, according to (21), the voltage transfer ratio change value follows:

$$\tilde{\tilde{K}}_{KG}^{21} = \frac{\tilde{\tilde{m}}_{YL}^{21} - 1}{\tilde{\tilde{m}}_{YL}^{21} + 1} = \tilde{\tilde{Y}}_L^{21}. \tag{24}$$

It is obvious that (23) has the form

$$K_G^2 = \frac{K_G^1(1-\tilde{\tilde{Y}}_L^{21}) + \tilde{\tilde{Y}}_L^{21}}{1+\tilde{\tilde{Y}}_L^{21}}. \tag{25}$$

The obtained relationship carries out the direct recalculation of the voltage transfer ratio at a respective conductivity load change value. The main thing for practice, this group projective transformation has the base fixed points. For example, if the initial value is $K_G^1 = 0.5$, then the subsequent value is $K_G^2 = 0.5$ for various $\tilde{\tilde{Y}}_L^{21}$ values.

In addition, taking into account (14.3), we obtain the cross ratio or regime change for the power change $\tilde{\tilde{P}}_1^1 \to \tilde{\tilde{P}}_1^2$:

$$\tilde{\tilde{m}}_{P1}^{21} = (\infty \;\; \tilde{\tilde{P}}_1^2 \;\; \tilde{\tilde{P}}_1^2 \;\; \tilde{\tilde{P}}_1^+) = (\infty \;\; \tilde{\tilde{P}}_1^2 \;\; \tilde{\tilde{P}}_1^2 \;\; 0.25) = \frac{1-4\tilde{\tilde{P}}_1^1}{1-4\tilde{\tilde{P}}_1^2}. \tag{26}$$

We introduce a power change value $\tilde{\tilde{P}}_1^{21}$. Then, similarly to (18), the regime changes:

$$\tilde{\tilde{m}}_{P1}^{21} = \frac{1+\tilde{\tilde{P}}_1^{21}}{1-\tilde{\tilde{P}}_1^{21}}. \tag{27}$$

Using (26),

$$\tilde{\tilde{P}}_1^{21} = \frac{\tilde{\tilde{P}}_1^1 - \tilde{\tilde{P}}_1^2}{\tilde{\tilde{P}}_1^1 + \tilde{\tilde{P}}_1^2 - 0.5}. \tag{28}$$

Then, the subsequent value follows

$$\tilde{\tilde{P}}_1^2 = \frac{\tilde{\tilde{P}}_1^1(1-\tilde{\tilde{P}}_1^{21}) + 0.5\tilde{\tilde{P}}_1^{21}}{1+\tilde{\tilde{P}}_1^{21}}. \tag{29}$$

Similar to (15), the following equality takes place:

$$\tilde{\tilde{m}}_{P1}^{21} = (\tilde{\tilde{m}}_{YL}^{21})^2.$$

Then, using (27), we obtain

$$\tilde{\tilde{P}}_1^{21} = \frac{\tilde{\tilde{m}}_{P1}^{21}-1}{\tilde{\tilde{m}}_{P1}^{21}+1} = \frac{(\tilde{\tilde{m}}_{YL}^{21})^2-1}{(\tilde{\tilde{m}}_{YL}^{21})^2+1}.$$

From here, the known typical expression follows:

$$\tilde{\tilde{P}}_1^{21} = \frac{2\tilde{\tilde{Y}}_L^{21}}{(\tilde{\tilde{Y}}_L^{21})^2+1}. \tag{30}$$

It is obvious that (29) has the form

$$\tilde{\tilde{P}}_1^2 = \frac{\tilde{\tilde{P}}_1^1(1-\tilde{\tilde{Y}}_L^{21})^2 + \tilde{\tilde{Y}}_L^{21}}{(1+\tilde{\tilde{Y}}_L^{21})^2}. \tag{31}$$

The obtained relationship performs the direct recalculation of the load power at a respective conductivity load change value. In addition, this group projective transformation has the base fixed points. For example, if the initial value is $\tilde{P}_1^1 = 0.25$, then the subsequent value is $\tilde{P}_1^2 = 0.25$ for various $\tilde{Y}_L^{21}$ values. The considered cases show that it is not correct to introduce changes of regime parameters in the form of formal increments, divisions, etc. in advance.

We now consider the efficiency via the load conductivity and voltage transfer ratio. For clarity, the correspondence of the typical and running values of these parameters is shown in Fig. 7.

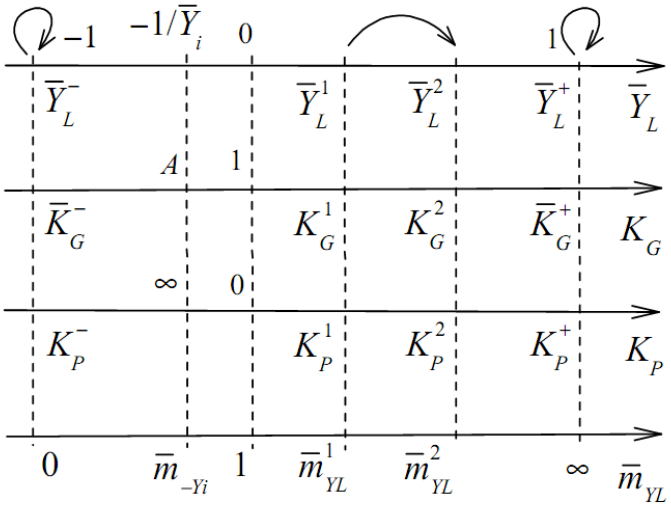

Fig. 7. Correspondence of the typical and running regime values.

The cross ratio for initial values

$$\bar{m}_{YL}^1 = (\bar{Y}_L^- \;\; \bar{Y}_L^1 \;\; 0 \;\; \bar{Y}_L^+) = \frac{1+\bar{Y}_L^1}{1-\bar{Y}_L^1}, \tag{32.1}$$

$$\bar{m}_{KG}^1 = (\bar{K}_G^- \;\; K_G^1 \;\; 1 \;\; \bar{K}_G^+) = \frac{K_G^1 - [A+\sqrt{A(A-1)}]}{K_G^1 - [A-\sqrt{A(A-1)}]} \div \frac{\sqrt{A-1}+\sqrt{A}}{\sqrt{A-1}-\sqrt{A}}. \tag{32.2}$$

$$m_{KP}^1 = (K_P^- \;\; K_P^1 \;\; 0 \;\; K_P^+) = \frac{K_P^1 - [\sqrt{A}+\sqrt{A-1}]^2}{K_G^1 - [\sqrt{A}-\sqrt{A-1}]^2} \div \frac{[\sqrt{A}+\sqrt{A-1}]^2}{[\sqrt{A}-\sqrt{A-1}]^2}. \tag{32.3}$$

The known equality

$$m_{KP}^1 = (\bar{m}_{YL}^1)^2 = (\bar{m}_{KG}^1)^2. \tag{33}$$

We consider a regime change due to a load change $\bar{Y}_L^1 \to \bar{Y}_L^2$. The cross ratio for this regime changes:

$$\bar{m}_{YL}^{21} = \bar{m}_{YL}^2 \div \bar{m}_{YL}^1 = (\bar{Y}_L^- \;\; \bar{Y}_L^2 \;\; \bar{Y}_L^1 \;\; \bar{Y}_L^+) = \frac{\bar{Y}_L^2+1}{\bar{Y}_L^2-1} \div \frac{\bar{Y}_L^1+1}{\bar{Y}_L^1-1}. \tag{34}$$

Therefore, we obtain the following request expressions at once.
The conductivity load change value

$$\overline{Y}_L^{21} = \frac{\overline{Y}_L^2 - \overline{Y}_L^1}{1 - \overline{Y}_L^2 \cdot \overline{Y}_L^1}. \tag{35}$$

The regime change

$$\overline{m}_{YL}^{21} = \frac{1 + \overline{Y}_L^{21}}{1 - \overline{Y}_L^{21}}. \tag{36}$$

The subsequent value corresponds to hyperbolic projective transformation (19):

$$\overline{Y}_L^2 = \frac{\overline{Y}_L^{21} + \overline{Y}_L^1}{1 + \overline{Y}_L^{21} \cdot \overline{Y}_L^1}. \tag{37}$$

Next, we write the cross ratio for the voltage transfer ratio change $K_G^1 \to K_G^2$:

$$\overline{m}_{KG}^{21} = (\overline{K}_G^- \quad K_G^2 \quad K_G^1 \quad \overline{K}_G^+) = \frac{K_G^2 - [A + \sqrt{A(A-1)}]}{K_G^2 - [A - \sqrt{A(A-1)}]} \div \frac{K_G^1 - [A + \sqrt{A(A-1)}]}{K_G^1 - [A - \sqrt{A(A-1)}]}. \tag{38}$$

Similarly, we introduce a voltage transfer ratio change value $\overline{K}_G^{21}$. Then, similar to (21), the regime change

$$\overline{m}_{KG}^{21} = \frac{1 + \overline{K}_{KG}^{21}}{1 - \overline{K}_{KG}^{21}}. \tag{39}$$

Using (38), the voltage transfer ratio change value

$$\overline{K}_G^{21} = \sqrt{A(A-1)}\,\frac{K_G^2 - K_G^1}{K_G^2 \cdot K_G^1 - A(K_G^2 + K_G^1 - 1)}. \tag{40}$$

Then, the subsequent value

$$K_G^2 = \frac{AK_G^{21}(K_G^1 - 1) - K_G^1\sqrt{A(A-1)}}{K_G^{21}(K_G^1 - A) - \sqrt{A(A-1)}}. \tag{41}$$

The known equality

$$\overline{m}_{YL}^{21} = \overline{m}_{KG}^{21}.$$

Then, according to (39), the voltage transfer ratio change value follows:

$$\overline{K}_{KG}^{21} = \frac{\overline{m}_{YL}^{21} - 1}{\overline{m}_{YL}^{21} + 1} = \overline{Y}_L^{21}. \tag{42}$$

It is obvious that (41) gets the form

$$K_G^2 = \frac{K_G^1[A\overline{Y}_L^{21} - \sqrt{A(A-1)}] - A\overline{Y}_L^{21}}{K_G^1\overline{Y}_L^{21} - [A\overline{Y}_L^{21} + \sqrt{A(A-1)}]}. \quad (43)$$

The obtained relationship carries out the direct recalculation of the voltage transfer ratio at a respective conductivity load change value. In addition, this group projective transformation has the base fixed points. For example, if the initial value is $K_G^1 = A \pm \sqrt{A(A-1)}$, then the subsequent value is $K_G^2 = A \pm \sqrt{A(A-1)}$ for various values $\overline{Y}_L^{21}$.

As the last step, we get the cross ratio for the efficiency change $K_P^1 \to K_P^2$:

$$\overline{m}_{KP}^{21} = (K_P^- \quad K_P^2 \quad K_P^1 \quad K_P^+) = \frac{K_P^2 - [\sqrt{A} + \sqrt{A-1}]^2}{K_G^2 - [\sqrt{A} - \sqrt{A-1}]^2} \div \frac{K_P^1 - [\sqrt{A} + \sqrt{A-1}]^2}{K_G^1 - [\sqrt{A} - \sqrt{A-1}]^2}. \quad (44)$$

We introduce an efficiency change value $\overline{K}_P^{21}$. Then, the regime change

$$\overline{m}_{KP}^{21} = \frac{1 + \overline{K}_P^{21}}{1 - \overline{K}_P^{21}}. \quad (45)$$

Using (44), the efficiency change value

$$\overline{K}_P^{21} = 2\sqrt{A(A-1)}\,\frac{K_P^2 - K_P^1}{K_P^2 \cdot K_P^1 - (2A-1)\cdot(K_P^2 + K_P^1) + 1}. \quad (46)$$

Then, the subsequent value

$$K_P^2 = \frac{\overline{K}_P^{21}[(2A-1)K_P^1 - 1] - 2\sqrt{A(A-1)}\,K_P^1}{\overline{K}_P^{21}[K_P^1 - (2A-1)] - 2\sqrt{A(A-1)}}. \quad (47)$$

The known equality

$$\overline{m}_{KP}^{21} = (\overline{m}_{YL}^{21})^2.$$

Therefore, using (45),

$$\overline{K}_P^{21} = \frac{\overline{m}_{KP}^{21} - 1}{\overline{m}_{KP}^{21} + 1} = \frac{(\overline{m}_{YL}^{21})^2 - 1}{(\overline{m}_{YL}^{21})^2 + 1}.$$

From here, the known typical expression follows:

$$\overline{K}_P^{21} = \frac{2\overline{Y}_L^{21}}{(\overline{Y}_L^{21})^2 + 1}.$$

It is obvious that (47) has the form

$$K_P^2 = \frac{K_P^1\{2\overline{Y}_L^{21}(2A-1) - 2\sqrt{A(A-1)}[(\overline{Y}_L^{21})^2 + 1]\} + 2\overline{Y}_L^{21}}{2K_P^1\overline{Y}_L^{21} - \{2\overline{Y}_L^{21}(2A-1) + 2\sqrt{A(A-1)}[(\overline{Y}_L^{21})^2 + 1]\}}.$$

The obtained relationship performs the direct recalculation of the efficiency at a respective conductivity load change value. Also, this group projective transformation has the base fixed points. For example, if the initial value is $K_P^1 = (\sqrt{A} \pm \sqrt{A-1})^2$, then the subsequent value is $K_P^2 = (\sqrt{A} \pm \sqrt{A-1})^2$ for various values $\overline{Y}_L^{21}$.

Thus, this well-founded introduction of regime parameter changes shows that the form of expressions for the subsequent values depends on the type of the regime. Therefore, it will be not correct to introduce formal increments, divisions, etc.

4. Conclusions

(i) The cross ratio for quadratic fractional expressions is carried out in a limited single-valued working area.
(ii) The cross ratio is accepted as the regime parameter in a relative form, which is invariant to the type of the actual regime parameters and circuit sections and depends on the type of the actual regime.
(iii) Changes in regime parameters are proved; direct formulas of recalculation are proposed.
(iv) The application of this approach to the alternating current circuits is a promising direction of researches.
(v) The represented invariant properties of energy characteristics give the base for the determination of single-valued areas of various cubic expressions.

References

[1] C. Alexander and M. Sadiku, Fundamentals of Electric Circuits, 5th ed. McGraw–Hill, New York, 2013.
[2] S. Bhattacharyya, L. Keel, and D. Mohsenizadeh, Linear Systems: A Measurement Based Approach, Springer, India, 2014.
[3] A. Frank, Schaum's Outline of Theory and Problems of Projective Geometry, McGraw–Hill, New York, 1967.
[4] R. Riaza, IEEE Trans. Circ. Syst. I: 66 (2), 463 (2018).
[5] A. Penin, Analysis of Electrical Circuits with Variable Load Regime Parameters: Projective Geometry Method. 2nd ed, Springer International Publishing AG Switzerland, 2016.
[6] R. Bryant, J. Tygar, and L. Huang, IEEE Trans. Circ. Syst. I 41 (11), 686 (1994).
[7] V. Mazin, Meas. Tech. 26 (8), 628 (1983).
[8] O. Tsybul'skii, Meas. Tech. 60 (5), 443 (2017).

CONTENTS

Condensed Matter Theory

Experimental Physics of Bulk Materials, Films, Wires, Coordination Clusters, and Quantum Dots

Physics of Nanofluids

Physics and Engineering of Electronic and Electrotechnical Devices